

University of Nebraska - Lincoln

DigitalCommons@University of Nebraska - Lincoln

---

Civil Engineering Theses, Dissertations, and  
Student Research

Civil Engineering

---

5-2015

# Velocity Distributions and Wall Pressures in a Scale Model Gated Box Culvert Control Structure

Alexander L. Evans

University of Nebraska-Lincoln, xander.evans@gmail.com

Follow this and additional works at: <http://digitalcommons.unl.edu/civilengdiss>



Part of the [Civil Engineering Commons](#), and the [Hydraulic Engineering Commons](#)

---

Evans, Alexander L., "Velocity Distributions and Wall Pressures in a Scale Model Gated Box Culvert Control Structure" (2015). *Civil Engineering Theses, Dissertations, and Student Research*. 78.

<http://digitalcommons.unl.edu/civilengdiss/78>

This Article is brought to you for free and open access by the Civil Engineering at DigitalCommons@University of Nebraska - Lincoln. It has been accepted for inclusion in Civil Engineering Theses, Dissertations, and Student Research by an authorized administrator of DigitalCommons@University of Nebraska - Lincoln.

**VELOCITY DISTRIBUTIONS AND WALL PRESSURES IN A  
SCALE MODEL GATED BOX CULVERT CONTROL STRUCTURE**

By

Alexander L. Evans

A THESIS

Presented to the Faculty of  
The Graduate College at the University of Nebraska  
In Partial Fulfillment of Requirements  
For the Degree of Master of Science

Major: Civil Engineering

Under the Supervision of Professor David M. Admiraal

Lincoln, Nebraska

May, 2015

# VELOCITY DISTRIBUTIONS AND WALL PRESSURES IN A SCALE MODEL GATED BOX CULVERT CONTROL STRUCTURE

Alexander L. Evans, M.S.

University of Nebraska, 2015

Adviser: David M. Admiraal

The South Florida Water Management District (SFWMD) manages a system of canals and structures that control the flow through several large storm water treatment areas (STA). The present project was initiated because of the partial failure of a three-barrel, gated box culvert structure that belongs to the system. The structure has a forebay with three sluice gates that control the flow into three 8 ft by 8 ft box culverts. Settling and partial failure of the culverts in the structure was presumably caused by piping of sediment through joints in pre-cast sections of culvert. It was hypothesized that both unsteady pressure fluctuations and pressure differentials between the outside and inside of the culverts led to the piping failure. To better understand flow characteristics in the culvert that may cause these adverse effects, a 1:8-scale model of one of the three gated culverts was constructed. The bed of the model culvert was instrumented with eight pressure tap transducers. In addition, a Particle Image Velocimetry (PIV) system was employed to record velocity distributions immediately downstream of the sluice gate, where piping and settlement was most prominent in the prototype.

Eight experiments of varying gate settings and flow conditions were carried out in the flume model. Both pressure and velocity distribution data were gathered. PIV data provided visual depiction of the formation, travel path, and translation to the flume bed of

turbulent flow structures originating in the hydraulic jump recirculation zone within the model. The pressure taps captured spikes in pressures associated with these flow structures as they were translated to the bed. Trends between pressure and velocity were observed in the data and indicated that low gate settings produced conditions that were more likely to cause the aforementioned adverse effects in the prototype. The flow jet in low gate settings produced strong negative pressure zones along the bed, downstream of the gate. It also generated a more pronounced recirculation zone above the jet where turbulent structures were observed to form and be translated to the bed causing spikes in pressure.

## Acknowledgements

To my beautiful wife Kristi, for always encouraging and helping me get through it all. I love you.

I thank my parents who have done so much for me in my life and who have made all of this possible. I love you both.

I would like to thank my prayer squad A-team – Mom, G-Ma, and Robin. Prayers were needed from day one freshman year and I could always (and still can) count on you.

I thank Dr. David Admiraal, for whom none of this would have been possible. Over the many years I have learned much from you in both academics and life. I could not have been blessed with a better teacher, advisor, boss, or mentor. I thoroughly enjoyed the long hours in the lab we spent jamming out to 80's pop classics over the sounds and smells of grinding steel, welding, silicone, blue paint, and the sweet California Cancer adhesive as we made the finest flume two nerds have ever built. Cheers.

I spent the better part of a decade at the University (Hey, a lot of people go to college for seven years...) and some of my most cherished moments were from the experiences shared with my graduate schoolmates:

Clarky Sparky: The best officemate a guy could ask for. There are too many fond memories to put in here. Just thinking of some make me bring forth a profound guttural laugh that would make Miles shake his head in disbelief once again. Our trips to UNL storage, 5-star cuisine lunches from the vending machine, messing with Whitney, Pam and Jennifer, hidden cameras filming Admiraal, MRE madness, Fear the Beard, Flume Raft Barbie, planking, shredding degrees, our office decor, EWB pizza sales, the world

map (where is that by the way? Jake probably took it), and of course your continual selfless good deed of giving directions to all the “lost” students in Nebraska Hall. On top of all this we still managed to get a little work done on my research, not yours so much, but mine, and that is all that matters. I thank you for everything.

Miles: The level headed one in the group. If it wasn't for you, we all would have had a lot fewer assignments completed and I may never have built my flume. I am completely indebted to you for all the work you put in to help me. The gallons of Smurf blue paint, silicone, endless drill holes and saw cuts (how did that drill not explode), and the most obscene amount of Dremel work every taken on by humans. I will forever be thankful.

Mohamed: You always had a smile on your face no matter how much I was annoying you. Thank you for all the good times and the fufu. *“I bless the rains down in Africa”*.

I would like to thank Pam and Whitney. Pam helped countless fledgling students over her tenure and I was no exception. It was such a fun time in Nebraska Hall when the gang would get together and bug Pam and Whitney. They were such good sports and so much fun. I thank you both.

I would like to gratefully acknowledge the financial support of the SFWMD

I would also like to thank Dr. Stansbury and Dr. Li for their advice and support serving as my technical review committee.

Finally, and with the greatest thanks; God, for all my blessings, abilities, answered prayers, and for absolutely everything in my life.

## Table of Contents

Acknowledgements.....	iv
Table of Contents.....	vi
List of Tables.....	viii
List of Figures.....	ix
Notation.....	x
Chapter 1 Introduction.....	1
1.1 Background.....	1
1.2 Objectives.....	2
1.3 Organization of Thesis.....	5
Chapter 2 Literature Review.....	6
2.1 Hydraulic Jumps and Associated Pressure Fluctuations.....	6
2.2 Submerged Hydraulic Jumps.....	9
2.3 Sluice Gates.....	10
2.4 Flow under Sluice Gates.....	11
2.5 Physical Model Scaling.....	11
2.6 Instrumentation.....	12
2.6.1 Pressure Taps.....	13
2.6.2 Particle Image Velocimetry (PIV).....	13
Chapter 3 Construction of the S-375 Physical Model.....	15
3.1 S-375 Prototype.....	15
3.2 Model Type and Scale.....	16
3.3 Model Construction.....	25
Chapter 4 Instrumentation.....	32
4.1 Pressure Transducers.....	32
4.2 Pressure Transducer Calibration.....	34
4.3 PIV System.....	36
4.4 Instrumentation Timing Set Up.....	40
4.5 V-Notch Outlet Weir.....	42
Chapter 5 Measurements and Methods.....	44
5.1 Introduction.....	44

5.2	Physical Model Measurements.....	44
5.3	PIV Measurements .....	47
5.4	Pressure Transducer Measurements .....	49
Chapter 6	Results.....	50
6.1	Introduction .....	50
6.2	Average Velocity Fields.....	52
6.3	PIV Observed Turbulent Flow Incursions .....	54
6.4	PIV Measurements of the Entire Flume .....	57
6.5	Pressure Measurements .....	59
6.6	Correlation of Pressures .....	67
6.7	Velocity and Pressure Relationship.....	69
Chapter 7	Conclusions.....	74
7.1	Overview .....	74
7.2	Observations.....	74
7.3	Future Work and Other Considerations .....	77
	Bibliography .....	79
	Appendices.....	81
Appendix A	Average Velocity Contour Maps .....	82
Appendix B	Measurement, Data Acquisition, and Other System Appurtenances .....	98



## List of Tables

Table 2-1 Parameter ratios for Froude and Reynolds models.....	12
Table 3-1 S-375 Operating conditions.....	16
Table 4-1 Pressure transducer linear regression equation and standard deviations.....	36
Table 6-1 Experiment Data Collection Summary.....	51

## List of Figures

Figure 1-1 Aerial view of STA (Gonzalez, 2010) .....	1
Figure 1-2 Schematic of STA-1 including location of S-375 control structure (Gonzalez, 2010) .....	2
Figure 1-3 Exaggerated scale profile view of settlement in prototype culverts .....	3
Figure 1-4 Profile view of S375 control structure (Gonzalez, 2010) .....	4
Figure 2-1 Schematic of a sluice gate (Roth and Hager, 1999) .....	10
Figure 3-1 S-375 gate structure and run-out culverts (Gonzalez, 2010).....	15
Figure 3-2 a) Construction installation of precast culvert sections and b) Construction of culverts (Gonzalez, 2010) .....	16
Figure 3-3 Geometric Model Dimensions .....	22
Figure 3-4 Physical model 3D layout .....	25
Figure 3-5 Sluice gate and threaded rod control .....	27
Figure 3-6 Model Culvert Barrel Section .....	28
Figure 3-7 Model head tank, forebay, culvert, tailbox, and piping. ....	30
Figure 3-8 V-Notch weir tank.....	31
Figure 4-1 Aluminum slot inserts .....	32
Figure 4-2 Pressure transducers and manometers installed in the slot inserts along the flume bed .....	34
Figure 4-3 Pressure sensor 4 sample calibration showing both dates of testing and the resulting regression equation .....	36
Figure 4-4 Custom PIV optic system.....	38
Figure 4-5 PIV Instrumentation timing grid .....	41
Figure 4-6 V-notch weir flow rate calibration .....	43
Figure 5-1 Data Sheet for Experiment G06.00 .....	46
Figure 6-1 Low velocity turbulent flow structure transported from the recirculation zone to the bed for Experiment G05.00.....	55
Figure 6-2 Streamwise velocity contours for the entire model culvert for a gate setting of 4.8 inches and a flow rate of 2.15 cfs .....	58
Figure 6-3 Relative Pressure Graphs .....	64
Figure 6-4 Pressure Correlation Graph of Experiment G05.00 .....	67
Figure 6-5 Pressure Readings from Experiment G05.00 Associated with Visible Flow Incursion .....	70
Figure 6-6 Experiment G05.00 Pressure Spike.....	71
Figure 6-7 Long-term Pressure Trends in Experiment G05.00 .....	73

## Notation

Symbol / Variable	Description
SFWMD	South Florida Water Management District
STA	Stormwater Treatment Area
PIV	Particle Image Velocimetry
DES	Detached Eddy Simulation
NGVD	National Geodetic Vertical Datum
cfs	Cubic Feet per Second
gpm	Gallons per Minute
Nd:YAG	Neodymium-doped Yttrium Aluminum Garnet
ft	Feet
g	Gravitational Acceleration, $9.81 \text{ m/s}^2$
Q	Flow Rate
$F_r$	Froude Number
$R_e$	Reynolds Number
$L_r$	Length Scale Ratio
$V_r$	Velocity Scale Ratio
$\rho_r$	Density Scale Ratio
V	Velocity
y	Depth of Water
$y_1$	Supercritical Depth of Hydraulic Jump
$y_2$	Subcritical Depth of Hydraulic Jump
$F_1$	Froude Number at Supercritical Section of Hydraulic Jump
$C_s$	Coefficient of Discharge
$R_e$	Reynolds Number in Model
$\nu$	Kinematic Viscosity
$Q_m$	Flow Rate in Model
$H_p$	Height of Prototype
$V_p$	Velocity in Prototype
$R_p$	Reynolds Number in Prototype
$\nu_p$	Kinematic Viscosity in the Prototype

## Chapter 1 Introduction

### 1.1 Background

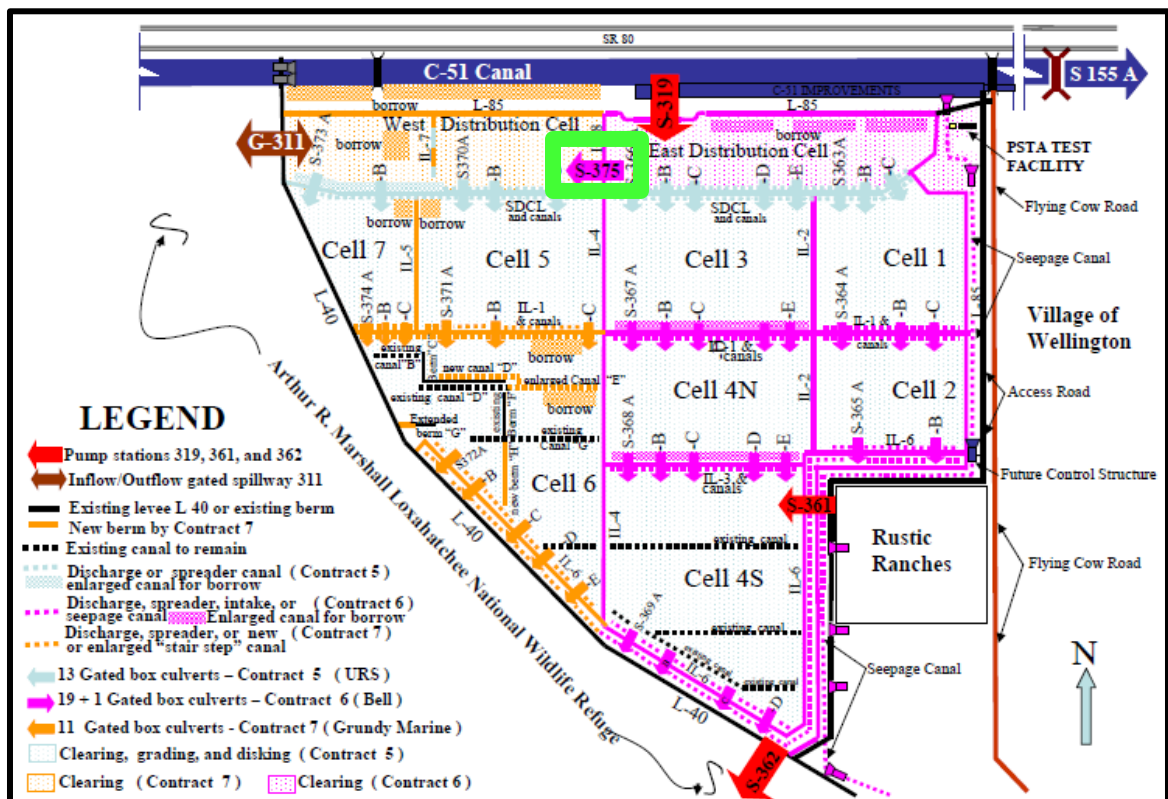
South Florida Water Management District owns and operates numerous Stormwater Treatment Areas (STAs). Figure 1-1 shows an aerial view of an STA. Agricultural and stormwater runoff is conveyed through these STAs in an effort to remove pollutants through settling and vegetative uptake before the water flows downstream to cities in South Florida and the Everglades. The STAs are extremely vast in size. They consist of vegetative retention cells, canals, hydraulic control structures, and inlet and outlet works.



Figure 1-1 Aerial view of STA (Gonzalez, 2010)

## 1.2 Objectives

This project was initiated because of the partial failure of an S-375 gated box culvert hydraulic control structure in the South Florida Water Management District Stormwater Treatment Area 1 East (STA-1E). The S-375 control structure consists of three 8 ft by 8 ft gated box culverts operating in parallel. Further information will be given on the culverts in subsequent sections. See Figure 1-2 for the schematic of STA-1E with the location of the S-375 control structure identified by the bright green box.



**Figure 1-2 Schematic of STA-1 including location of S-375 control structure (Gonzalez, 2010)**

Partial failure of the control structure was discovered when sinkholes were found on an embankment above the box culverts. Subsequently, the insides of the culverts were inspected and some sections of the culverts were found to have settled several inches. In

some cases, settling had left gaps between the precast sections of the concrete box culvert. See Figure 1-3 for a depiction of the settlement observed in the culvert and associated sections.

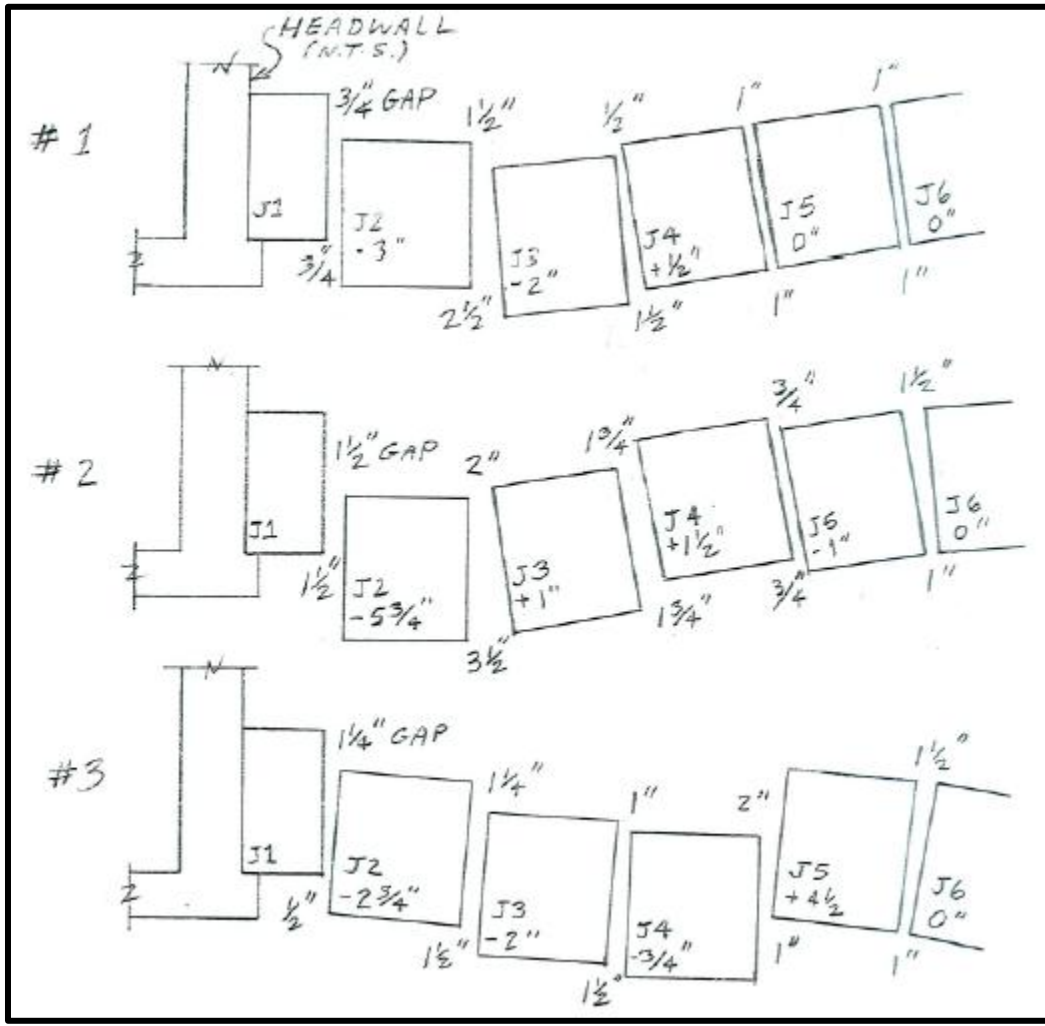
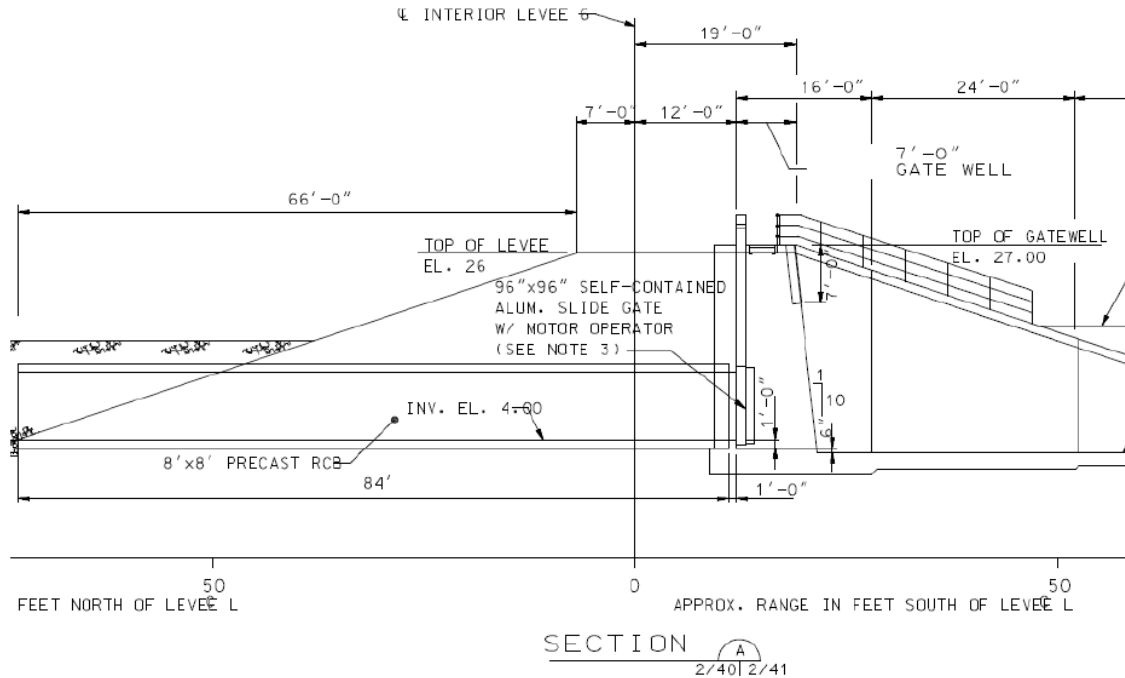


Figure 1-3 Exaggerated scale profile view of settlement in prototype culverts

These gaps likely exacerbated the problem leading to further deterioration of the foundation of the box culvert control structure. See Figure 1-4 for a profile view of the S375 control structure. The flow is from right to left in Figure 1-4.



**Figure 1-4 Profile view of S375 control structure (Gonzalez, 2010)**

It was presumed that the cause of the failure was piping of sediment from the outside casing of the structure into the box culverts through the joints between the precast sections that make up the barrel of the structure. The erosion that occurred through the joints was assumed to be induced by either pressure fluctuations in the flume barrel or by a pressure differential between the inside and the outside of the flume barrel. These pressure fluctuations and or differentials were assumed to be caused by flow characteristics associated with the hydraulic jump that formed downstream of the inlet sluice gate.

To better understand the pressure characteristics that presumably led to the partial failure within the culvert, a model of the S-375 structure was constructed for experimentation. Understanding the operating conditions that potentially produce the adverse pressure conditions may prevent future failures of similar structures.



### 1.3 Organization of Thesis

This thesis consists of an introduction, literature review, a discussion of the layout and design of the S-375 gated control structure, model scaling, model construction, an introduction to the essential components of the model, description of the testing equipment and the operation parameters, measurements, results, and conclusions. Finally, appendices containing referenced figures and details of the equipment and instrumentation used are provided for reference purposes.



## Chapter 2 Literature Review

### 2.1 Hydraulic Jumps and Associated Pressure Fluctuations

The Froude number is defined by  $F_r = \frac{V}{(gy)^{0.5}}$ , where  $V$  is flow velocity,  $g$  is gravitational acceleration, and  $y$  is depth. A supercritical flow ( $F_r > 1$ ) can transform into a subcritical flow ( $F_r < 1$ ) by passing through a hydraulic jump. The rapid transition from supercritical to subcritical flow occurs when the tailwater depth is equal to the subcritical sequent depth of the incoming supercritical flow, resulting in a great deal of energy dissipation. The sequent depths are related by the Belanger equation

$\left(\frac{y_2}{y_1} = \frac{1}{2}(\sqrt{1 + 8F_1^2} - 1)\right)$  where  $y_1$  and  $y_2$  equal supercritical and subcritical sequent depths of the jump, respectively, and  $F_1$  is the Froude number at the supercritical section of the jump. (Habibzadeh et al. 2011).

The energy dissipation is due to the production of large-scale, multiphase (air-water) turbulence and the resulting conversion of the turbulence into heat. This process generates low frequency hydrodynamic pressure fluctuations on the channel bottom and side walls surrounding the jump. Significant damage has been reported on stilling basins and spillways due to such pressure fluctuations.

Various articles have been published examining these fluctuating pressures which have been linked to many chute and basin failures. Even with numerous articles and studies performed, there is still a lack of quantitative data on the magnitude of the pressure fluctuations and an acceptable design procedure to deal with these issues in spillways and other applications. This is a major problem because these structures may fail at flow

rates much lower than design maximum flow rates if pressure fluctuations are severe enough.

In 1964, Bowers, Tsai, and Kuha completed a report on the failure of the Karnafuli Dam spillway. In 1961, the spillway chute on the Karnafuli Hydroelectric Facility was damaged by flows at 20% of the design discharge. In the report it is suggested that fluctuating pressures associated with the hydraulic jump could have caused sufficient uplift to remove the spillway slabs. In 1987, Toso and Bowers conducted model studies of spillway damage in the Karnafuli project. They believed that the flow conditions were such that fluctuating pressures in the hydraulic jump were the primary cause of failure of the chute slab in 1961. They went on to say that instantaneous pressure differentials probably occurred between the chute block drain opening and the upper surface of the chute slab and that the net difference between these pressures and those on the surface of the slab were believed to have created forces that were far in excess of the weight of the chute slab, leading to uplift and spillway damage.

Toso and Bowers established that the failure process was due to the severe pulsating pressures in the hydraulic jump region, in particular they determined that; a) the pulsating pressures may have damaged the joint seal of the slabs and, through the unsealed joints, extreme pressure values may have propagated from the upper to the lower surface of the slabs; b) the instantaneous difference between the total pressure acting on the upper and lower surfaces of the slab reached high values, occasionally causing the total uplift force to exceed the weight of the slab; c) the instantaneous spatial structure of pressure fluctuations may also have played a relevant role in the magnitude of the overall lifting force.

In 1967 Vasiliev and Bukreyev performed a significant study on pressure fluctuations in hydraulic jumps and aimed at ways to define the dynamic load acting on the containment structure of the hydraulic jump. Vasiliev and Bukreyev stated that the most common method for determining the dynamic load was in terms of the standard deviation of the fluctuating force. In 2000, Pirooz and Kavianpour studied the effect of inflow conditions on pressure fluctuations at the bottom of a hydraulic jump with Froude numbers of 6, 8 and 10.

In 1971, Schiebe described the stochastic characteristics of pressure fluctuations on the bed under a hydraulic jump. Schiebe also showed exceptional agreement on the root-mean-square (RMS) of pressure fluctuations in two laboratory channels, one five times as large as the other. His study supported Froude scaling relationships.

Khader and Elango performed laboratory experiments on the pressure fluctuations beneath spatial hydraulic jumps downstream of an expansion. They tested flow rates with Froude numbers ranging from 3.52 to 6.86. The hydraulic jumps formed downstream of an expansion. Pressure transducers were used to gather pressure data at a rate of 100 Hz. They found that the peak frequencies and intensity coefficients of spatial hydraulic jumps were higher than those of classic hydraulic jumps.

In 1991, Farhodi and Narayanan studied the force on the slab beneath a hydraulic jump. They conducted experimental measurements on the mean and fluctuating forces exerted on the slab beneath a free hydraulic jump. They concluded that the scale of the pressure producing patterns is larger in the transverse direction than in the stream-wise direction.

Also, the intensity of force fluctuations on a slab depends on the relative magnitude of the ratio of its width to its length.

## 2.2 Submerged Hydraulic Jumps

When the tailwater depth is greater than the subcritical sequent depth, the hydraulic jump will become submerged. It has been observed that when the submergence of the jump increases, jet mixing decreases. This results in less energy dissipation compared to free jumps, and the decay of the high velocity jet coming into the jump is retarded (Rajaratnam 1967, 1965; Govinda Rao and Rajaratnam 1963).

Submerged hydraulic jumps have been studied by many researchers, including Dey and Sarkar 2008; Leutheusser and Fan 2001; Long et al. 1990; Narasimhan and Bhargava 1976; Rajaratnam 1965; Rao and Rajaratnam 1963.

An important feature of the hydraulic jump is the recirculation zone or roller. This recirculation zone plays a major part in the dissipation of energy. It has been found that the strength of the backward roller can be connected with scour caused by the jump (Zare, Baddour 2007). Zare and Baddour also concluded that the strength of the roller is significantly higher near the walls than at the center of the jump. They claim this may be attributed to the high forward jet velocities near the inlet which delay the formation of the roller in the central region of the channel. They also noted that the roller was attached to the walls close to the bottom of the channel, and near the surface the roller extended over the entire width of the channel.

### 2.3 Sluice Gates

Sluice gates are hydraulic structures that allow control of discharge and the upstream water surface elevation and can be used to measure flow rates. Roth and Hager (1999) provided the sketch of a typical sluice gate shown in Figure 2-1 and definitions of its components. The relevant variables are defined as the flow rate  $Q$ , the approach flow depth  $h_o$ , the height of the gate opening  $a$ , and the downstream depth  $h_u$ .

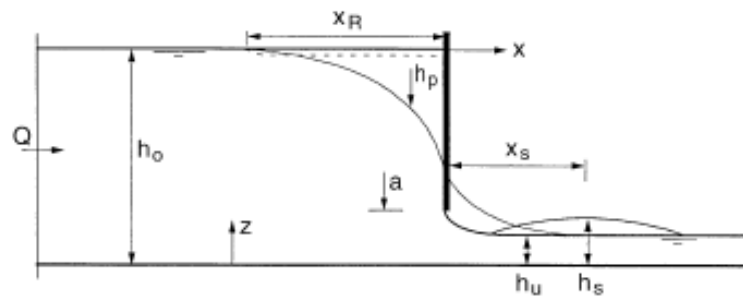


**Figure 2-1 Schematic of a sluice gate (Roth and Hager, 1999)**

The equation given by Roth and Hager (1999) as well as by Rajaratnam and Subramanya (1967) is:

$$Q = C_s a b \sqrt{2g h_o^{1/2}} \quad (2.1)$$

Where  $C_s$  is the coefficient of discharge,  $b$  is the channel width, and  $g$  is the acceleration of gravity.

The sluice gate examined in this project is of similar nature to the sluice gate defined for this equation. The gate is rectangular in shape, sharp crested, and located in a smooth rectangular channel. According to Roth and Hager the surface roughness effect on both the gate and channel below the gate are insignificant.

## 2.4 Flow under Sluice Gates

Kim (2007) and Akoz et al. (2009) studied the validity of Reynolds Average Navier–Stokes (RANS) simulations for sluice gates in free flow, focusing on pressure field and mesh influence. In comparison, less has been done for submerged flow.

Cassan and Belaud (2012) performed a study on the flow under sluice gates and emphasized the work on submerged flow under sluice gates. The study consisted of a numerical Reynolds Average Navier-Stokes model and an experimental model.

In the case of submerged flow with large gate opening, they concluded that the contraction coefficient should not be assumed to be similar to 0.61 which is typical of free flow because the coefficient was observed to significantly increase with gate opening, which is consistent with the energy-momentum balance.

## 2.5 Physical Model Scaling

Typically, hydraulic models are scaled based on Froude and Reynolds number similarity.

In open atmosphere models where gravity controls flow behavior, the Froude number plays an important role. When hydraulic model flows are pressurized or submerged,

Reynolds number scaling is important. For either of these two types of flows, simple ratio formulas can be used to scale variables between the model and the prototype; such ratios are found in most fluid mechanics texts and articles, such as in Roberson et al. (1988). See Table 2-1 below for parameter ratios for Froude and Reynolds models.

Where  $L_r$  is the length scale ratio,  $V_r$  is the velocity scale ratio, and  $\rho_r$  is the density scale ratio.

**Table 2-1 Parameter ratios for Froude and Reynolds models**

<b>Property</b>	<b>General Relation</b>	
	<b>Fr</b>	<b>Re</b>
Geometry	$L_r$	$L_r$
Velocity	$L_r^{1/2}$	$V_r / L_r$
Discharge	$L_r^{5/2}$	$L_r V_r$
Force	$L_r^3$	$V_r \rho_r$

Often, one dimensionless parameter can be considered to be dominant. However, according to Rouse (1961), in most cases exact similarity will not be achieved. This is due to the complexity of effectively scaling roughness elements and certain geometric characteristics from the prototype to the model. Consequently, the goal of any model study should be to investigate the qualitative properties that influence prototype performance.

For the current study, which dimensionless parameter influences flow behavior the most depends on flow conditions. During open channel flow in the flume, Froude number similitude will be important. During submerged flow in the flume, Reynolds number similitude will be important. For either of these conditions, Reynolds and Froude numbers may be of importance near the sluice gate depending on the gate opening height and the flow conditions in the channel downstream of the gate.

## 2.6 Instrumentation

The following section contains literature review of data collection instrumentation used for experimentation as part of this thesis.

### 2.6.1 Pressure Taps

Pressure taps are small orifices machined in a flow boundary. The orifices are perpendicular to the boundary and connect the flow region with a small cavity on the other side of the boundary. A manometer or transducer is connected to the cavity to measure pressures at the wall of the flow.

Flow over a pressure tap normally induces a sequence of counter-rotating vortices within the tap. These vortices can entrain high speed fluid from the flow into the orifice causing pressures inside the cavity to be higher than the true wall pressures. To minimize these effects, choosing an optimal hole size is crucial. Based on Tavoularis data, practical hole sizes range between 0.5 and 3.0 mm. (Tavoularis, 2005).

### 2.6.2 Particle Image Velocimetry (PIV)

Particle Image Velocimetry (PIV) measures fluid motion by illuminating small tracer particles and from their displacement, a flow velocity field can be determined. PIV in its simplest form can be traced back to the first person gazing at debris in a stream or river with some concept of velocity in mind. Of course, many advances have been made since then. PIV has since advanced to a very accurate, quantitative measurement of fluid velocity profiles in a number of applications.

As mentioned, velocity profiles are measured by the displacement of tracer particles seeded in the flow. Care must be taken when selecting particles for certain applications. The tracer particles are considered as ideal when they (1) exactly follow the motion of the fluid, (2) do not alter the flow or the fluid properties and (3) do not interact with each other (Westerweel, 1997).



Early in the development of PIV, an issue arose regarding the energy required to illuminate fine particles to produce an image of sufficient exposure. With high flows and large turbulence, smaller particles were required to maintain their fidelity to provide accurate velocities. It was discovered that pulsed lasers would provide sufficient energy for PIV applications. The development and use of double-pulse solid-state lasers was a milestone in PIV. The earliest use of Nd:YAG lasers appears to be in 1986 (Kompenhans and Reichmuth, 1986).

Additional details for general PIV measurements are discussed in Akilli et al. (2005).

## Chapter 3 Construction of the S-375 Physical Model

### 3.1 S-375 Prototype

Figure 3-1 shows a side view of the S-375 control structure. The structure is approximately 100 feet in length and consists of a forebay and three nearly identical sluice gates and box culverts. All three of these culverts draw water from the same reservoir and discharge into the same stilling basin. Flow from the forebay into the box culverts is controlled by three automated sluice gates. The box culverts that follow each sluice gate are constructed of 8 ft by 8 ft by 8 ft precast concrete sections with a total length of 84 feet for each culvert. Near the head wall, the first section of each box culvert is part of the forebay and is approximately 4 ft in length. See Figure 3-2 for construction images of the culverts including precast sections. All the information regarding the structure of the prototype culvert was provided by SFWMD.

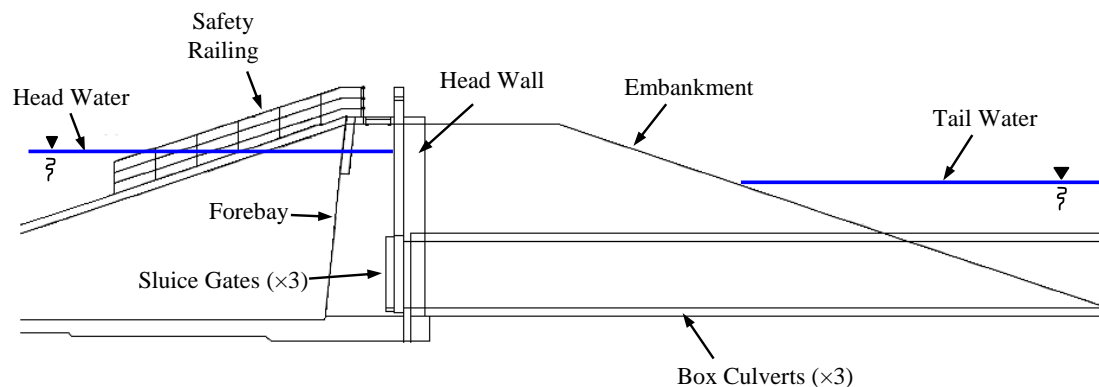


**Figure 3-1 S-375 gate structure and run-out culverts (Gonzalez, 2010)**

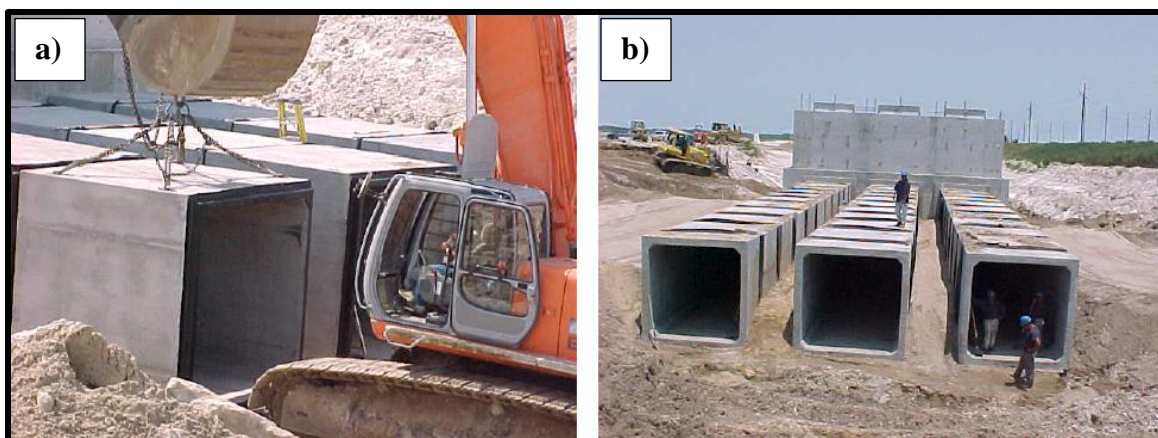


**Figure 3-2 a) Construction installation of precast culvert sections and b) Construction of culverts (Gonzalez, 2010)**

Table 3-1 shows the operational range of the S-375 structure. Upstream stages are given above the NGVD sea level datum. Peak discharge of each of the three culverts is 526 cfs based on information provided by SFWMD. The elevation of the culvert invert is at 4 ft above sea level and for modeling purposes the headwater and tailwater ranges are also specified using the culvert invert as the datum. The peak discharge for the structure corresponds to a peak Reynolds number of  $5.4 \cdot 10^6$ , based on the equivalent diameter of the culvert and the bulk average velocity from the peak flow rate.

**Table 3-1 S-375 Operating conditions**

	Minimum	Maximum
Headwater Stage	17.5 ft NGVD	20.44 ft NGVD
Tailwater Stage	14.5 ft NGVD	18.68 ft NGVD
Headwater (Invert Datum)	13.5 ft	16.44 ft
Tailwater (Invert Datum)	10.5 ft	14.68 ft
Discharge	0 cfs	526 cfs
Full culvert Reynolds No. (est.)	-	$5.4 \cdot 10^6$

### 3.2 Model Type and Scale

For practical reasons, only the central section of the three conveyance sections of the S-375 was modeled. The central section was selected because it is the most symmetric of

the three sections, although the three sections are nearly identical. Only the abutments of the forebay are different and are not expected to significantly impact flow behavior downstream of the sluice gate. The model includes a scaled representation of the central forebay, sluice gate, and box culvert. The tank upstream of the forebay was designed to deliver the scaled range of stages that the prototype is designed to handle. The tail box can be used to control the downstream stage. The tail box was built with high sidewalls so that the range of scaled tailwater values that the prototype is designed to handle could be simulated in the model.

The S-375 model box culvert can flow either partly or completely full. When there is a free surface inside of the box culvert, the flow will be strongly influenced by gravitational forces and the Froude number will be very important. However, if flow into the box culvert is controlled by the upstream sluice gate, viscous forces may be important in the vicinity of the sluice gate, and although the Froude number is dominant in the box culvert, Reynolds number will be important near the gate. When the box culvert is flowing full, viscous forces dominate, and measurements must be scaled based on Reynolds number similitude. So for most of the model tests, Reynolds numbers will be important.

The peak prototype Reynolds number based on the equivalent diameter of the prototype and the bulk average velocity from the peak flow rate, is approximately  $5.4 \cdot 10^6$ . The peak Reynolds number in the model will be lower. An 8:1 scale was chosen for the model based on practical laboratory considerations such as available discharge and space. With a Froude number model, as the size of the model decreases, the flow rate required for the model decreases with the power of  $5/2$ . For Reynolds number models, as the size

of the model decreases the equivalent velocity in the model increases. For a box culvert, we will use the equivalent diameter of the culvert to calculate the culvert Reynolds numbers. The equivalent diameter is 4 times the hydraulic radius. For Reynolds number similarity, the Reynolds number for flow in a rectangular culvert barrel is given as:

$$\frac{4V_m R_m}{\nu_m} = \frac{4V_p R_p}{\nu_p} \quad (3-1)$$

Where  $V$  is velocity,  $R$  is the hydraulic radius of the barrel, and  $\nu$  is the viscosity of the fluid in the barrel. The subscripts  $m$  and  $p$  refer to model and prototype variables, respectively. Since the flume barrel cross section is square, the hydraulic radius of the barrel is  $H/4$  where  $H$  is both the height and width of the barrel. If the hydraulic radius is inserted into equation (3-1), the 4 cancels out and the new similarity condition is:

$$\frac{V_m H_m}{\nu_m} = \frac{V_p H_p}{\nu_p} \quad (3-2)$$

Since the velocity in the culvert equals the culvert discharge divided by the cross sectional area ( $H^2$ ) of the culvert, the discharge can be easily substituted into equation 3-2. If discharge is used instead of velocity in the equation, the similarity condition becomes:

$$\frac{Q_m}{H_m \nu_m} = \frac{Q_p}{H_p \nu_p} \quad (3-3)$$

Rearranging equation (3-3) yields:

$$Q_m = Q_p \cdot \frac{H_m \nu_m}{H_p \nu_p} \quad (3-4)$$

Since the model is 1:8, the ratio of  $H_m/H_p$  is 1/8. So if the viscosity in the model is the same as in the prototype, the discharge in the model will be 1/8<sup>th</sup> of the discharge in the prototype to achieve the same Reynolds numbers. This discharge will be almost seven times higher than what can be provided in the laboratory. However, the Reynolds numbers in both the prototype and model will be quite high, and at high Reynolds numbers, flow behavior becomes independent of Reynolds number. Thus, despite differences in Reynolds numbers, the flow behavior in the model and prototype will be similar. However, for best similarity the Reynolds number in the model and prototype should match, so the flows observed in the model do not represent the full range of flows that were observed in the prototype.

To understand what influences flow behavior in the S375 Box culvert, a dimensional analysis was developed. The most important variables in the present analysis include geometric dimensions, flow variables, and fluid properties. The variables include the following (Refer to Figure 3-3 for a depiction of the geometric variables):

**Universal Variables (variables that apply to the entire model)**

Geometric dimensions:

- The flume width (w)
- The flume length (L)
- The flume height (D)
- The height of the gate opening (d)

Flow variables:

- The discharge per unit width (q)
- The bulk average velocity through the gate opening ( $V_d$ )
- The bulk average velocity in the culvert (V)

- The head water depth (H)
- The tail water depth (T)
- The difference in heads ( $\Delta H = H - T$ ) is of more importance than the heads themselves because the difference is what drives the flow. However, this assumption is not always correct for open channel flow since flow through the gate can be independent of the tailwater if the gate is not submerged. In the present analysis, the model gate will always be submerged so the assumption is valid.

Fluid and other properties:

- The dynamic viscosity of the water in the model ( $\mu$ ).
- The density of the water in the model ( $\rho$ ).
- The gravitational acceleration ( $g$ )

**Local Variables (variables that yield local results)**

Geometric dimensions:

- Local position ( $l$ ) – the distance from the leading edge of the culvert

Flow variables:

- The relative static bed pressure,  $\Delta h$  ( $h-H$ )
- The standard deviation of the relative pressure ( $\Delta h'$ )

When the variables are organized to determine how local pressure is related to relevant universal and local parameters, the parameter functionality is written as:

$$\Delta h = f(q, \mu, \rho, \Delta H, l, L, w, D, d, g) \quad (3-5)$$

Where  $f$  is an arbitrary function determined by empirical analysis. The variables  $q$ ,  $\rho$ , and  $d$  are used as repeating variables: a flow parameter, a fluid property, and a geometric dimension. Dimensional analysis shows that:

$$\frac{\Delta h}{d} = f\left(\frac{\rho q}{\mu}, \frac{\Delta H}{d}, \frac{L}{d}, \frac{l}{d}, \frac{w}{d}, \frac{d}{D}, \frac{gd^3}{q^2}\right) \quad (3-6)$$

The first term inside the function is  $\rho q/\mu$ . Discharge per unit width is equal to the discharge divided by channel width ( $q = Q/w$ ). Substituting in  $V_d d w$  for  $Q$  shows that  $q = V_d d$ , so the first term is the same as  $\rho V_d d/\mu$ . This is the Reynolds number of the gate opening ( $Re_d$ ).

$$\frac{\Delta h}{d} = f\left(Re_d, \frac{\Delta H}{d}, \frac{L}{d}, \frac{l}{d}, \frac{w}{d}, \frac{d}{D}, \frac{gd^3}{q^2}\right) \quad (3-7)$$



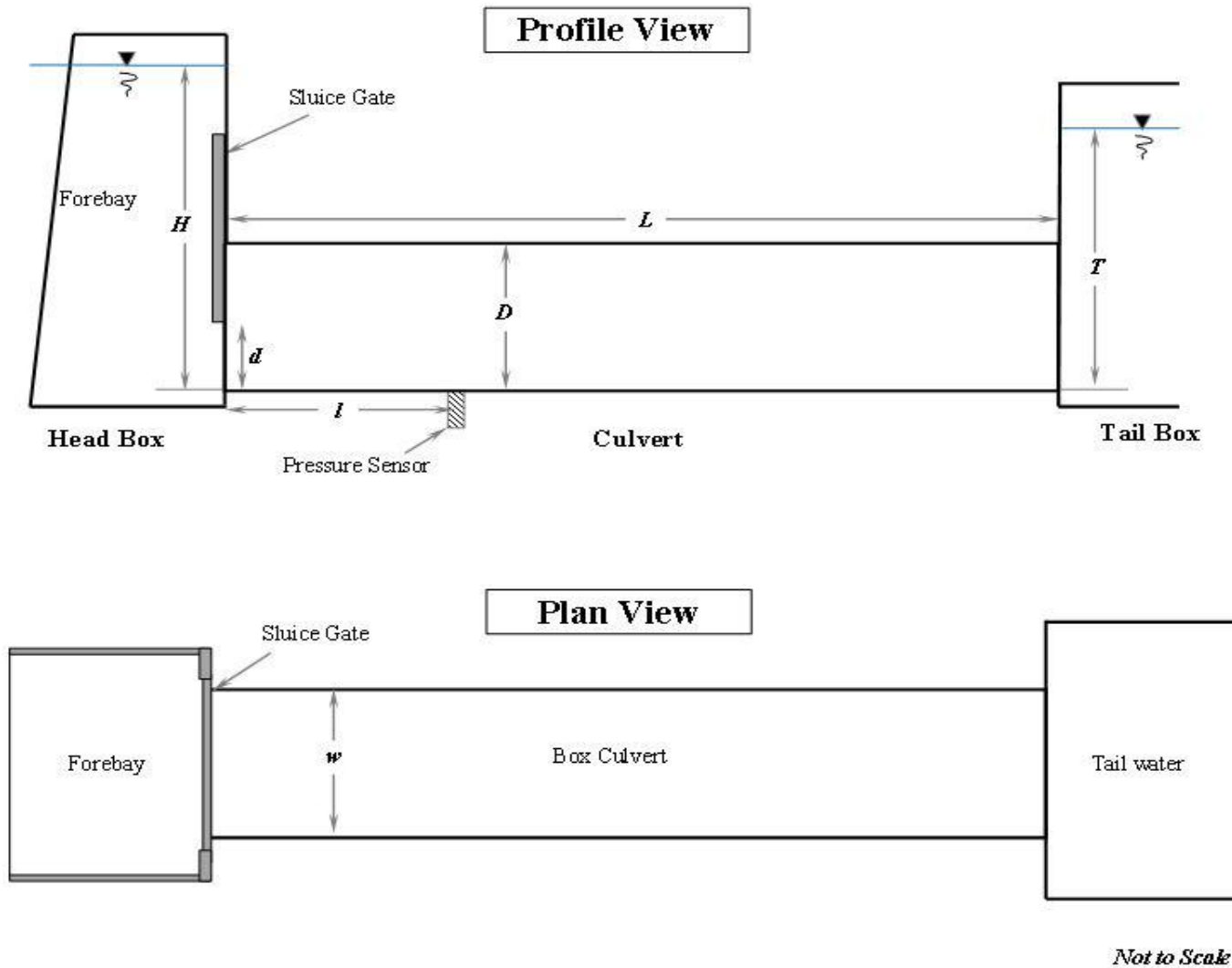


Figure 3-3 Geometric Model Dimensions

The third term can be inverted (from  $L/d$  to  $d/L$ ) and multiplied by the second term to get the head drop per unit length of culvert ( $\Delta H/L$ ). The second term can be replaced with the new parameter.

$$\frac{\Delta h}{d} = f \left( Re_d, \frac{\Delta H}{L}, \frac{L}{d}, \frac{l}{d}, \frac{w}{d}, \frac{d}{D}, \frac{gd^3}{q^2} \right) \quad (3-8)$$

The third term is the ratio of the culvert length to the gate opening height; it can be replaced with the length to height ratio of the culvert ( $L/D$ ) if it is recombined with the sixth term. The fourth term is the ratio of distance downstream of the opening to the gate opening height ( $l/d$ ). The fifth term is the ratio of the width of the culvert to the gate opening height; it can be replaced with the width to height ratio of the culvert ( $w/D$ ) if it is recombined with the sixth term. The sixth term is the ratio of the gate opening to the full gate opening ( $d/D$ ) – this influences the behavior of the recirculation zone downstream of the gate. The last term is rearranged – first inverted and then the square root of it will form a related dimensionless parameter.

$$\frac{\Delta h}{d} = f \left( Re_d, \frac{\Delta H}{L}, \frac{L}{D}, \frac{l}{d}, \frac{w}{D}, \frac{d}{D}, \frac{q}{d\sqrt{gd}} \right) \quad (3-9)$$

The variable  $q/d$  is the same as the average velocity through the gate opening ( $V_d$ ), and the last term is representative of an inlet Froude number ( $Fr_d$ ).

$$\frac{\Delta h}{d} = f \left( Re_d, \frac{\Delta H}{L}, \frac{L}{D}, \frac{l}{d}, \frac{w}{D}, \frac{d}{D}, Fr_d \right) \quad (3-10)$$

The pressure term on the left ( $\Delta h/d$ ) can be adjusted by dividing it by the square of the inlet Froude number.

$$\frac{\Delta h}{d} \frac{1}{Fr_d^2} = \frac{\Delta h}{d} \frac{gd^3}{q^2} = \frac{\Delta h}{q^2/gd^2} \quad (3-11)$$

Again,  $q/d$  is the bulk average velocity at the duct inlet, multiplying the new dimensionless number by two will provide another dimensionless number with the same

functionality. Thus,  $\frac{\Delta h}{V_d^2/2g}$  can replace  $\frac{\Delta h}{D}$  without sacrificing dimensional representation:

$$\frac{\Delta h}{V_d^2/2g} = f\left(Re_d, \frac{\Delta H}{L}, \frac{L}{D}, \frac{l}{d}, \frac{w}{D}, \frac{d}{D}, Fr_d\right) \quad (3-12)$$

The pressure difference given above is actually a difference in pressure heads, and

$\frac{\Delta h}{V_d^2/2g}$  is equivalent to a pressure coefficient, which can be shown by multiplying both the numerator and the denominator by the specific weight of the fluid:

$$\frac{\Delta h}{V_d^2/2g} = \frac{\gamma \Delta h}{\rho V_d^2/2} \quad (3-13)$$

Thus, the functionality of the final parameter set is:

$$C_p = f\left(Re_d, Fr_d, \frac{\Delta H}{L}, \frac{L}{D}, \frac{l}{d}, \frac{w}{D}, \frac{d}{D}\right) \quad (3-14)$$

In which:

$$C_p = \frac{\Delta h}{V_d^2/2g} = \frac{\Delta p}{\rho V_d^2/2} \quad (3-15)$$

$$Re_d = \frac{V_d d}{\nu} = \frac{q}{\nu} \quad (3-16)$$

$$Fr_d = \frac{V}{\sqrt{gd}} = \frac{q}{d\sqrt{gd}} \quad (3-17)$$

### 3.3 Model Construction

Figure 3-4 shows the physical layout of the model. Shown in the model layout are the head tank, the model forebay, the flume barrel, and the tail box. The head tank is 84 ½ inches above the floor, and supplies flow to the model forebay. The head tank is constructed of ¾ inch plywood, reinforced with a steel framework and lined with fiberglass. The head tank is 51 ¼ inches long, 40 ⅝ inches wide and 39 ¼ inch deep. Water is supplied to the head tank from a sump below the floor using a submersible axial pump that can deliver between 1000 and 1300 gpm, depending on the head required in the forebay of the model. More information on the pump is provided in Appendix B-7.

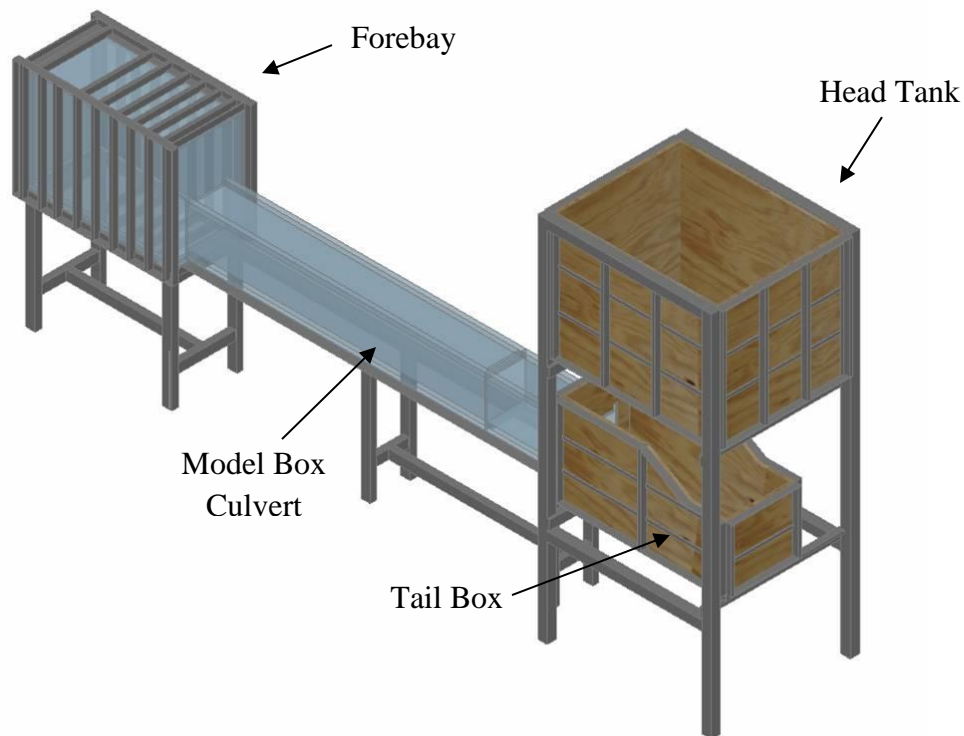


**Figure 3-4 Physical model 3D layout**

The forebay is constructed of ¾ inch Plexiglas, bolted and sealed together with silicone and epoxy. The forebay is 46 inches long, 33 inches deep and 22 inches wide. The bed of

the forebay is 44 ½ inches above the floor. Thus, the flow supplied from the head tank to the forebay can be provided at an elevated pressure if the forebay is sealed. If sealed well enough, the elevated pressures will make it possible for the model to increase Reynolds numbers to levels that are closer to prototype levels than if the water supplied to the forebay is at atmospheric pressure. This will be true both when the sluice gate is fully open and when it is partially open. The forebay structure was reinforced with a steel framework to provide additional strength to the forebay in case operating the model at elevated pressures is necessary.

At the entrance to the model culvert is a sluice gate, as shown in Figure 3-5. The sluice gate is constructed of ¼ inch aluminum and can be vertically adjusted, sliding within aluminum slots. The gate height is controlled by a threaded rod system attached to the removable lid of the forebay. A ruler has been attached to this system, without interference to the flow, to measure the gate opening.

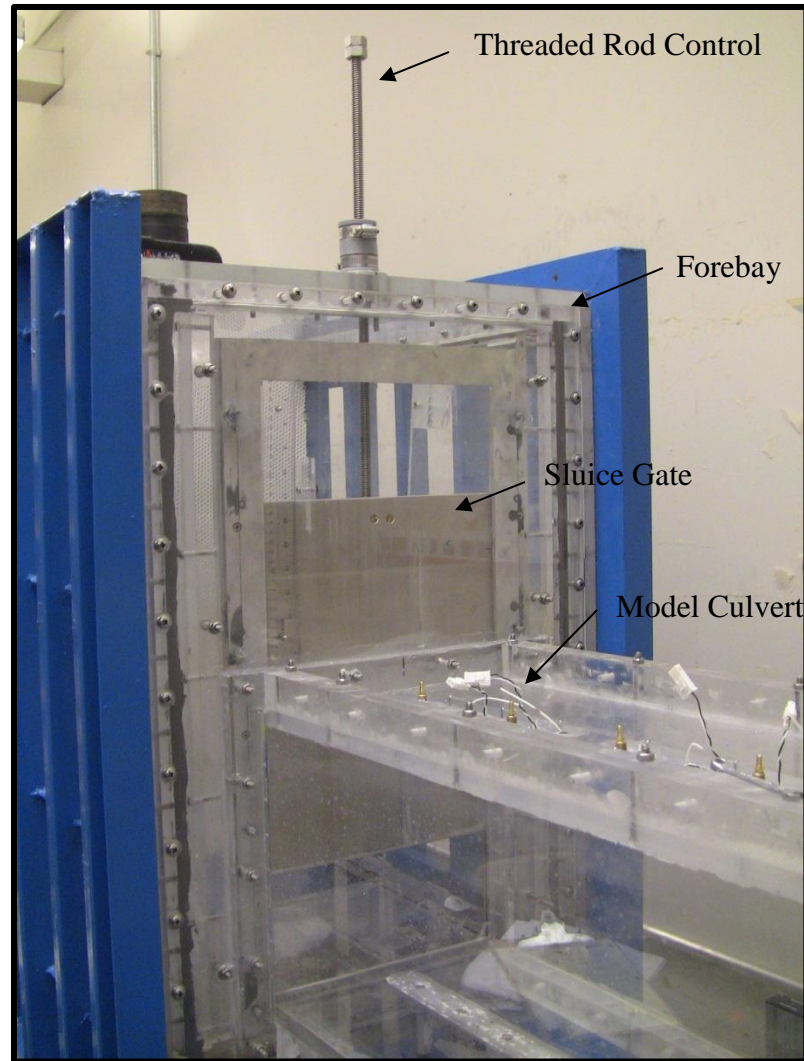


**Figure 3-5 Sluice gate and threaded rod control**

A false bed was constructed just upstream of the sluice gate inside the forebay. This false bed replicates the upstream portion of the gate control structure of the prototype. The false bed is constructed of Plexiglas. The false bed is 1.36 inches below the bed of the model culvert and is 14 inches in length and 18 inches wide.

The flume barrel section was constructed using  $\frac{3}{4}$  inch Plexiglas. See Figure 3-6 for an image of the model culvert barrel section. The flume barrel is  $126\frac{13}{16}$  inches long

(10.57 feet) with a cross sectional area of one square foot. A removable steel framework was constructed to provide support if necessary during operation with elevated pressures. All Plexiglas seams were glued and or bolted together and sealed with silicone.

The length of the flume barrel structure was beyond the orderable length of Plexiglas, thus the barrel of the flume has two sections. Care was taken to construct the connection between the sections so that it was as smooth as possible to limit its effects on the flow. The location where the sections were sealed together is downstream of all pressure measurement equipment and will not affect pressure measurements.

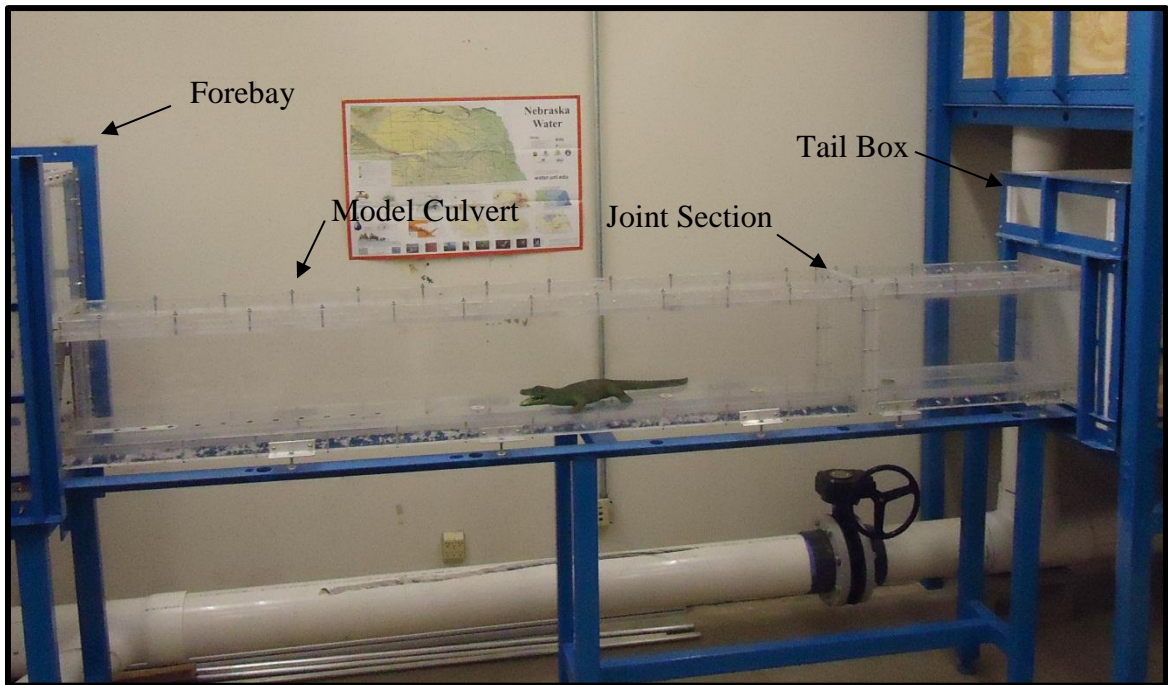


**Figure 3-6 Model Culvert Barrel Section**

The tail box was constructed primarily of  $\frac{3}{4}$  inch plywood lined with fiberglass and supported by a steel framework. The upstream face of the tail box was constructed of  $\frac{3}{4}$  inch Plexiglas to allow for a more effective seal with the flume barrel. The tail box is 52

½ inches long, 22 ½ inches wide. The inlet depth of the tail box is 30 ½ inches, with an outlet depth of 21 ½ inches at the downstream section where the outlet pipes exit the tail box. The bed of the tail box is 4.41 inches below the end of the flume barrel. Aluminum slots are located inside the tail box 27 inches downstream of the flume barrel opening to allow Plexiglas stop logs of varying height to be placed perpendicular to the flow to control the downstream stage in the model.

Supply and return piping was installed to and from the sump tank. An 8 inch supply and return pipe enters the head tank. The 8 inch supply line is split at a tee where flow travels to the forebay and excess is routed to the head tank.

The flow to the forebay is controlled by a butterfly valve. Downstream of the butterfly valve the flow splits into two 6 inch lines which enter the forebay through the bed. The pipes in the forebay were perforated with ¾ inch holes on the upper half of the pipes to reduce turbulence in the forebay. A flow straightener was installed to decrease turbulence and to produce a more uniform flow regime in the forebay upstream of the sluice gate. Refer to Figure 3-7 for a depiction of the aforementioned components of the flume model.





**Figure 3-7 Model head tank, forebay, culvert, tailbox, and piping.**

After the flow passes through the flume barrel into the tail box, two 8 inch pipes route the flow into a V-notch weir tank before the flow returns to the sump tank. Figure 3-8 shows the weir tank. The V-notch tank was constructed of aluminum and bolted to a steel frame and then sealed with epoxy. The tank is located just downstream of the tail box and is just upstream of the sump. The downstream end of the tank is a 30 degree V-notch weir. The weir was calibrated to measure the flow rate in the model.



**Figure 3-8 V-Notch weir tank**

## Chapter 4 Instrumentation

### 4.1 Pressure Transducers

Transducer slots were machined into the bed and crown of the flume. Aluminum inserts were constructed that fit into the slots. A total of 12 Pressure taps were drilled into the inserts at 3 inch intervals from the entrance of the flume to 36 inches downstream. The slot inserts could be replaced with inserts with different pressure tap spacing if necessary. The inserts could also be replaced with Plexiglas inserts to improve visibility into the flume. Figure 4-1 shows slots with aluminum inserts just downstream of the sluice gate before installation of pressure transducers.



**Figure 4-1 Aluminum slot inserts**

The pressure sensors used are PX309 pressure transducers from Omega. The transducers were placed along the slot inserts in the bed of the flume. The pressure transducers are located along the bed at 3, 6, 9, 12, 18, 24, 30, and 36 inches downstream of the flume

entrance. See Figure 4-2 for the layout of the sensors along the slot inserts at the bed of the flume.

These transducers feature a wide variety of pressure ranges and rapid response to pressure fluctuations. The information sheet for the pressure sensors can be found in Appendix B-1. Manometers were placed in various locations in the slots with the pressure sensors. These manometers, four on the flume bed and six on the flume ceiling, help with the calibration of the pressure sensors as well as verification of the pressure sensors readings. The manometers on the bed of the flume were located 15, 21, 27, and 33 inches downstream of the flume entrance. The manometers on the crown of the flume were located at 3, 9, 15, 21, 27, and 33 inches downstream of the flume entrance.

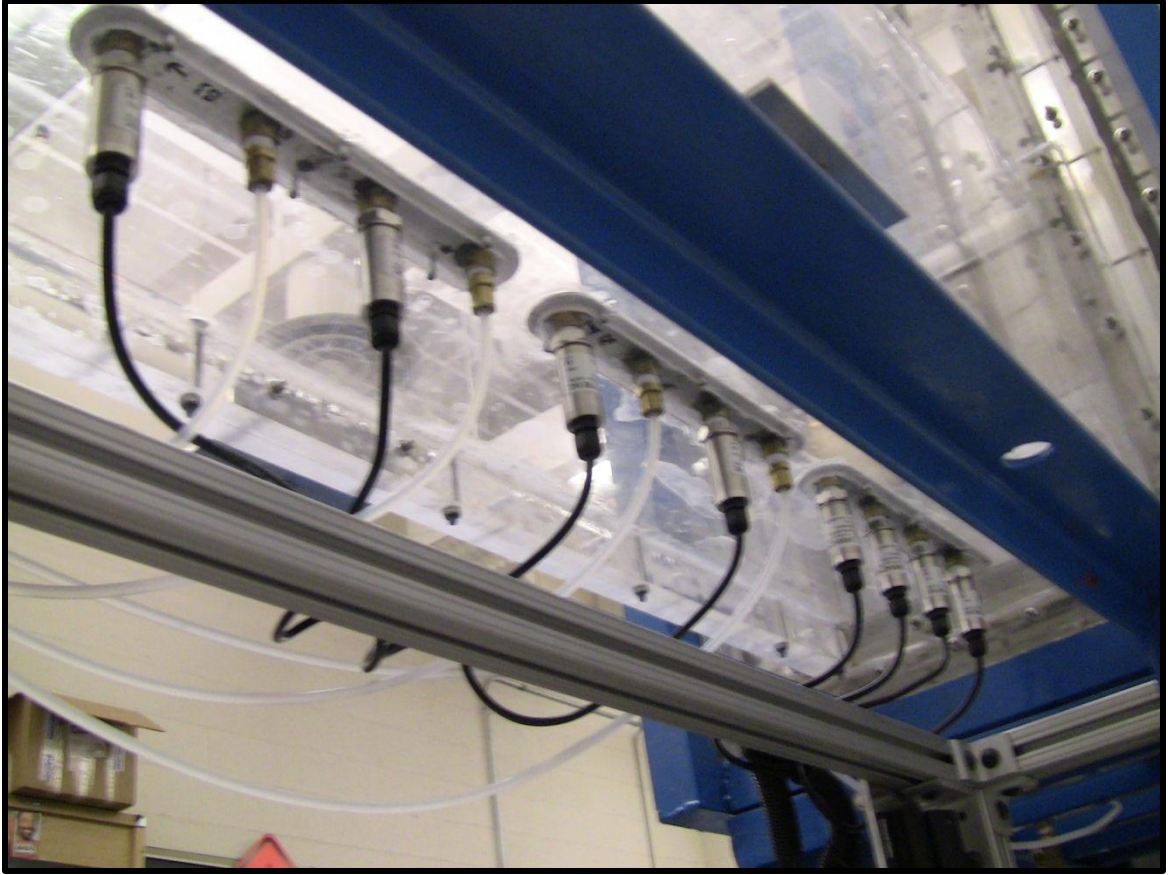


**Figure 4-2 Pressure transducers and manometers installed in the slot inserts along the flume bed**

Pressure was recorded using an NI USB-6210 data acquisition system from National Instruments. Information about the data acquisition system is given in Appendix B-2. Two of these USB compatible systems were purchased to accommodate as many as 20 pressure transducers at once. The pressure measurements were synchronized with other system measurements described in a later section.

## **4.2 Pressure Transducer Calibration**

The PX309 series pressure transducers located on the bed of the flume were calibrated. Water was pumped into the flume using a small sump pump. The tail box weir was used

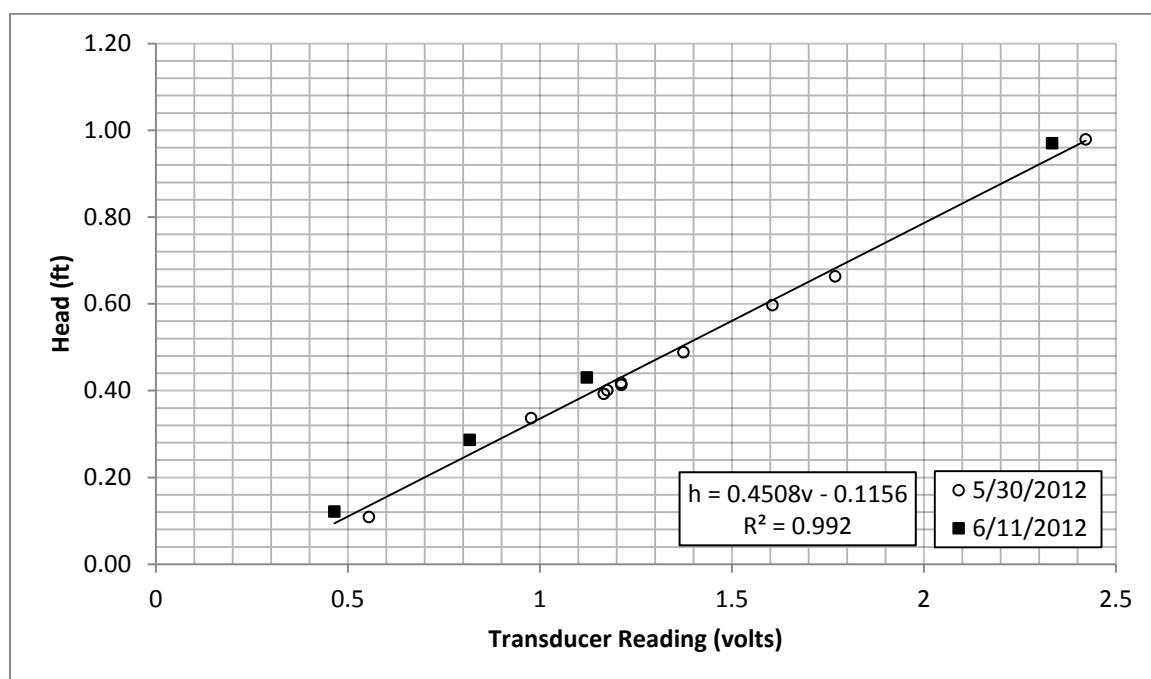


to maintain a constant head in the flume. Calibrations were run using different head levels created by using various weir heights. A pressure head reading was taken from the head tank manometer and the manometers that span the bottom of the flume before and after running the Lab View software for the transducers. Pressure head readings were taken before and after each experiment to ensure equilibrium conditions were maintained throughout the calibration procedure. The Lab View software was set to collect 30,000 pressure transducer measurements per sensor at a rate of 500 Hz. Eleven calibration tests with different head levels were conducted on 5/30/12, and four additional tests were conducted on 6/11/12.

The data from the pressure transducers for each experiment were graphed using Microsoft Excel. The voltage readings from each transducer were time-averaged and plotted against the observed head in the flume. The y-axis is pressure head (h) in feet of water and the x-axis is the transducer reading (v) in volts. See Figure 4-3 for a sample graph of the calibration results. For each sensor, a line was fit to the data and the standard deviation was calculated. See Table 4-1 for regression equations and standard deviation data. Each linear regression equation was used to convert transducer voltage readings to head in feet for each respective sensor. The sensor with the largest observed deviation was sensor 4 with a standard deviation pressure head of 0.0266 ft of water. All other sensors had a standard deviation in the range of 0.008 to 0.017 ft of water.

**Table 4-1 Pressure transducer linear regression equation and standard deviations**

Sensor	Pressure Head (ft of water)	Standard Deviation (ft of water)
0	$h = 0.4581v - 0.1252$	0.0170
1	$h = 0.455v - 0.1057$	0.0125
2	$h = 0.4577v - 0.1273$	0.0081
3	$h = 0.458v - 0.1385$	0.0101
4	$h = 0.4508v - 0.1156$	0.0266
5	$h = 0.4593v - 0.1351$	0.0087
6	$h = 0.4599v - 0.1223$	0.0155
7	$h = 0.4578v - 0.116$	0.0142

**Figure 4-3 Pressure sensor 4 sample calibration showing both dates of testing and the resulting regression equation**

### 4.3 PIV System

The PIV System consists of a dual pulse Nd:YAG Laser system, a custom optical system, a high resolution camera, and a delay generator. Information on all associated

appurtenances is located in Appendix B. Information on the Nd:YAG Laser system can be found in Appendix B-3.

The custom optical system carries the Nd:YAG laser pulses from the laser head to the flow and modifies it into a light sheet. The optical components consist of four first-surface mirrors that reflect the laser pulses at right angles until they reach the test section where the flow is measured. Each laser pulse is directed through a set of aluminum tubes that are mounted on an aluminum frame. At the end of each tube is a mirror that reflects the laser 90 degrees. The custom laser guide ends below the flume barrel and is attached to the steel support structure where a set of three cylindrical lenses expand the laser into a light sheet that illuminates a thin section parallel to the flow. The custom optic system can be seen in Figure 4-4.



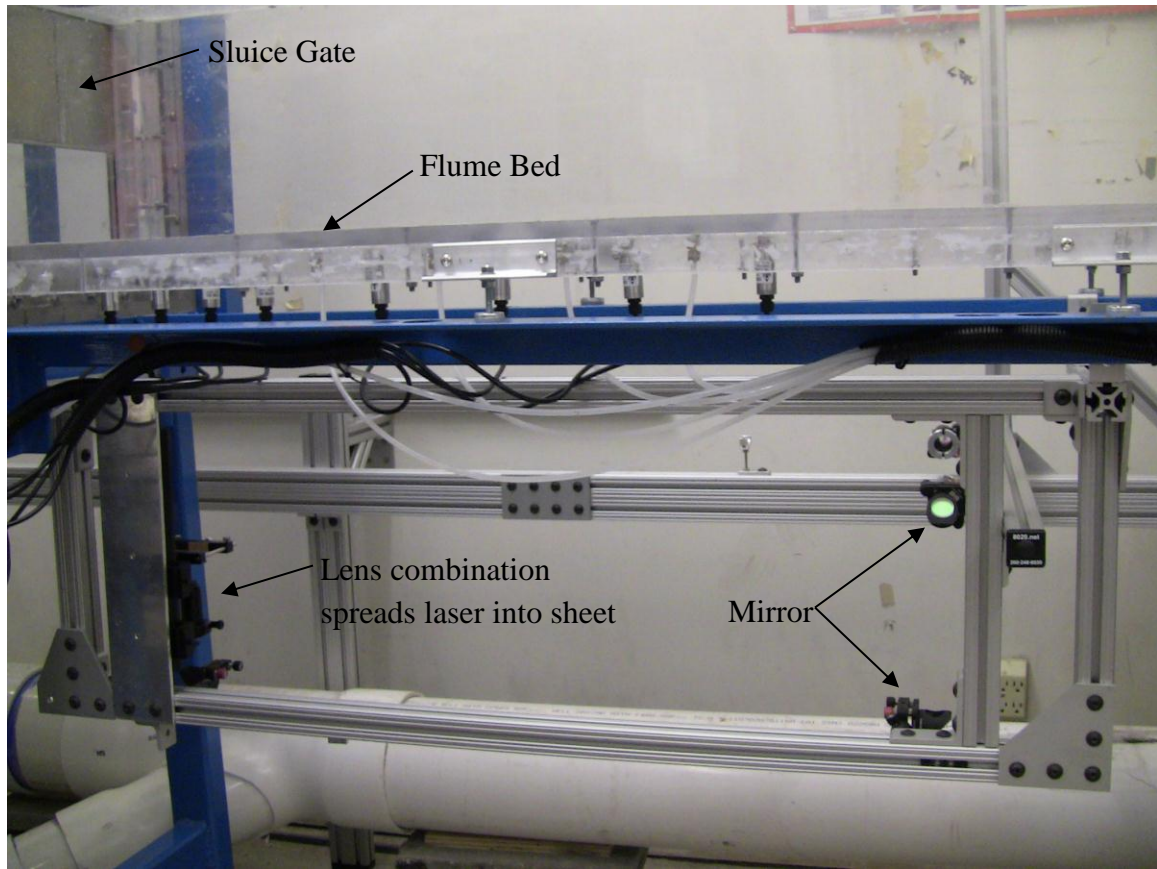


**Figure 4-4 Custom PIV optic system**

The flow was seeded with small particles which reflect the laser sheet as it passes through the water. These reflections are recorded by camera images. Two pulses are fired by the laser for each velocity field measurement. The pulses are separated by a brief interval of time. During the time between the two pulses, the particles in the flow travel a short distance. An entire velocity field is measured in the flow by recording images of the two pulses, calculating the distances that each particle traveled and converting the displacement measurements into velocities by dividing the distance traveled by each particle by the time interval between measurements.

For the PIV data to be correctly analyzed, the distance scale at the location of the images had to be accurately determined. To accomplish this, a scaled grid was attached to a rectangular piece of acrylic and placed parallel to the flow at the location of the light sheet that the camera was imaging. A picture was taken and uploaded to the Labview software. The software allowed the user to determine the distance scale at the location of the light sheet. This was accomplished by tracing the grid of known dimensions on the image collected by the software.

The software determined the ratio of pixels to distance. The determined pixel to distance ratio for the performed experiments was 34.35 pixels per centimeter. The actual distance the particles traveled was determined by dividing their travel distance in pixels by this pixel to distance ratio. Additionally, a ruler was placed on the bed of the flume at the location of the camera frame. This made it possible to determine the location of the pressure sensors on the PIV images.

The camera selected for this project was a Prosilica GT1290. This camera was capable of measuring two images with a very short time interval between them. The camera was triggered immediately before the first laser pulse, and then triggered a second time before the second laser pulse. The two images were transferred to the data acquisition system which recorded both images. Information on the camera specifications is located in Appendix B-4.

This image recording method requires a delay generator to fire the laser and to trigger the camera. For the Prosilica GT1290 system, the delay generator is triggered by a pulse from the computer controlling the system. The delay generator then triggers the camera

and laser, controlling their timing to produce the specified separation time between light sheets and images. Information on the delay generator is located in Appendix B-5. For more detailed information on the timing of the instrumentation, refer to section 4.4.

For safety purposes, Sperian/Uvex YAG/KTP safety goggles were used when operating the laser. The specifications for these goggles are given in Appendix B-6.

#### **4.4 Instrumentation Timing Set Up**

Labview software was used to control the instrumentation for gathering pressure and velocimetry data. A program was written to control the instrumentation and to set delays and timing schedules. Once the program was initiated, the Analog/Digital (A/D) Boards were armed. Once armed, the A/D Boards began collecting pre-samples. A user-defined number of pre-samples were retained for each test. Once the data collection was enabled, the initial video output strobe from the camera triggered the video strobe divide-by-two sequencer, the user-defined number of pre-samples was stored, and collection of data samples was initiated. The divide-by-two sequencer divides the camera video strobe, which is 1/30th of a second, by two, so that only one pulse is transmitted to the delay generator for every two camera images. The divided output strobe triggers the delay generator which in turn triggers the laser sheet twice – once at the end of a camera frame and once at the beginning of the following frame. The timing sequence for the PIV instrumentation is shown in a grid format in Figure 4-5.

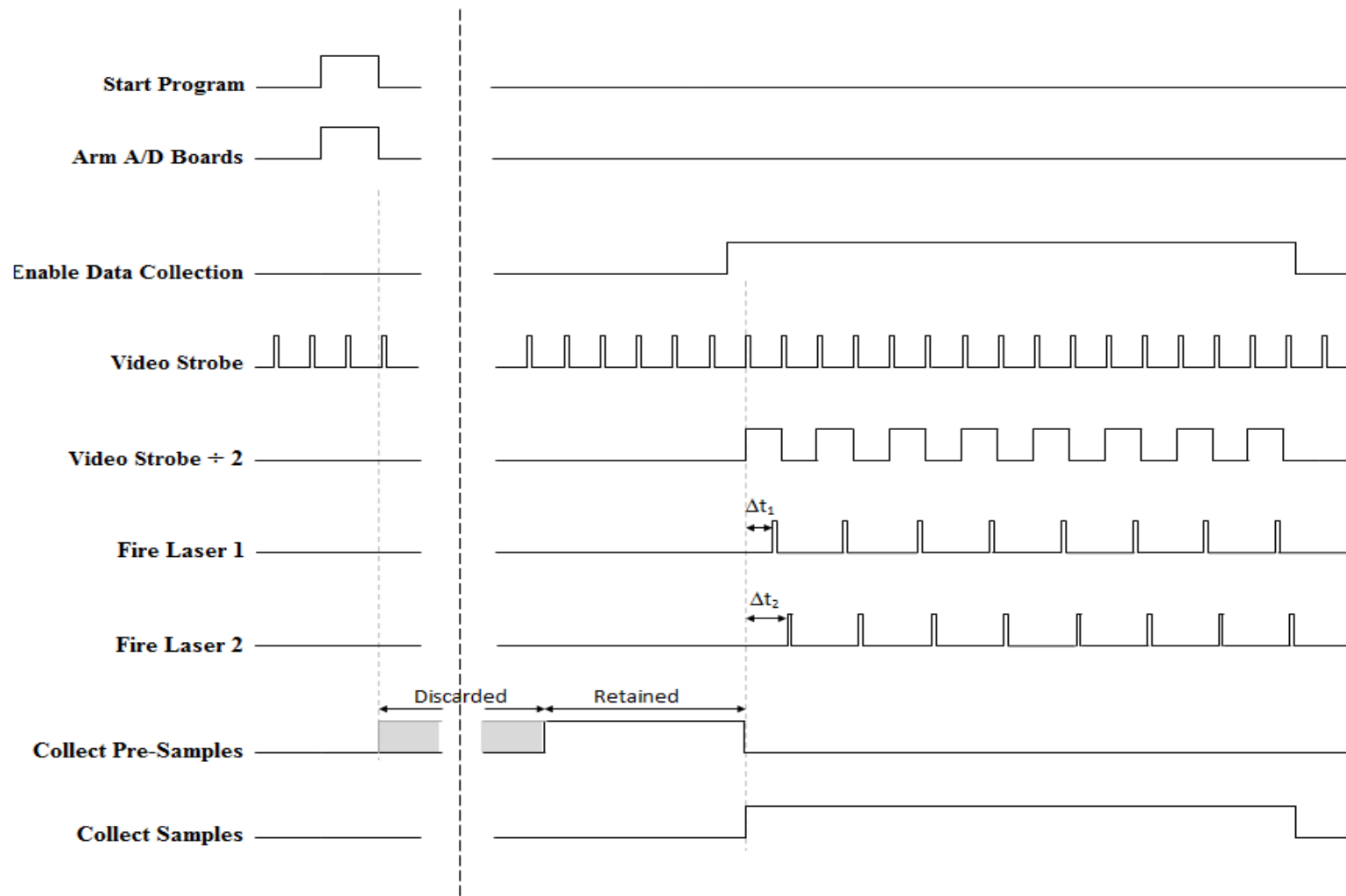


Figure 4-5 PIV Instrumentation timing grid

#### 4.5 V-Notch Outlet Weir

The 30 degree V-notch weir was located just downstream of the tail box and was used to measure the flow rate in the flume. To accurately determine flow rate using the weir it was calibrated using a weigh tank. Head above the weir was measured using a point gauge, and flow was determined by the weight of water released during a known period of time. Forty three tests of varying head levels were carried out. Measurements were based on the following flow rate equation of a V-notch weir.

$$Q = \frac{8}{15} C_d \sqrt{2g} \tan \frac{\theta}{2} H^{5/2} \quad (4-1)$$

Where Q is flow rate in cfs,  $C_d$  is the coefficient of discharge, g is the gravitational acceleration,  $\theta$  is the angle of the V-notch in degrees, and H is the head above the weir.

The head to the 5/2 power was plotted versus the flow rate. A line was fit to the data with a fixed y-intercept at the origin (See Figure 4-6 below). The linear equation of that line was used to calculate flow rate based on measured head levels above the weir.

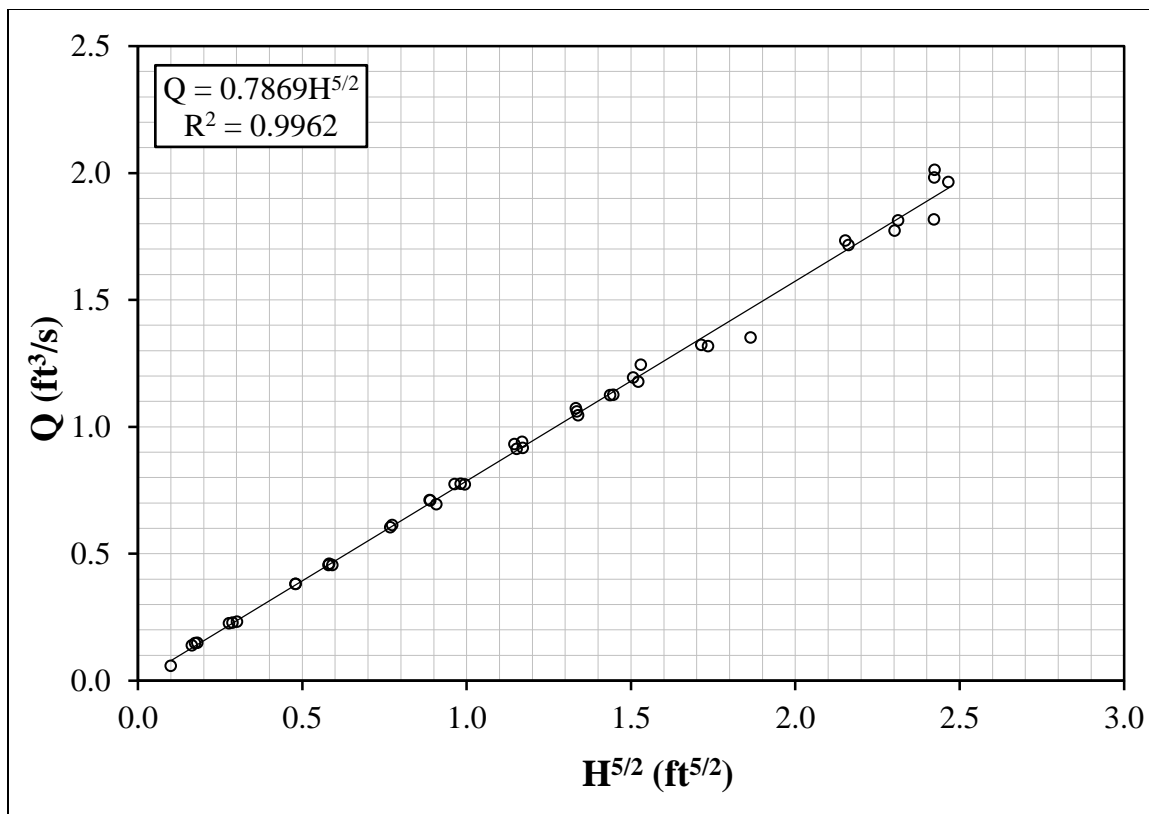


Figure 4-6 V-notch weir flow rate calibration

## Chapter 5 Measurements and Methods

### 5.1 Introduction

Experiments focused primarily on pressure fluctuation and velocity field measurements for submerged flow. Eight experiments were conducted in the flume. The experiments were classified by gate opening. Seven experiments were conducted with gate openings ranging from 3 inches to fully open in increments of 1.5 inches. This corresponded to gate openings ranging from 2 ft to a fully open gate in increments of 1 foot in the prototype. Flow conditions corresponded to the computational conditions used by SFWMD in their numerical studies. Additionally, one experiment was run at a gate opening and forebay and tail box head differentials that closely matched SFWMDs numerical results that produced the largest bed pressure fluctuations. The critical condition corresponded to a gate opening of 4.875 inches in the model.

### 5.2 Physical Model Measurements

To begin, all valves were checked to insure proper settings. Then the pump was initiated. The sluice gate was then set to the corresponding height of the current experiment. The butterfly valve and the tail box weir height were then adjusted to control the stage in the forebay and the tail box respectively. After the flow reached equilibrium, all settings were recorded. All manually recorded settings were collected both before and after each experiment to insure equilibrium was maintained throughout the experiment.

The settings recorded for each experiment were as follows:

- Gate height
- Manometer readings – manually recorded readings for manometers located in the forebay, flume bed (15, 21, 27, and 33 inches downstream of flume entrance), tail box, and V-notch outlet weir.
- Temperature
- Tail box weir height (this controls stage in the tail box)
- PIV image file names
- Calibration image file name
- Laser fire delay time
- Laser separation time
- Pressure transducer pre-sample amount
- Pressure transducer sample amount
- Sample frequency
- PIV images
- Pressure transducer readings

See Figure 5-1 for a sample data sheet.



S-375 FLUME TESTS				
GENERAL INFORMATION				
Test Name:	G06.00 H25 T18 D#		V-Notch Weir Angle:	29.3 degrees
Date:	5/25/2012		V-Notch Datum:	31.9 cm
Time:	11:30 AM			
	V-Notch Weir:	Reading	Head	
	Start:	79.12	47.22	cm
	End:	79.12	47.22	cm
Water Temperature:	21.0° C			
Gate Opening:	15.24 cm			
	6 in			
Tail Stop Log Height:	35.8775 cm			
PRESSURE INFORMATION				
Bottom Pressure Sensors File Names:	G3 H30 T17 D# C1 P2.csv		Presamples:	100
Top Pressure Sensors File Names:	G3 H30 T17 D# C1 P1.csv		Samples:	30100
			Sample Frequency:	500 Hz
		Start	End	Datum
Gate Setting (cm):		19.43	19.43	4.19
Head Water Elevation (in):		24.50	24.50	3.25
Tail Water Elevation (in):		18.00	18.00	
		Range	Average	Datum
Manometer Tap A (in):		13.70	14.50	14.10
Manometer Tap B (in):		14.40	15.10	14.75
Manometer Tap C (in):		15.10	16.30	15.70
Manometer Tap D (in):		16.30	17.10	16.70
PIV INFORMATION				
Image File Names:	G6 H25 T18 D# ###.bmp			
Calibration File Name:	Calibration Image 5-16-12.bmp			
Laser Fire Delay Time:	32.5 mS			
Separation Time:	1 mS			

Figure 5-1 Data Sheet for Experiment G06.00

### 5.3 PIV Measurements

The data collection software recorded and saved the PIV images to their selected destination folders. For each experiment, six data collection runs were completed. Each run consisted of 180 PIV image pairs (360 total images). The 180 image pairs were collected at a rate of 15 pairs per second corresponding to 12 seconds of images for each data collection run and one minute and twelve seconds of image data per experiment.

The viewing area of the camera was from 4 inches downstream to 18.5 inches downstream of the sluice gate, spanning the entire height of the flume. The camera captured particles in the flow illuminated by the laser light sheet which was located approximately 1.5 inches from the center of the flume towards the left descending bank.

The data were then analyzed using the computer software Flow Field Captor. The software utilized a cross correlation method to interrogate 64 by 64 pixel sections of the image. Each pixel section corresponds to a 1.86 cm by 1.86 cm flow region based on the calculated pixel to distance ratio of 34.45. The analysis of the flow region produced velocity vectors at a user defined grid within the image. The grid used in the current study spanned 37 columns and 27 rows for a total of 999 vectors per image pair. These columns and rows were spaced apart by 32.75 pixels. This spacing and grid set up was selected so that vector columns were located at the location of the pressure sensors in the image field. This allowed velocities to be measured at the exact location of pressure transducer readings. The grid was also on an x-y coordinate system for ease of set up and ability to know exact locations in the vector field. The x-axis was in the streamwise

direction, and the y-axis was perpendicular in direction between the flume bed and crown.

During the cross correlation calculations, some interrogation locations produced faulty vectors. This was primarily due to insufficient illumination of particles in portions of the image and or entrained air bubbles in the flow circulating in the hydraulic jump roller near the sluice gate entrance. The software allowed both automatic and manual filtering of these inaccurate or faulty velocity vectors. Each of the 180 image pairs was analyzed and filtered for each of the six data sets per experiment. The automatic filter settings needed to eliminate these vectors varied depending on the experiment parameters.

The automatic filters used included minimum and maximum velocity constraints in either the x or y-direction. These velocity constraint filters were applied to all or portions of the flow field depending on the experiment. For example, minimum x-directional velocity constraints were used in portions of the flow where negative or small velocities were not probable; such as in the region of the jet just downstream of the sluice gate when the gate has a small opening height.

Air bubbles were entrained in the forebay and carried into the recirculation zone where they accumulated at the crown of the flume just downstream of the sluice gate. The air bubbles were recirculated by the flow, interfering with PIV measurements. To reduce the number of faulty PIV vectors caused by air bubbles, entrained air was removed using a very small vacuum pump. The pump was attached to unused pressure transducer taps in the crown of the flume. The pump pulled the air out of this location through tubes attached to the pressure tap holes. The pump was started prior to running a test and once

the air was removed the pump was disconnected, the tubes were closed off, and the test run was initiated.

#### **5.4 Pressure Transducer Measurements**

The data collection software recorded and saved the pressure transducer readings to their selected destination folders. For each experiment, six data collection runs were completed. Each run consisted of 30,100 pressure readings per sensor and 100 pre-sample transducer readings. This corresponds to just over 60 seconds of pressure transducer readings for each collection run and over 6 minutes of total readings per experiment.

The data collected by the software for each data set of an experiment were compiled into a single spreadsheet. The calibration equation for each sensor was applied to the data to convert the readings to pressure in feet of water. Time-averaged, maximum, and minimum pressures were calculated for each sensor.

## Chapter 6 Results

### 6.1 Introduction

Results were obtained using the equipment presented in Chapter 4. The equipment used for data acquisition was affixed to the constructed flume model as described in Chapter 3. The data were collected using the means presented in Chapter 5. The data collected included physical model measurements, PIV velocity measurements, and pressure measurements in the model. The data were processed using the methods described in Chapter 5.

A total of 8 experiments of varied settings were run in the model flume. Each experiment contained 6 data sets containing both PIV velocity and pressure measurements. Refer to Table 6-1 for a summary of experiment data and information. One non-standard PIV experiment was also completed in addition to the eight experiments previously mentioned. The results of these experiments are presented in this chapter.

**Table 6-1 Experiment Data Collection Summary**

<b>Experiment</b>	<b>Date</b>	<b>Name</b>	<b>Gate Height (in)</b>	<b>Discharge (cfs)</b>	<b>Headwater (ft)</b>	<b>Tailwater (ft)</b>	<b>Temperature (°F)</b>	<b>Reynolds #</b>
1	5/25/2012	G03.00	3.0	1.58	2.21	1.39	70.30	1.55E+05
2	6/12/2012	G04.50	4.5	2.26	2.10	1.30	64.90	2.05E+05
3	5/24/2012	G05.00	4.875	2.39	1.84	1.05	69.80	2.32E+05
4	5/25/2012	G06.00	6.0	2.35	1.77	1.50	69.80	2.28E+05
5	6/12/2012	G07.50	7.5	2.50	1.64	1.34	65.30	2.29E+05
6	5/25/2012	G09.00	9.0	2.53	1.54	1.52	68.90	2.43E+05
7	6/12/2012	G10.50	10.5	2.51	1.49	1.30	66.20	2.32E+05
8	5/25/2012	G12.00	12.0	3.01	1.54	1.52	68.90	2.89E+05

Pressure Data Collection: One (1) minute of data per data set. Six (6) total data sets per experiment. Eight (8) sensors in the bed of the flume.

PIV Data Collection: Twelve (12) seconds of collection per data set. Six (6) data sets per experiment.

Reynolds number based on equivalent model diameter and measured peak flow rate.

## 6.2 Average Velocity Fields

The filtered PIV results from the six data sets of each experiment were compiled into a single merged velocity vector file. The Flow Captor software was used to average the velocity vectors at each location on the defined grid to produce an average velocity vector field for each data set. A spreadsheet was then used to find the combined average velocity field for the experiment using the averaged velocity vectors from each of the six data sets. A weighted average was used to combine data from the six data sets since the filtering process removed varying numbers of vectors from each data set. In this way, the 12 seconds of PIV data collected for each of the six data sets could be combined to form an average velocity distribution based on 72 seconds of PIV data.

Average velocity fields were developed for each of the eight experiments. To display the average velocity fields, average velocity vectors were plotted on a velocity contour map. The contour maps provide good visualization of the average velocities seen within the flume for each experiment. Two contour maps were developed for each experiment. Contour maps were developed at two scales: a small vector scale to more clearly show vectors in the high velocity region and a large vector scale to more clearly show vectors in the recirculation zone. The recirculation zone is the low velocity area formed above the high velocity jet, where flow is recirculated and entrained back into the flow jet. The Experiment G12.00, with the fully opened gate, did not require a map for both a small and large vector scales because the velocities did not vary substantially across the flow field. Refer to Appendix A for the average velocity field contour maps of each experiment.

The average velocity contour maps allow for a broad understanding of the velocity fields associated with each experiment. Low gate setting experiments, such as G03.00 and G04.50, clearly show the high velocity jet at the bottom of the flume at the gate opening. These experiments are uniquely different from experiments with high gate settings, in which the recirculation zone is very small or non-existent. The high velocity jet associated with low gate settings push the recirculation zone farther downstream than experiments with higher gate settings.

As the gate opening increases, the strength of the jet decreases, causing the recirculation zone to move farther upstream, becoming more visible in the viewing extents of the PIV camera. The center of the recirculation zone can be easily identified by a low velocity contour color (dark blue) on the maps. For example, Figure A-3b in Appendix A clearly shows the center of the recirculation zone for test G05.00.

The largest velocities in the negative x-direction, or upstream direction, are located directly above the recirculation zone near the crown of the flume. The largest velocities in the positive x-direction are within the jet near the gate opening.

Both the jet and the recirculation zone are important in understanding flow behavior for each test. The high speed jet zone drives the flow, entraining water from the recirculation zone. The recirculation zone has a low velocity and pressure because of the enclosed nature of the flow. As flow is recirculated, pockets of low velocity fluid are carried off with the high speed jet flow and are transported to the flume bed. The pockets of fluid are carried by turbulent flow structures that form in the recirculation zone and travel to the bed where they influence the observed pressures.



### 6.3 PIV Observed Turbulent Flow Incursions

Experiments with low gate settings that produced a high velocity jet and formed a recirculation zone were examined, revealing many turbulent structures. The structures formed in the recirculation zone and traveled within the recirculation zone, through the jet, and towards the flume bed. One of the six PIV data sets for the G05.00 experiment was analyzed to produce the example shown in Figure 6-1 of a turbulent structure traveling from the recirculation zone to the bed.

The images of the flow incursion in Figure 6-1 show velocity vectors overlaid on a contour map. The contour map is representative of the y-directional velocity in the flow. A white circle has been imposed on the image to identify the flow incursion structure, showing its location and propagation through the flume.

As the turbulent structures move towards the bed of the flume and into the jet stream, they are carried by the velocity of the jet in the flow and can be seen translating downstream.

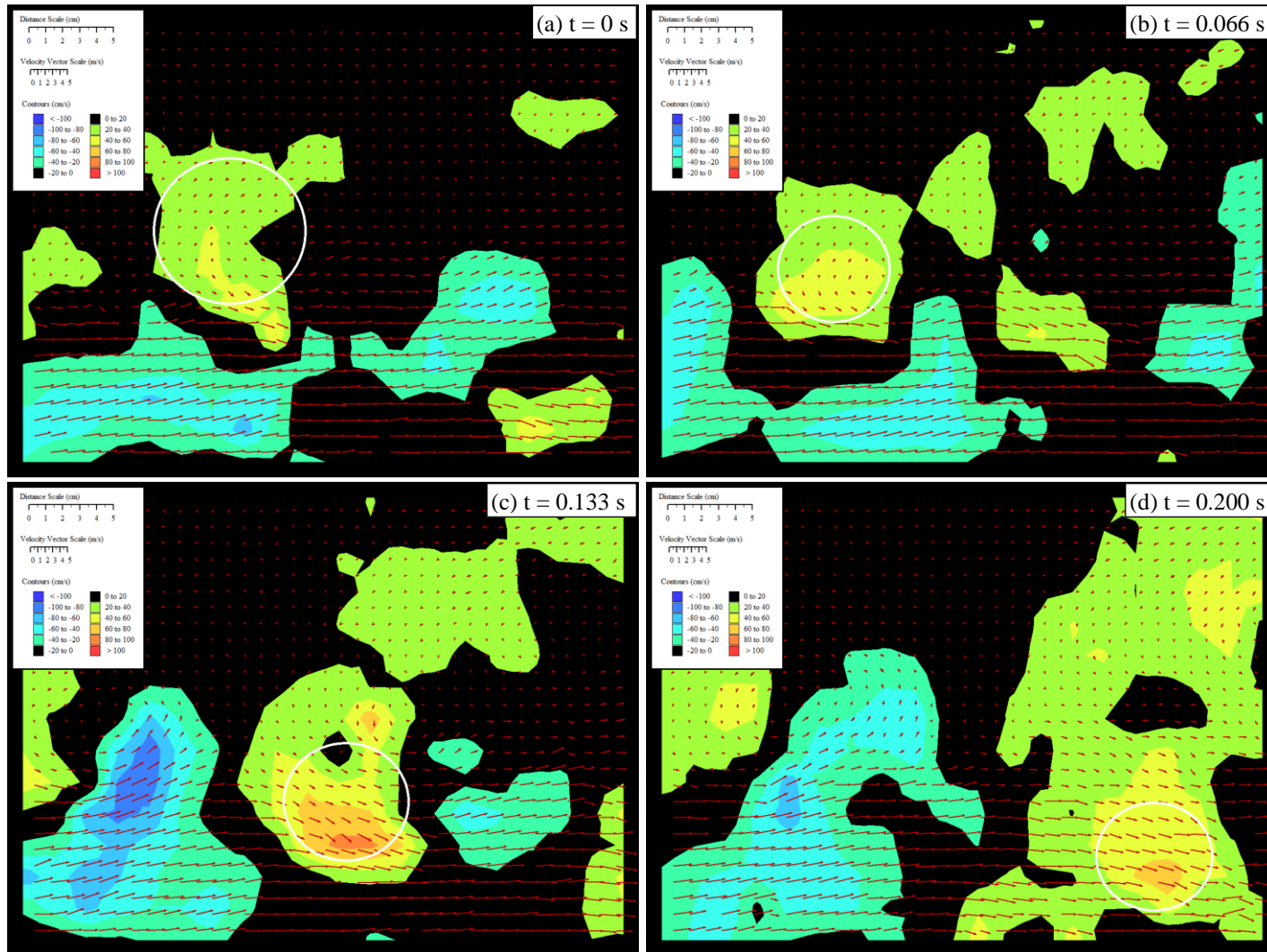


Figure 6-1 Low velocity turbulent flow structure transported from the recirculation zone to the bed for Experiment G05.00

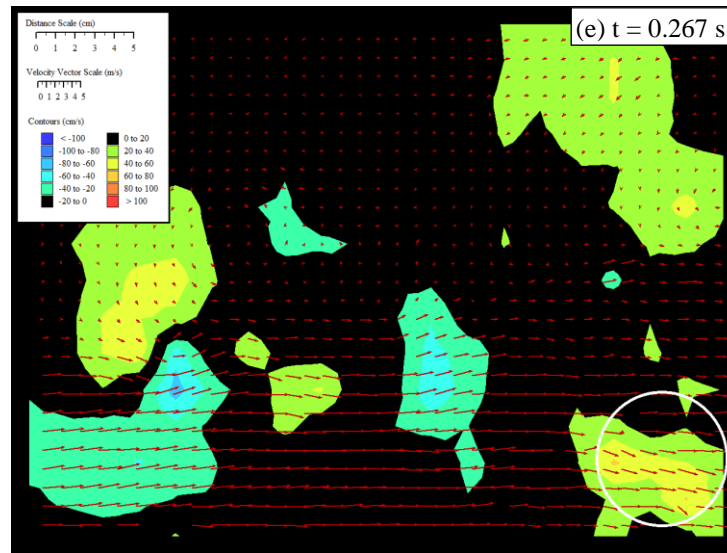


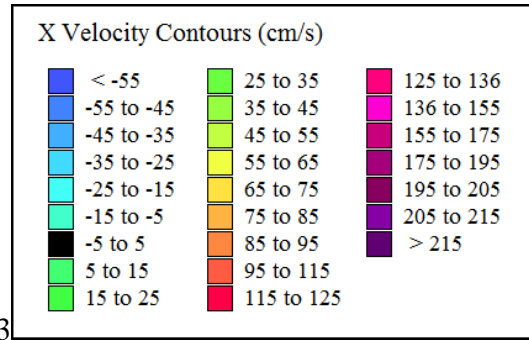
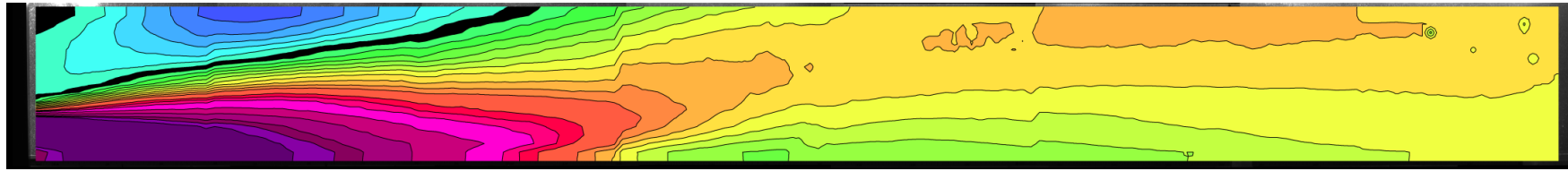
Figure 6-1: (continued)

#### 6.4 PIV Measurements of the Entire Flume

One non-standard PIV experiment was performed in which the velocity distribution in the entire culvert was obtained for one gate setting and one flow rate. The gate setting that was selected was the gate setting that SFWMD found might be the most problematic gate setting, according to a numerical flow analysis. The test setting was for a 4.8 inch high gate opening and a model flow rate of 2.15 ft<sup>3</sup>/s. This is close in comparison to the settings of the standard experiment G05.00, with a 4.875 inch high gate opening and a 2.39 cfs flow rate, in the standard PIV measurements. The experiment conducted for the non-standard PIV measurement corresponds to a prototype gate opening of 3.2 feet.

To do this experiment, PIV was performed the same way that PIV was done for the standard experiments, but instead of just looking at the inlet section, PIV was done on seven longitudinal sections of the culvert, one section at a time. The results of the PIV analysis were then merged to form the entire velocity distribution. This was a complex, time-consuming process, especially filtering and analysis of the resulting PIV images, so the full-culvert PIV study was only done for one test condition.

Figure 6-2 shows the contours of the streamwise velocity vectors for the complete culvert PIV test. The full length of the recirculation zone is shown in the figure. In addition, the behavior of the jet as it expands in the culvert is shown in the image.



3

Figure 6-2 Streamwise velocity contours for the entire model culvert for a gate setting of 4.8 inches and a flow rate of 2.15 cfs

The jet initially impinges on the bed and then is deflected towards the crown of the flume where it is once again deflected back towards the bed. The deflection effect diminishes in strength as the vertical velocity profiles become more uniform. The effect that this "meandering" of the flow stream has on the bed pressure distribution will be discussed in Section 6.5.

## **6.5 Pressure Measurements**

For each sensor, the data from all six data sets were averaged. This was done for each of the eight experiments. The data for the pressure sensors were measured in volts. The voltages were converted to a pressure head based on the sensor calibrations prior to averaging.

Pressure measurements were converted to values that were relative to the same datum so that trends in pressure data could be observed and compared across the range of experiments. Varying gate settings affect the head levels in the forebay from experiment to experiment. This variation in headwater can greatly increase or decrease the total pressure observed at the sensors, but does not affect the pressure trends. For example, if both the headwater and the tailwater go up by one foot, the flow through the culvert essentially stays the same and the mean pressure at each of the sensors in the culvert will go up by one foot, but the pressures measured at each of the sensors remains the same relative to the sensors around it. Essentially, the only effect of increasing the headwater and the tailwater by the same amount is that the magnitude of the pressure datum increases.

Therefore, to calculate the relative pressure, the headwater was subtracted from the pressure readings for each sensor. The relative average, minimum, and maximum pressures recorded at each sensor were calculated. These three pressures at each sensor are graphed for each experiment on a single graph. Trend lines of varying magnitude of polynomial functions were added to help visualize trends in pressures and pressure fluctuations. These trend lines are only a visual aid for understanding the data and do not represent theoretically predicted behavior of the bed pressure. See graphs a) through h) in Figure 6-3 for the relative pressure graphs.

From the upstream-most sensor, the pressure tends to decrease to a minimum at the third sensor – the location approximately nine inches downstream of the gate in the model. At this distance downstream, the pressure has the least deviation from the mean, for all experiments. This is associated with the geometry of the flow, which comes into the culvert through the gate with momentum in the negative y-direction, or towards the flume bed. The downward moving jet impinges on the bed before being reflected in the flow where it expands to fill the entire culvert. This initial downward movement imparts a relatively steady pressure on the bed that is apparent for all of the gate settings. Farther downstream of the gate the downward momentum of the flow from the forebay ceases to affect the bed pressure.

Based on the results shown in Figure 6-3, the lowest average bed pressures are observed to occur 9 to 18 inches downstream of the gate, with low gate settings causing the lowest average bed pressures to occur farther downstream of the gate than for high gate settings. Incidentally, 18 inches in the model corresponds to 12 feet of culvert in the prototype.

For comparison, prototype failure was primarily in the first 4 to 5 precast boxes of the structure, i.e., the first 32 to 40 feet.

Continuing downstream from the sensor with the minimum average pressure, average pressures generally increase, especially for experiments with lower gate settings. This increase in pressure is followed by a slow drop off in pressure for the higher gate settings (see the pressures in Figure 6-3 for G09.00, G10.50, and G12.00). This underscores the "meandering" effect observed in the non-standard PIV analysis done for the 4.8 inch gate setting. The asymmetry that is caused by the low velocity recirculation zone not only causes the jet to reflect off of the bed, but pulls the jet towards the crown farther downstream. The jet then reflects off of the crown and travels back towards the invert. This effect gradually diminishes as the flow travels downstream, returning to a uniform flow distribution. Based on pressure observations, it appears that the "meandering" of the jet is controlled in part by the length of the recirculation zone, which is controlled by the gate setting. Higher gate settings appear to lead to shorter recirculation zones and thus shorter jet deflection wavelengths. However, this observation should be corroborated in the future with additional measurements.

In addition to the increase in average pressure, deviations from the average pressure or fluctuations in pressure, tend to increase with distance downstream of the gate. This is due to the mixing of fluid from the recirculation zone that forms above the jet with the fluid in the jet. The low velocity fluid in the recirculation zone is transferred by vortices from the recirculation zone throughout the jet and ultimately to the flume bed. These flow incursions produce spikes of positive and negative pressure as they are transferred to the flume bed at sensor locations and are carried by the velocity of the jet downstream.



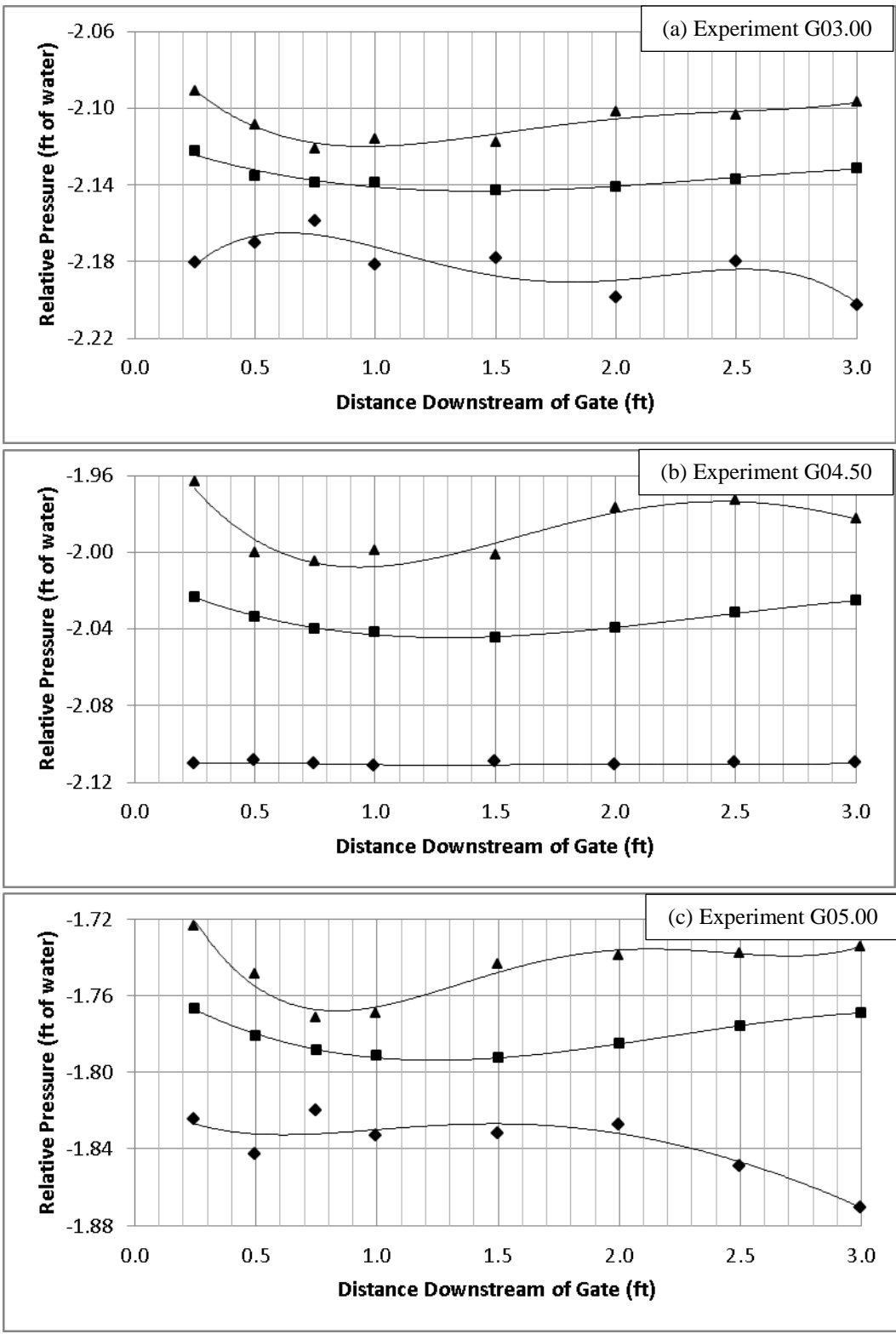
Potentially, the low velocity incursions result in elevated pressures followed by reduced pressures associated with flow acceleration of the jet, but this phenomenon was not experimentally verified. Refer to the graph c) in Figure 6-3 for an example of this trend.

Experiments with gate settings less than six inches, show fluctuations continuing to grow with increasing distance downstream of the gate. This shows that the turbulent vortices continue to be transferred to the bed even farther downstream than just to the portion of the flow examined through PIV measurement. This is likely due to the end of the recirculation zone being farther downstream. Because a high definition of pressure fluctuations was desired on the bed of the culvert near the gate, there were no pressure transducers located more than three feet downstream of the gate. As a consequence, the maximum and minimum instantaneous bed pressures may not have been captured for experiments with the lowest gate settings since these pressures may have occurred more than three feet downstream of the gate.

It should also be noted that the minimum pressures gathered in these experiments likely do not represent the largest potential minimum pressures. Based on observation of the pressure measurement time series, spikes in negative pressure translated to the bed of the flume by flow incursions from the recirculation zone are infrequent and random in occurrence due to the chaotic nature of entrainment from the recirculation zone. While six minutes likely gives a representative measure of the average pressure distribution and the standard deviation of the pressure measured by the transducer, it is probably not a long enough period to record extreme events like minimum and maximum pressures.

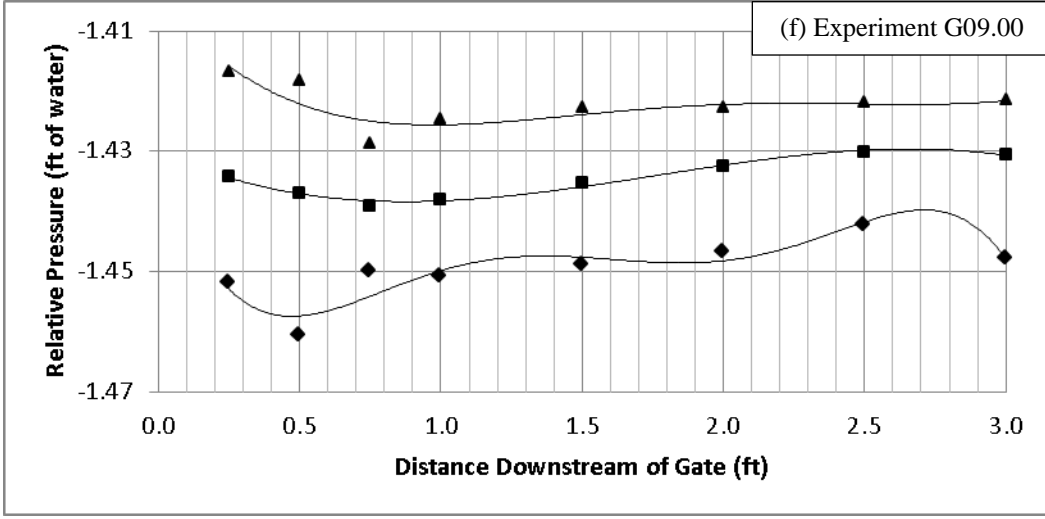
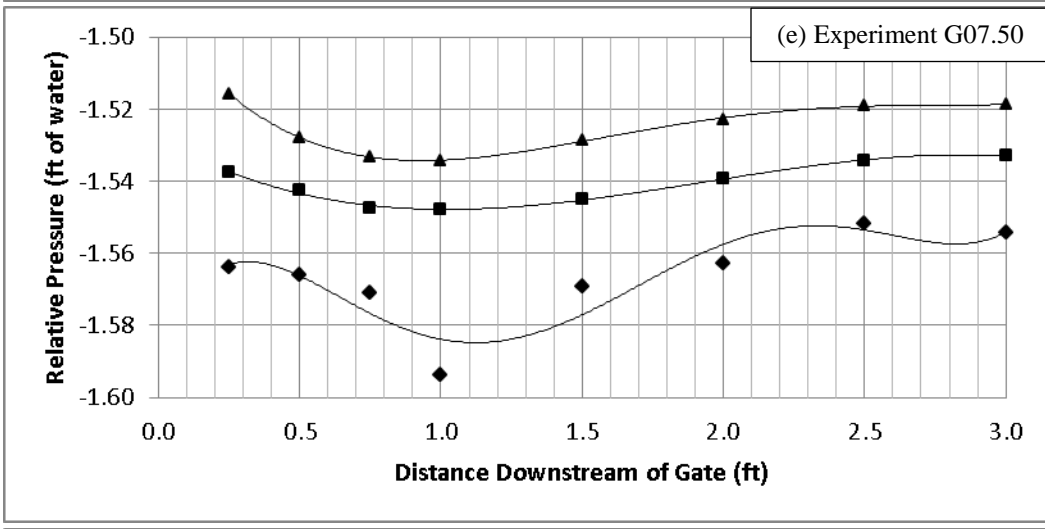
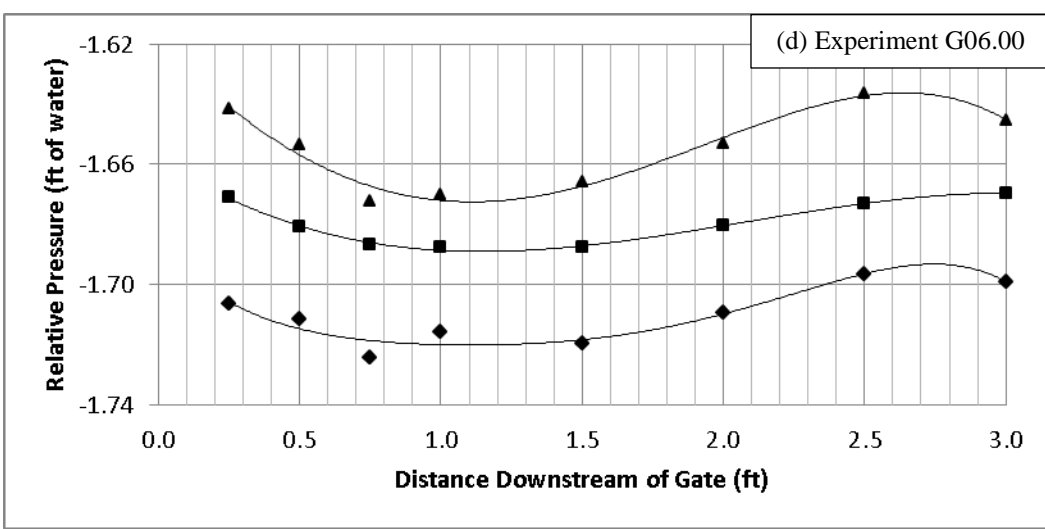
This is made apparent by the scatter in the minimum pressure data in Figure 6-3 for each experiment. The only experiment which does not show scatter in the minimum pressure data is experiment G04.50 where minimum pressures appear stagnant across the distance downstream of the gate. The pressures for this test were lower than for any of the other tests, and it appeared that minimum pressures were below the saturation limit of the sensors. The aforementioned trends however, are apparent in the experiments with a gate setting lower and higher from experiment G04.50. It would be plausible to expect similar trends in this experiment.

Examination of the relative pressures in the flume during experiments with higher gate settings reveals increases in all pressures, minimum, maximum and average, with distance from the gate. Pressure data from experiments with the gate set higher than six inches show this trend. Refer to graphs e) through h) in Figure 6-3. This shows that the recirculation zone is much less defined due to the decrease in velocity of the jet formed downstream of the gate and the elimination of a stagnation region behind the gate. This decrease in the recirculation zone intensity is magnified by the increase in gate height. The decrease in recirculation zone intensity also decreases the deviation or fluctuations in observed pressures. The smaller recirculation zone does not produce high intensity pressure spikes, and the spikes that are formed do not penetrate through the jet to the bed.

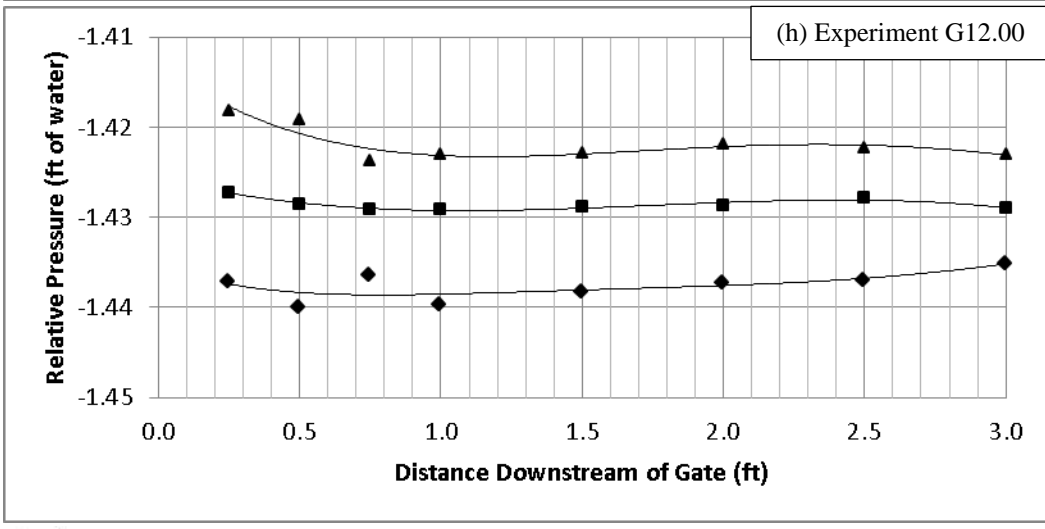
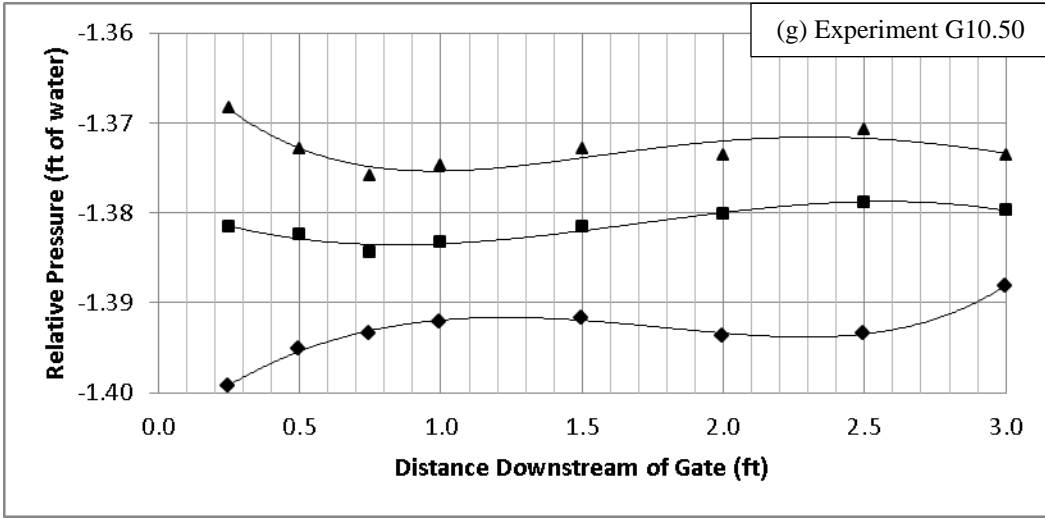


- ◆ Relative Minimum Pressure
- ▲ Relative Maximum Pressure
- Relative Average Pressure

Figure 6-3 Relative Pressure Graphs



◆ Relative Minimum Pressure    **Figure 6-3 Relative Pressure Graphs (cont.)**  
▲ Relative Maximum Pressure  
■ Relative Average Pressure



◆ Relative Minimum Pressure    **Figure 6-3 Relative Pressure Graphs (cont.)**  
▲ Relative Maximum Pressure  
■ Relative Average Pressure

## 6.6 Correlation of Pressures

To examine the temporal relations between pressure sensor measurements along the bed of the flume, the correlations between time series of pressure readings from different sensors were calculated. The correlations between pressure measurements allow the timing associated with the translation of pressure fluctuations to be studied, specifically pressure fluctuations associated with turbulent structures that carry the fluctuations from sensor to sensor. See Figure 6-4 for the correlation graph of one data set from Experiment G05.00. The correlations are between the pressure time series measurements for sensors 1 and 2, sensors 2 and 3, sensors 3 and 4, etc., as shown by the legend, with sensor 1 being the sensor that is farthest upstream.

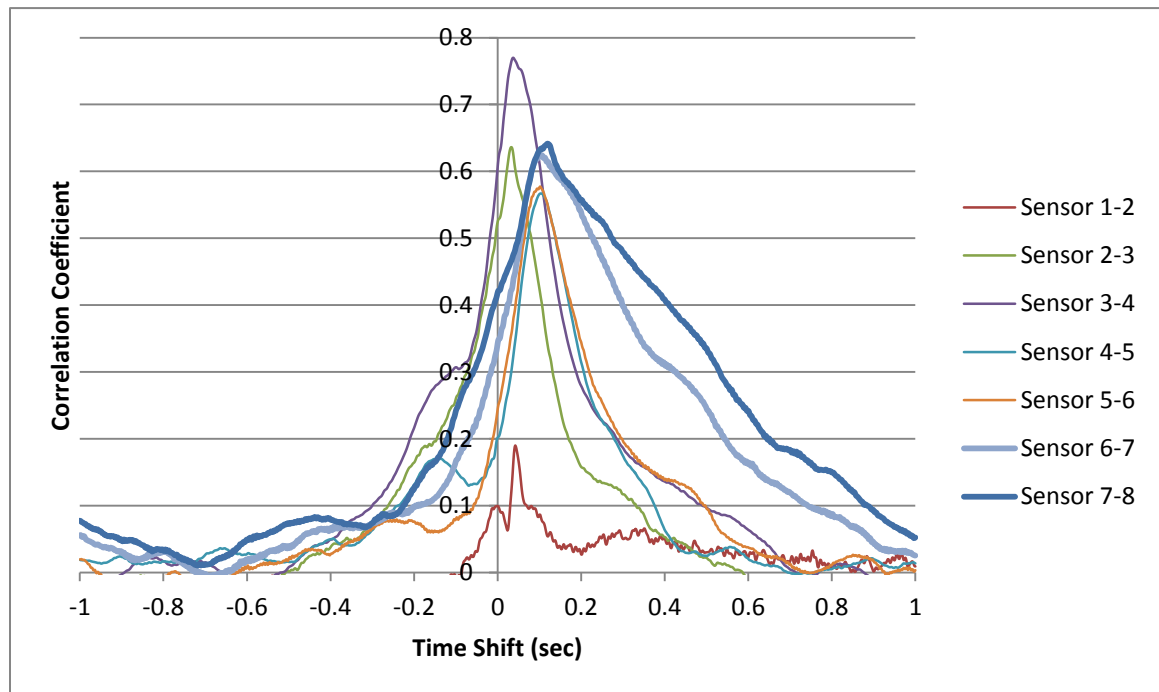


Figure 6-4 Pressure Correlation Graph of Experiment G05.00

The correlation coefficient shows the degree of linear correlation between the two sensors and ranges in value from zero to one, with a value of one representing the strongest correlation. The x-axis shows the time step in seconds.

The peak in correlation coefficient, for a given sensor pair, shows when pressure readings are most correlated for a given time step. For Experiment G05.00, the peak correlation is for a time shift of between approximately 0.05 and 0.10 seconds. The peak time shift is associated with the velocity of the jet and the distance between sensors, so the time shift increases with distance from the gate, because the velocity of the jet decreases with distance from the gate. In addition, the last four sensor pairs (4-5, 5-6, 6-7, and 7-8) show longer time shifts because they are spaced at six inches instead of three inches. The larger spacing between the sensors also leads to a reduction in the magnitude of the peak correlation.

The pressure time series data of sensors 1 and 2 are not as strongly correlated as the other sensor pairs. This is presumed to be because sensor 1 is immediately downstream of the gate, where the recirculation zone has very little effect on pressure fluctuations and the observed pressure fluctuations were primarily related to conditions in the forebay; whereas the pressures at sensor 2 may be more strongly affected by the gate and the recirculation zone behind the gate. Sensors located farther downstream are more strongly affected by conditions in the recirculation zone.

The correlation reveals the time it takes for a flow structure, such as a flow incursion that causes a negative or positive spike in pressure, to move downstream to the next sensor.

This timing identification allows the calculation of the velocity at which the flow

structure, that is causing the spike in pressure, is traveling downstream. The sensors that are farther downstream appear to have broader correlation functions, partly because of wider spacing between sensors, but also suggesting that the transit time of turbulent pressure fluctuations is more widely varied than it is near upstream sensors. Despite being turbulent, the jet that comes through the gate has a relatively steady velocity and constant momentum. As the flow jet travels downstream, it becomes more turbulent with intermixed high and low momentum flow, the high momentum flow being from the jet and the low momentum flow being from the recirculation zone. This tends to broaden the correlation function and lower the peak correlation to some extent.

## **6.7 Velocity and Pressure Relationship**

Experiment G05.00 was evaluated both for pressure correlations (Section 6.6) and visible flow incursions (Section 6.3). The times of the PIV measurements showing the flow incursion of Section 6.3 were synchronized with bed pressure readings, and the corresponding time steps of the flow incursion were plotted with the pressure time series data. Figure 6-5 shows the pressure readings associated with the flow incursion depicted in Figure 6-1 and described in Section 6.3. The vertical lines in Figure 6-5 indicate the times when the PIV images showing the flow incursion were collected.



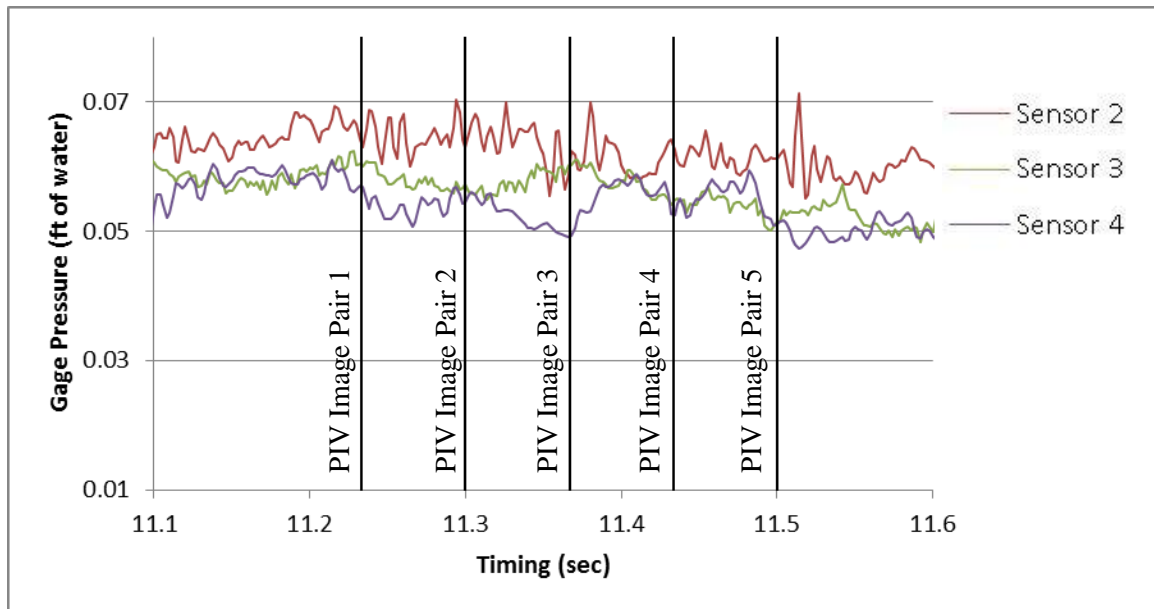


**Figure 6-5 Pressure Readings from Experiment G05.00 Associated with Visible Flow Incursion**

This flow structure was visible with PIV field measurements but there was no visible pressure spike in the data at these time steps in the pressure data. The reason for this is likely because although the pressure series and the PIV series were synchronized in time, the PIV images were recorded along a different alignment than the pressure sensors. Thus, turbulent structures that were obvious in the PIV images were not all significant contributors to the pressures measured on the bed at the locations of the pressure sensors.

Further examining the pressure data showed that pressure spikes caused from flow incursions are apparent at other times in the pressure data of Experiment G05.00. See Figure 6-6 below for an example of a spike in pressure from Experiment G05.00. The spike shown in Figure 6-6 is an extreme event. Unfortunately, because of memory limitations, there is no PIV data available for this event (PIV data could only be recorded for the first 12 seconds of each test); it would have been favorable to observe how an event of this magnitude appeared in the PIV data.

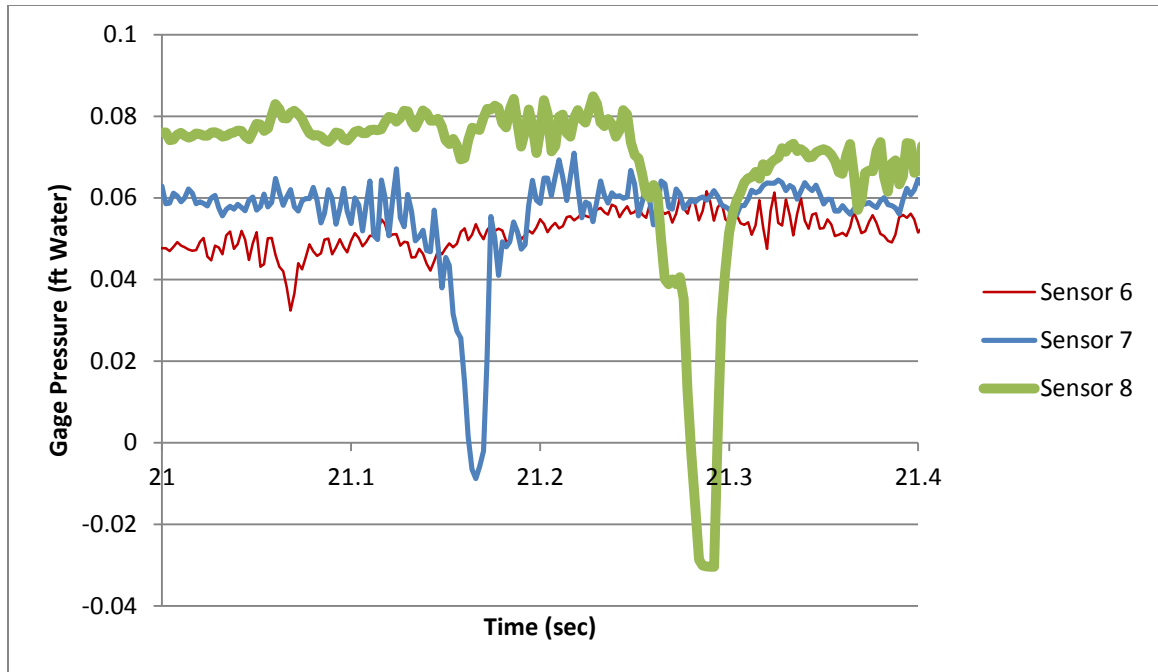


**Figure 6-6 Experiment G05.00 Pressure Spike**

The pressure data shown in Figure 6-6 depicts the spike in pressure at the three most downstream sensors. The spike is visible in the upstream sensor, sensor 6, at approximately 21.07 seconds and can be seen propagating downstream and also increasing in magnitude from sensor 7 to sensor 8 at 21.17 and 21.28 seconds respectively. It is important to remember the flow path of the incursion shown in Section 6.3, and to recognize that as these structures translate in the direction of flow, they also move towards the bed, having a greater impact at downstream locations. The flow incursion was transferred from the recirculation zone to the bed of the flume as it traveled downstream. As flow incursions form and move downstream, getting closer to the bed, the pressure spikes associated with them propagate from sensor to sensor, and potentially increase in magnitude.

The translation of this pressure spike with regard to timing is also important. As previously discussed, the peak correlation of the pressure time series for the downstream sensor pairs of test G05.00 is at a time shift of approximately 0.1 seconds. The pressure spike shown in Figure 6-6 propagates downstream from one sensor to the other in approximately 0.1 seconds. Examining this time shift with the known distance between sensors we can estimate the velocity of the flow incursion causing the pressure spike. Upon examination, this velocity is about 1.5 m/s (4.9 ft/s), which is comparable to the velocity of the jet in the experiment. This shows that flow incursions, and thus the pressure spikes, are carried by the inherent flow velocity near the flume bed.

In examining the pressure data for Experiment G05.00 there are other visible trends in pressure fluctuations. Some of these trends are observed over a larger time scale than the pressure spikes caused by the flow incursions. Figure 6-7 shows a negative pressure trend followed by a rise in pressure that occurs over a longer time scale in Experiment G05.00. The pressure trend indicates longer term changes in the behavior of the recirculation zone. Careful observations of the trends in Figure 6-7 reveal that the pressure time series of adjacent sensors are still correlated by about 0.1 second.

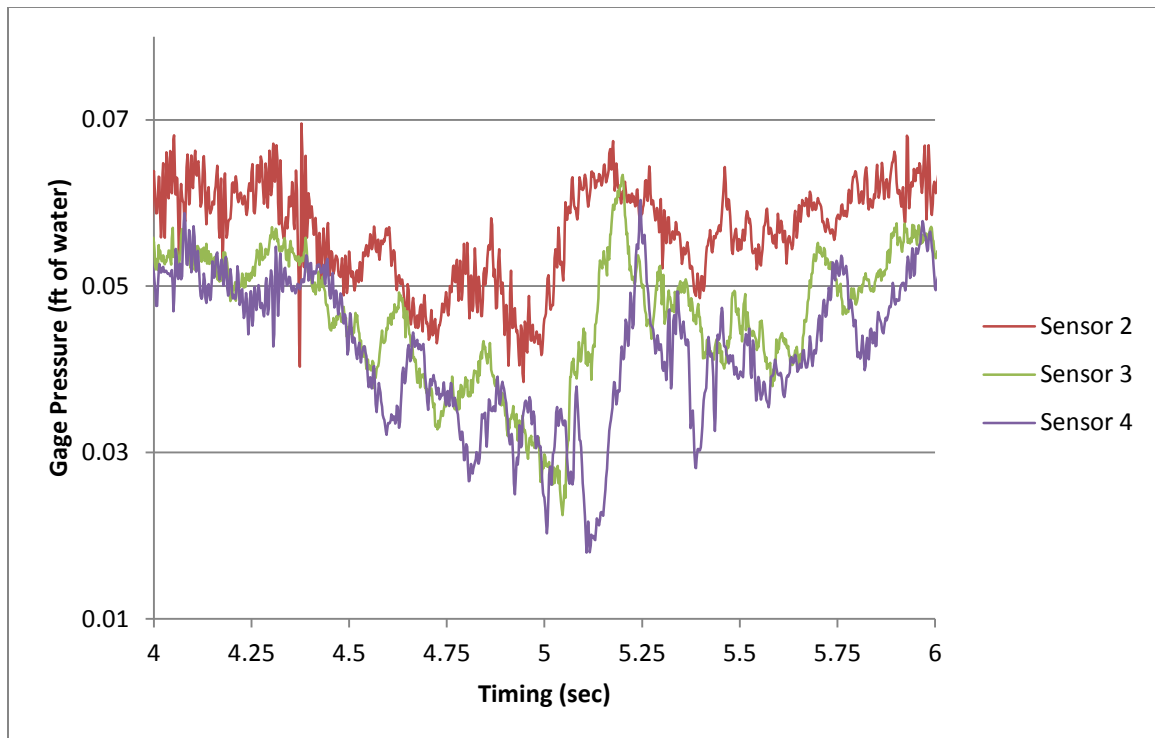


**Figure 6-7 Long-term Pressure Trends in Experiment G05.00**

An observed trend in decreasing pressure begins at approximately 4.3 seconds and ends at approximately 5 seconds. A more rapid rise in the pressure follows between approximately 5.0 seconds and 5.25 seconds. The longer term change in pressure indicates that the trend is not associated with a flow incursion, transferred by the flow, but by changes in the large eddy in the recirculation zone formed above the jet.

## Chapter 7 Conclusions

### 7.1 Overview

In this thesis, PIV velocity and pressure measurements were gathered in a 1:8 scale model of the SFWMD S375 gated box culvert control structure. Data were collected and studied from experiments in the model to better understand the pressure and flow characteristics of the prototype culvert. This project was initiated in part because of the partial failure of the SFWMD S375 structure.

The goal of this project was to collect information with regard to culvert settings and conditions to help understand flow and pressure relations within the culvert.

Understanding these conditions and relations is advantageous in an effort to avoid flow characteristics that are presumably adverse to structure integrity.

### 7.2 Observations

Several conclusions can be made from experimental results, including the PIV velocity and pressure measurements made within the model culvert. PIV measurements allowed for the calculation of locally averaged velocities of each experiment. Average velocity calculations provided a visual representation of flow fields. Average velocity contour maps provided a good understanding of the jet and recirculation zone size and strength from experiment to experiment. A pronounced, high velocity flow jet was observed in experiments with low gate settings. This jet produced a well-defined recirculation zone above the jet stream. Conversely, for experiments with high gate settings, weaker jets

were observed, and thus less defined recirculation zones developed behind the gate. Velocity measurements from the non-standard PIV experiment provided beneficial information as well. The jet was observed deflecting off the flume bed towards the crown, because of the initial momentum towards the bed, and then back towards the crown from the bed, causing a “meandering” effect. This “meandering” diminishes with distance downstream of the gate where vertical velocity distributions became more uniform.

Additionally, flow incursions were observed in the PIV measurements. The measurements showed the translation of low velocity flow incursions from the recirculation zone to the flume bed, where they would impose a spike in pressure observed in the pressure readings.

Relative average, minimum, and maximum pressures were calculated for each experiment from the pressure measurements. Pressure trends were observed in the experiments. For all experiments, pressures decreased from the most upstream sensor to approximately 6 to 12 inches downstream. At this location the pressure had the least difference in maximum and minimum pressures or was the steadiest. This is presumed to be caused by the momentum of the flow from the forebay towards the flume bed. Based on this, it would be unlikely to see large pressure fluctuations at this location in the prototype and thus a lower probability of joint failure due to fluctuations. Nevertheless, the low pressures associated with the steady part of the high velocity jet flow in this region might still initiate joint failure in the prototype. These observations should be corroborated with future experimentation.

From this location all pressures tended to increase downstream of the gate for all experiments. For experiments with lower gate settings, the fluctuation or difference between maximum and minimum observed pressures increased with distance downstream. It should be further noted that the absolute minimum and maximum pressures may not be captured for experiments with low gate settings. This is because these pressure instances may have occurred downstream of the farthest downstream transducer. Experiments with high gate settings showed an increase in all pressures from the location of minimum average pressure. The fluctuation, or difference in maximum and minimum pressures, did not increase downstream as it did with experiments of low gate settings.

Correlation observations between pressure sensor readings and timing, paints a broad picture of flow behavior observed in the model. Correlating the time of these pressures across the sensors allows for the estimation of the translation velocities of low velocity incursions. Observations showed that they are traveling along the bed at a velocity comparable to the jet velocity. It was also observed that some trends in pressure occur over time periods that are much longer than the travel times between sensors that are associated with the jet velocity.

Separate instances of flow incursions in the velocity measurements and pressure spikes in the pressure measurements were found. However, due to limitations in data measurement components, it is very difficult to capture an instance that clearly shows both velocity and pressure effects from the same flow incursion.

These observations and resultant data indicate experiments with low gate settings, below six inches in the model, were more likely to produce the adverse effects presumed to cause partial failure in the prototype. Experiments with low gate settings produced a high velocity flow jet which caused strong low pressure zones on the flume bed, immediately downstream of the gate. The strong flow jet generated a more pronounced recirculation zone above the jet. The recirculation zone was where flow incursions were observed to form, and as they were translated to the bed, they caused large spikes in pressure. These large pressure spikes and strong low pressure zones observed in these experiments in the model were the types of conditions that have been presumed to lead to and or exacerbate partial failure of the prototype structures. Future experimentation should be undertaken in the model or prototype to validate these presumptions and extend results.

It is important to note that the results and conclusions from these experiments, in order to be scaled to the prototype structure, need to maintain Reynolds similarity. This includes timing and velocity components of the results. Refer to Section 3.2 for details.

### **7.3 Future Work and Other Considerations**

The results of this thesis show that there are several possible changes that can be made to the experimentation conducted to improve on the ability to distinguish trends and relationships between velocity and pressure in the model.

Future work is planned to use a PIV camera placed on a sliding system that will allow the entire length of the flume to be exposed to PIV during each test run. This will allow the visualization and calculation of the flow field throughout the entire flume during each experiment performed. One example of this was presented in the thesis. Additional



experimentation settings of PIV measurements throughout the entire flume would be beneficial in understanding the characteristics of velocity and flow within the structure.

Future experiments with increased flow rates would benefit results as well. Current limitations in providing sufficient flow have inhibited the range of conditions that are able to be tested. Increased flow rates in the model may prove beneficial in finding prototype scenarios where pressure fluctuations are highest. Finding these scenarios where fluctuations in the prototype are detrimental to the integrity of the control structure are paramount.

Installing equipment that would allow the laser sheet to be spread across the flume, centered along pressure transducers would be extremely beneficial. This would allow for a more probable likelihood of capturing data from a flow incursion in both velocity measurements as well as pressure. This would allow one to make a clear observation of pressure effects based on location and magnitude of the incursion in the flow field.

Utilizing the presented changes in experimentation would allow for more complete data of the flume model characteristics and the ability to make more accurate comparisons between the model and prototype.

## Bibliography

- Abdul Khader M.H. and Elango K. 1974. Turbulent pressure field beneath a hydraulic jump. *Journal of Hydraulic Research*. 12(4): 469-489.
- Akilli, H., Sahin, B., Tumen, N.F. (2005). Suppression of vortex shedding of circular cylinder in shallow water by a splitter plate. *Flow Measure. Instrument*. 16, 211–219.
- Akoz, M., Kirkgoz, M., and Oner, A. (2009). “Experimental and numerical modeling of a sluice gate flow.” *Journal of Hydraulic Research*. 47(2), 167–176.
- Bowers C.E. Toso J.W. (1987). Karnafuli project- model studies of spillway damage. *Journal of Hydraulic Engineering*. ASCE, 114 (5).
- Bowers, C. E., Tsai, F. Y., and Kuha, R. M. (1964). “Hydraulic studies of the spillway of the Karnafuli hydroelectric project, East Pakistan.” Project Report No. 73, St. Anthony Falls Hydraulic Lab. Univ. of Minnesota, Minneapolis, Minn., 1–380.
- Cassan L, Belaud G. (2012). Experimental and Numerical Investigation of Flow under Sluice Gates. *J. Hydraulic Engineering* 138. 367-374.
- Dey, S., and Sarkar, A. (2008). “Characteristics of turbulent flow in submerged jumps on rough beds.” *J. Eng. Mech.*, 134(1), 49–59.
- Farhoudi, J. and Narayanan, F. (1991). “Force on Slab beneath Hydraulic Jump.” *J. Hydraul. Eng.* Volume 117 issue 1. 64-83.
- Gonzalez, J., SFWMD (2010). Personal communication and submittals.
- Govinda Rao, N. S., and Rajaratnam, N. (1963). “The submerged hydraulic jump.” *J. Hydraulic. Div.*, 89(HY1), 139–162.
- Habibzadeh A. and Wu S., Ade F., Rajaratnam N., Loewen M. R. (2011). Exploratory Study of Submerged Hydraulic Jumps with Blocks. *Journal of Hydraulic Engineering*. Volume 137. 706-710.
- J Westerweel. (1997). Laboratory for Aero & Hydrodynamics, Delft University of Technology, Rotterdamseweg 145, 2628 AL Delft, the Netherlands.
- J. J. Sharp. (1981). "Hydraulic Modeling", pp. 18-21, 44-56, Butterworths, London.
- Kim, D. (2007). “Numerical analysis of free flow past a sluice gate.” *KSCE J. Civ. Eng.*, 11(2), 127–132.
- Kompenhans J, Reichmuth J (1986) Particle imaging velocimetry in a low turbulent wind tunnel and other flow facilities. In: Proceedings of the IEEE Montech '86 conference, Montreal, Canada, October 1986. AGARD conference proceedings no. 399, paper 35.

- Leutheusser, H. J., and Fan, J. J. (2001). "Backward flow velocities of submerged hydraulic jumps." *Journal of Hydraulic Engineering*. 127(6), 514–517
- Pirooz B. Kavianpour M.R. (2000). *Experimental Investigation of Pressure Fluctuations Beneath Hydraulic Jumps*. 29th IAHR Congress. Beijing, China.
- Rajaratnam, N. (1965). "Submerged hydraulic jump." *J. Hydraulic. Div.*, 91 (HY4), 71–96.
- Rajaratnam, N. (1967). "Hydraulic jumps." *Advances in hydrosience*, Vol. 4, Academic Press, New York, 197–280.
- Rajaratnam, N. and Subramanya, K. (1967b) "Flow immediately below submerged sluice gate," *Journal of the Hydraulics Division, ASCE*, 93(4), 57-77.
- Rajaratnam, N., and Subramanya, K. (1967a) "Flow equation for the sluice gate," *Journal of Irrigation and Drainage Division, ASCE*, 93(3), 167-186.
- Roberson, J. Cassidy, J., and Chaudhry, H. (1988), Hydraulic Engineering, Houghton Mifflin Co, Boston.
- Roth, A.. and Hager, W.H. (1999) "Underflow of standard sluice gate," *Experiments in Fluids*, 27, 339-350.
- Rouse, H. (1961) *Fluid Mechanics for Hydraulic Engineers*, Dover Publications, Inc., New York.
- Tavoularis, Stavros. (2005). *Measurement in fluid mechanics*. Cambridge New York: Cambridge University Press. 188-200.
- VassiLiev O.F. and Bukreyev V.I.(1967), *Statistical characteristic of pressure fluctuations in the region of hydraulic jump*, Proc. XII IAHR Congress, Fort Collins, Co.(USA), Vol.2
- Zare, H. K., Baddour, R. E. (2007). *Canadian Journal of Civil Engineering*. Vol. 34 Issue 9, 1140-1148

# Appendices

## Appendix A Average Velocity Contour Maps

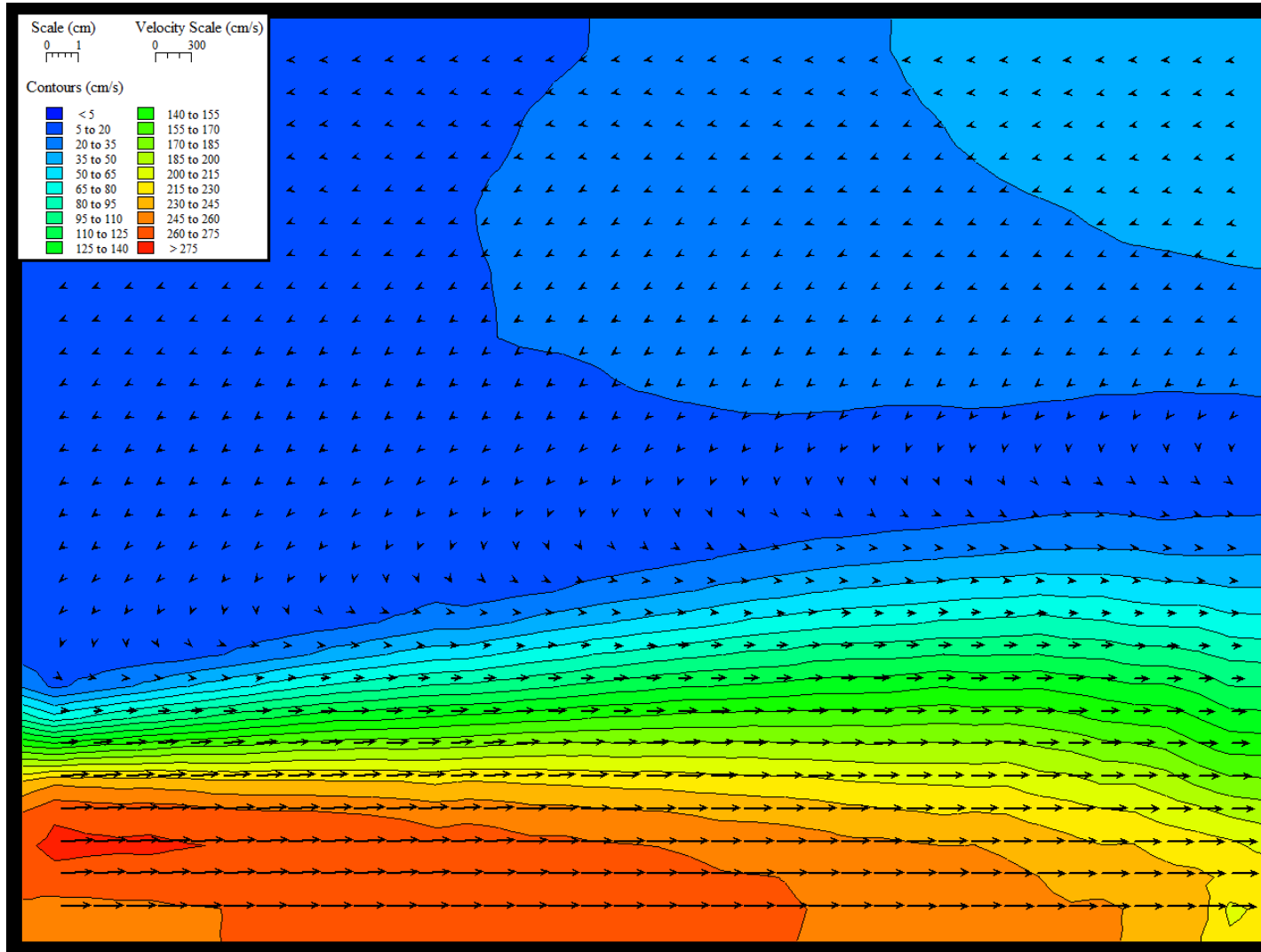


Figure A-1a G03.00 Velocity Contour Map (Small Vector Scale)

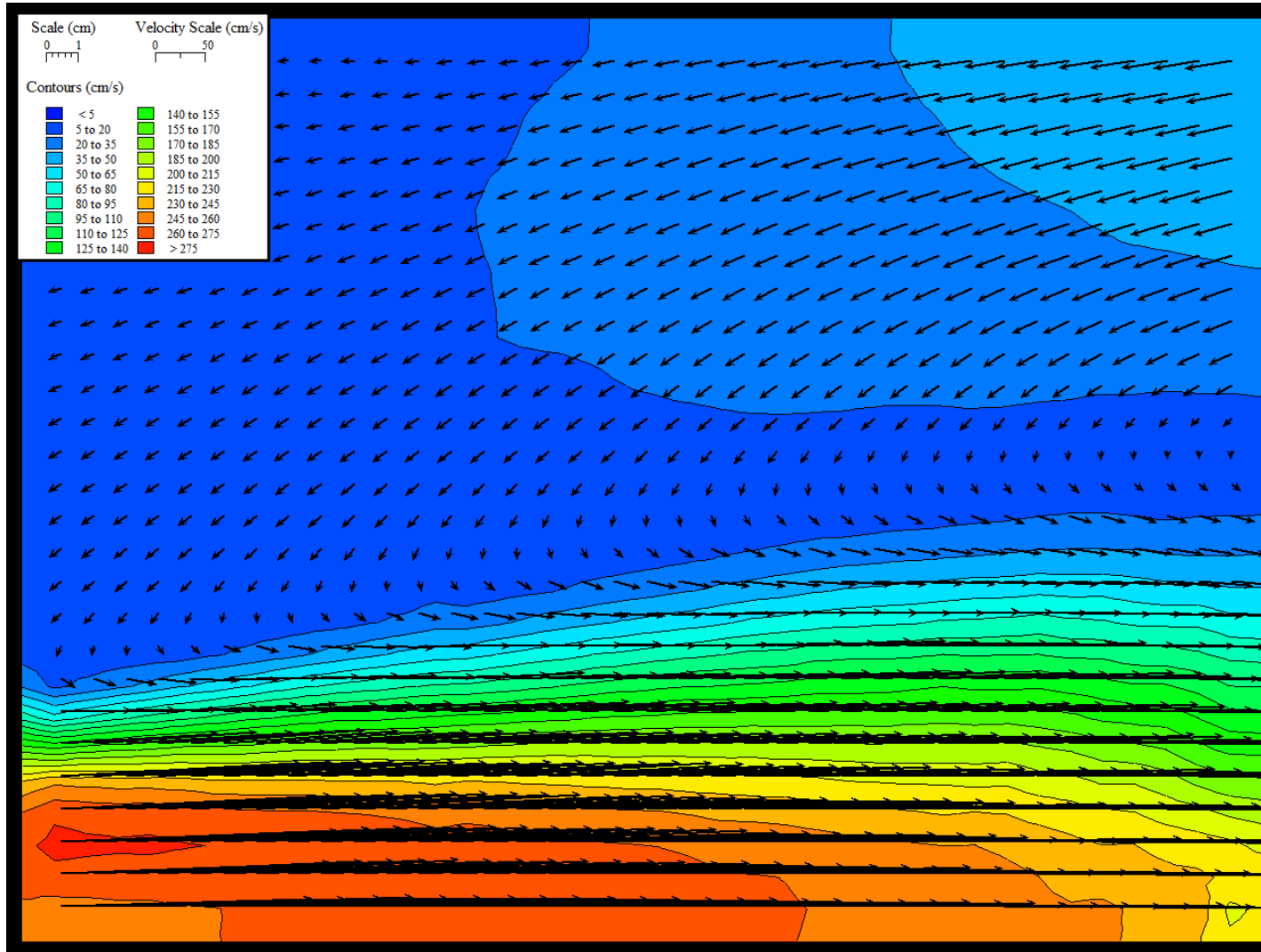


Figure A-1b G03.00 Velocity Contour Map (Large Vector Scale)

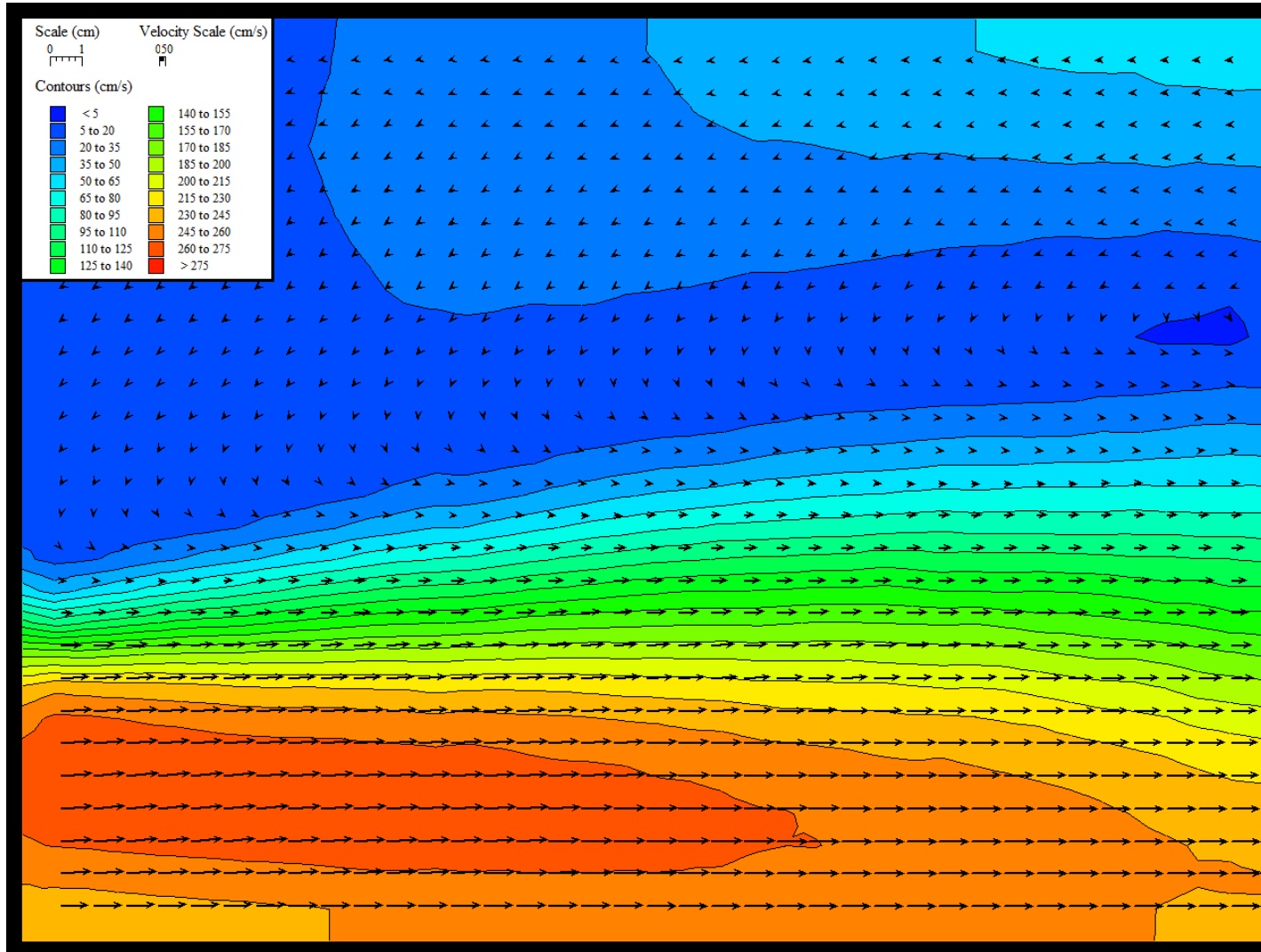


Figure A-2a G04.50 Velocity Contour Map (Small Vector Scale)



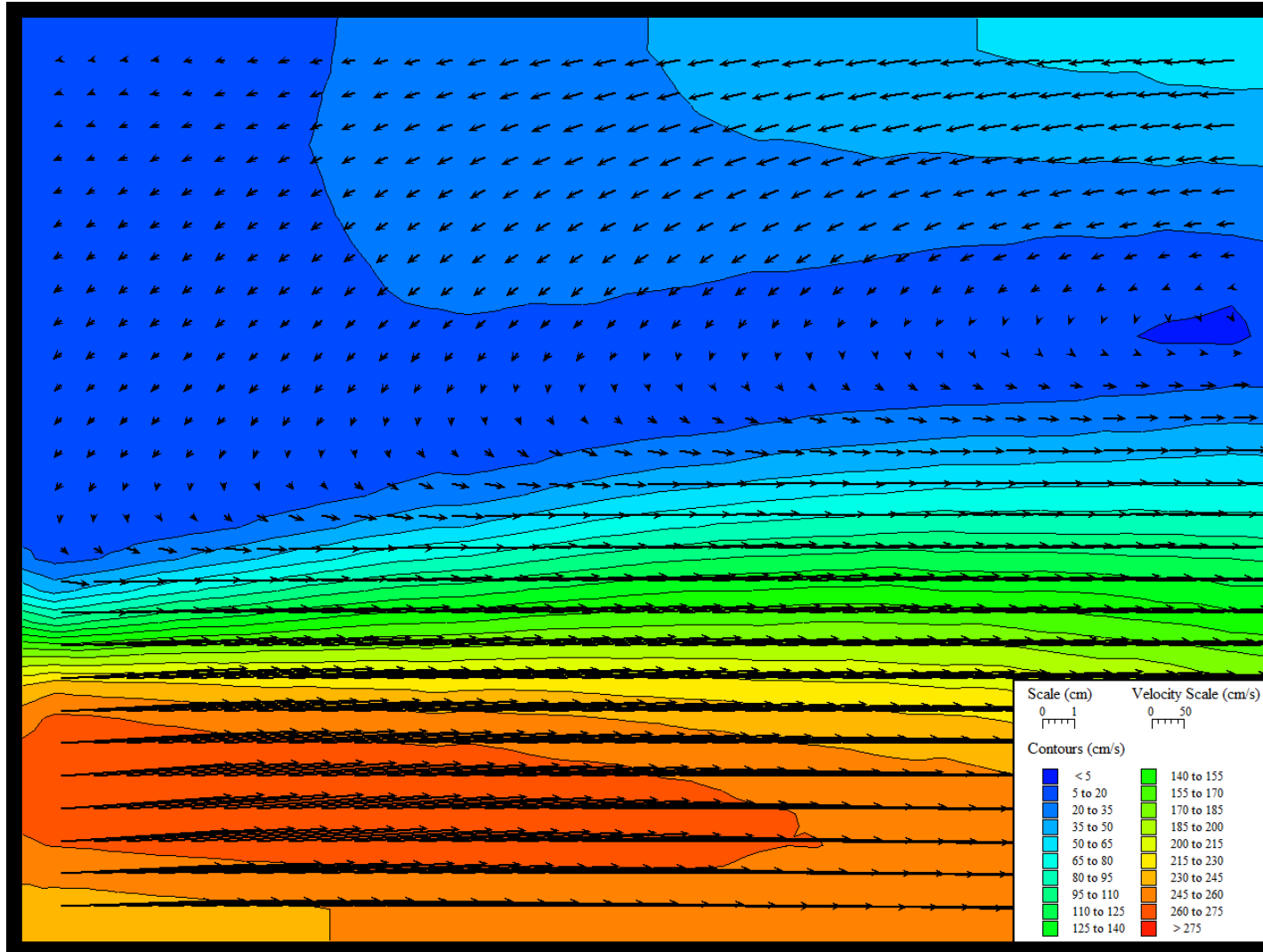


Figure A-2b G04.50 Velocity Contour Map (Large Vector Scale)

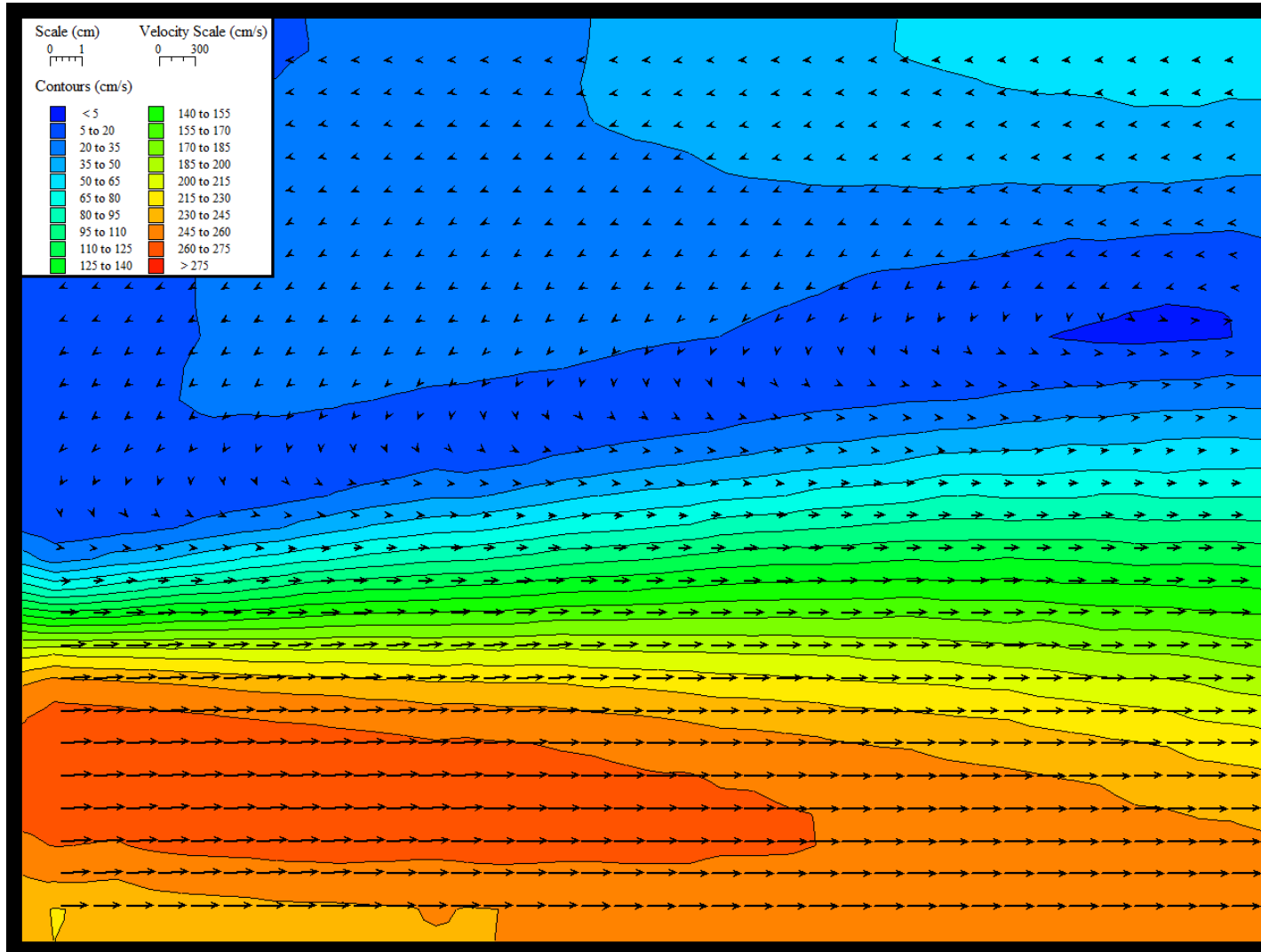


Figure A-3a G05.00 Velocity Contour Map (Small Vector Scale)

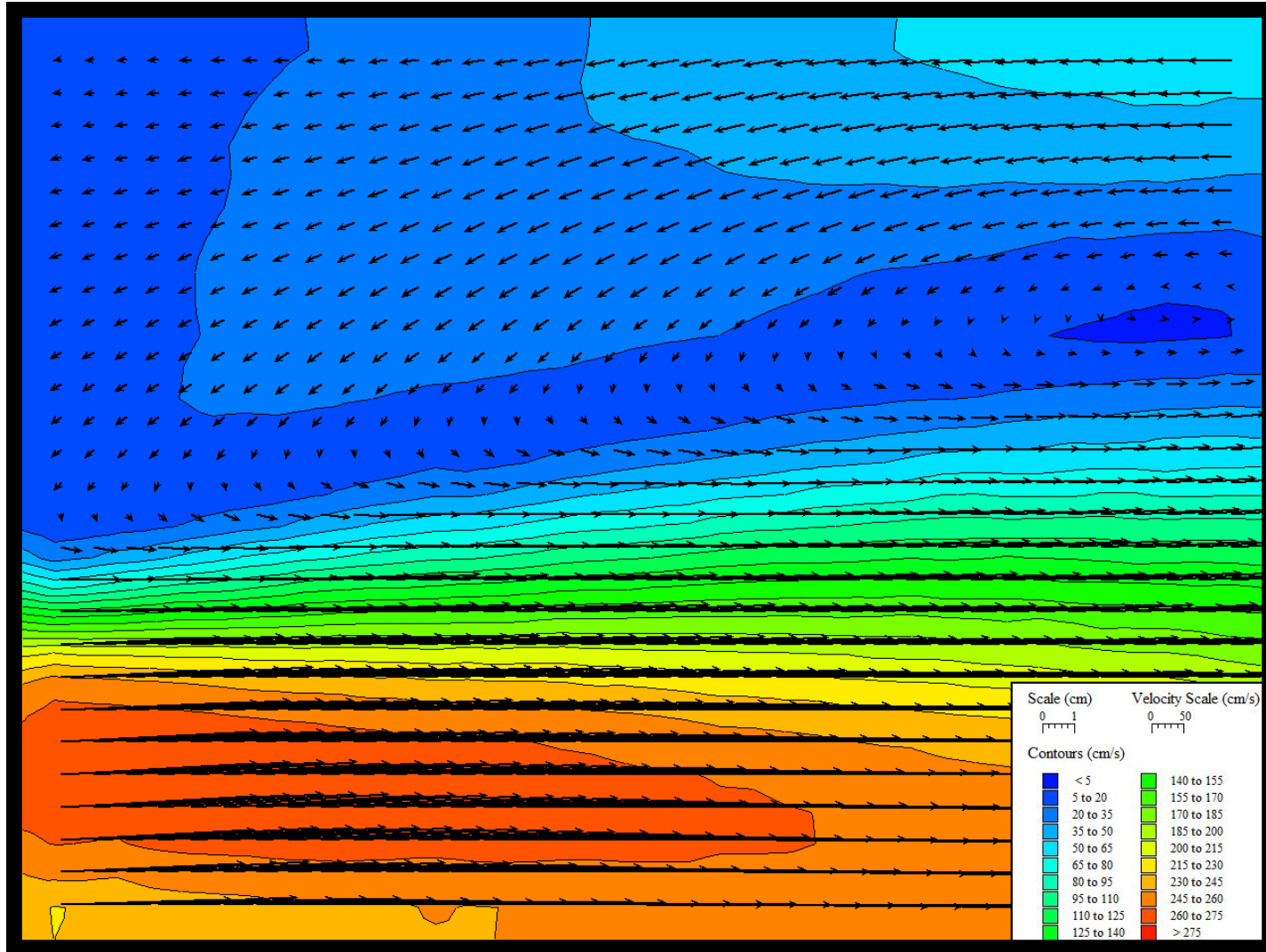


Figure A-3b G05.00 Velocity Contour Map (Large Vector Scale)

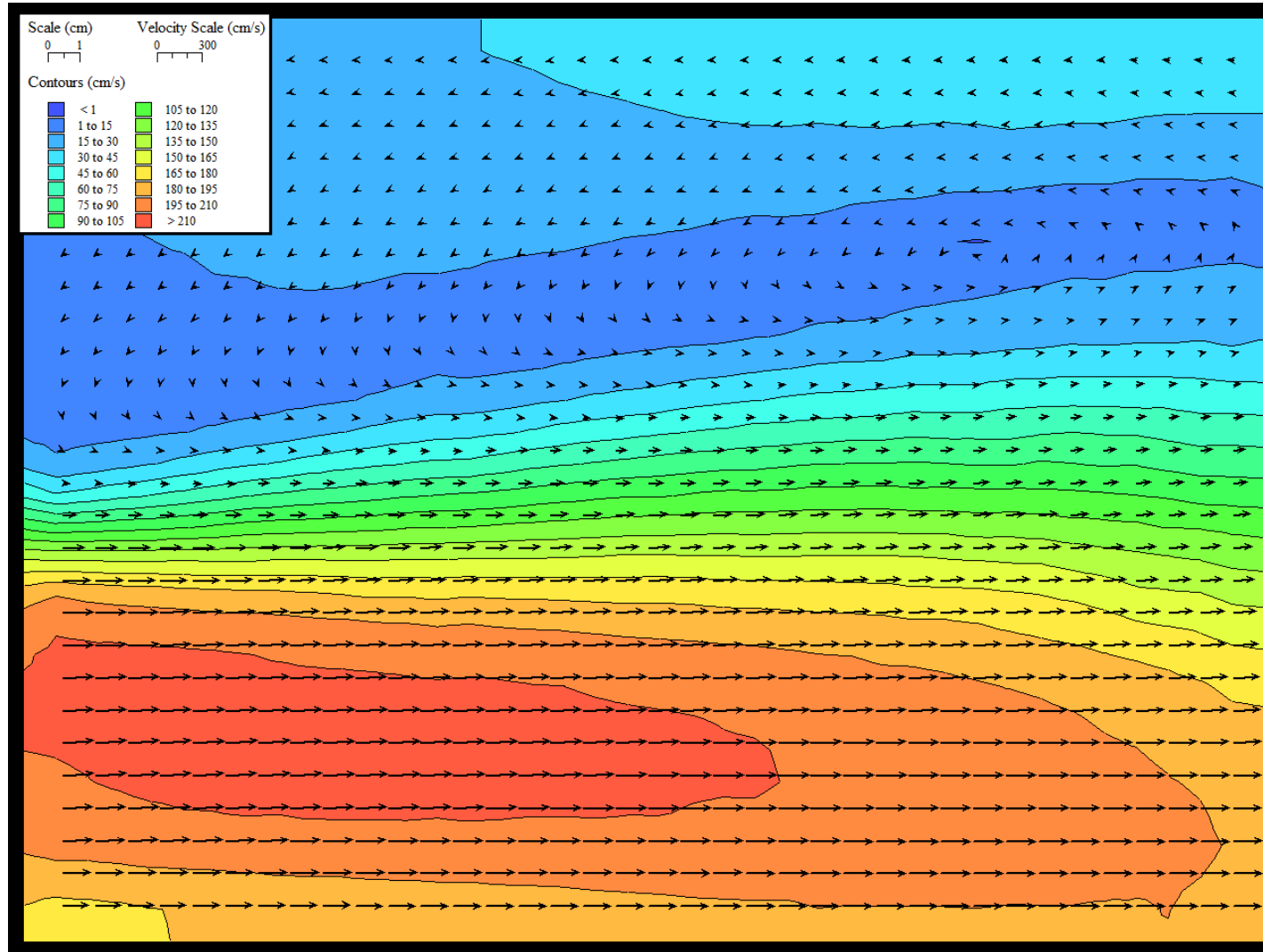


Figure A-4a G06.00 Velocity Contour Map (Small Vector Scale)

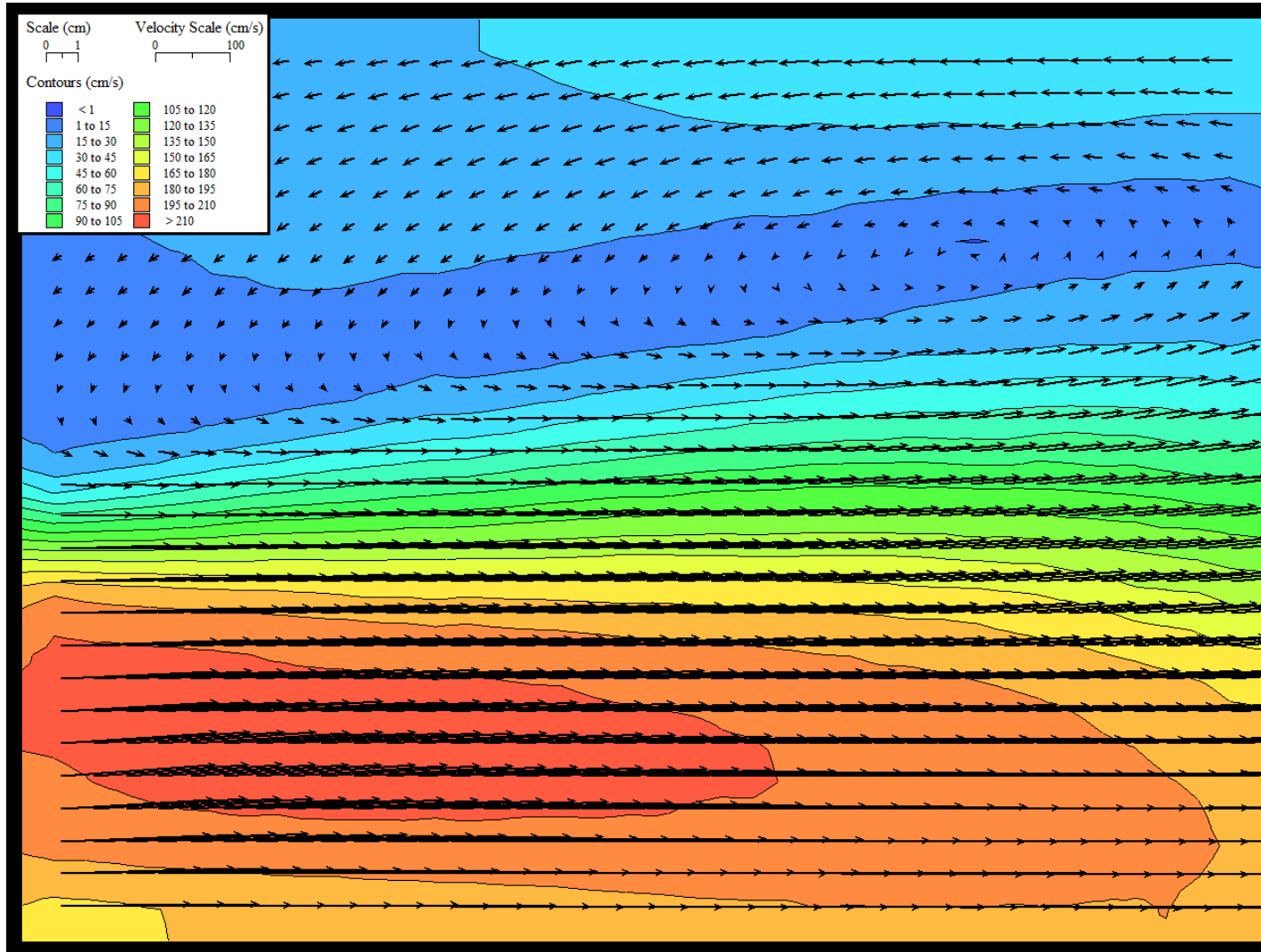


Figure A-4b G06.00 Velocity Contour Map (Large Vector Scale)

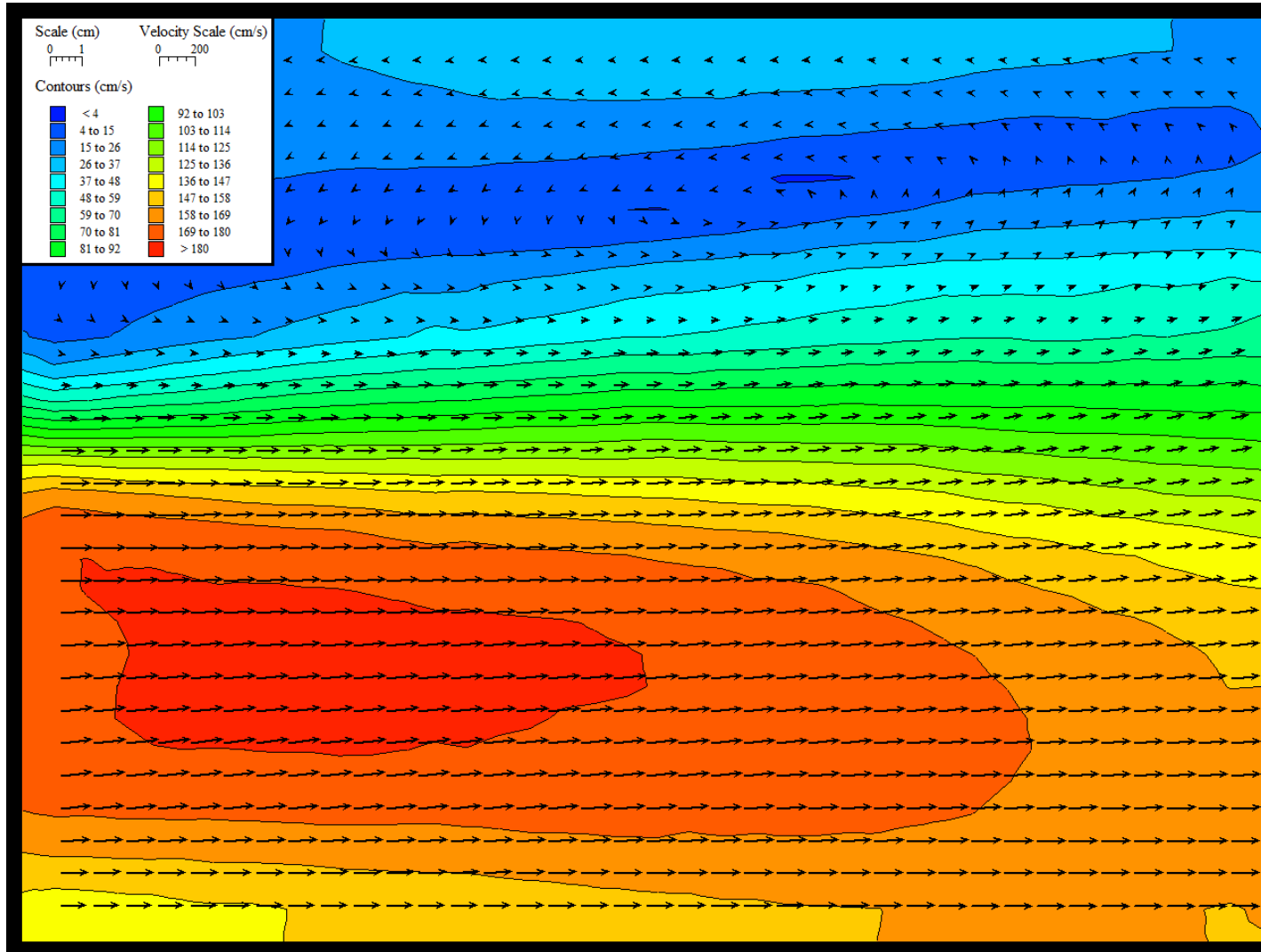


Figure A-5a G07.50 Velocity Contour Map (Small Vector Scale)

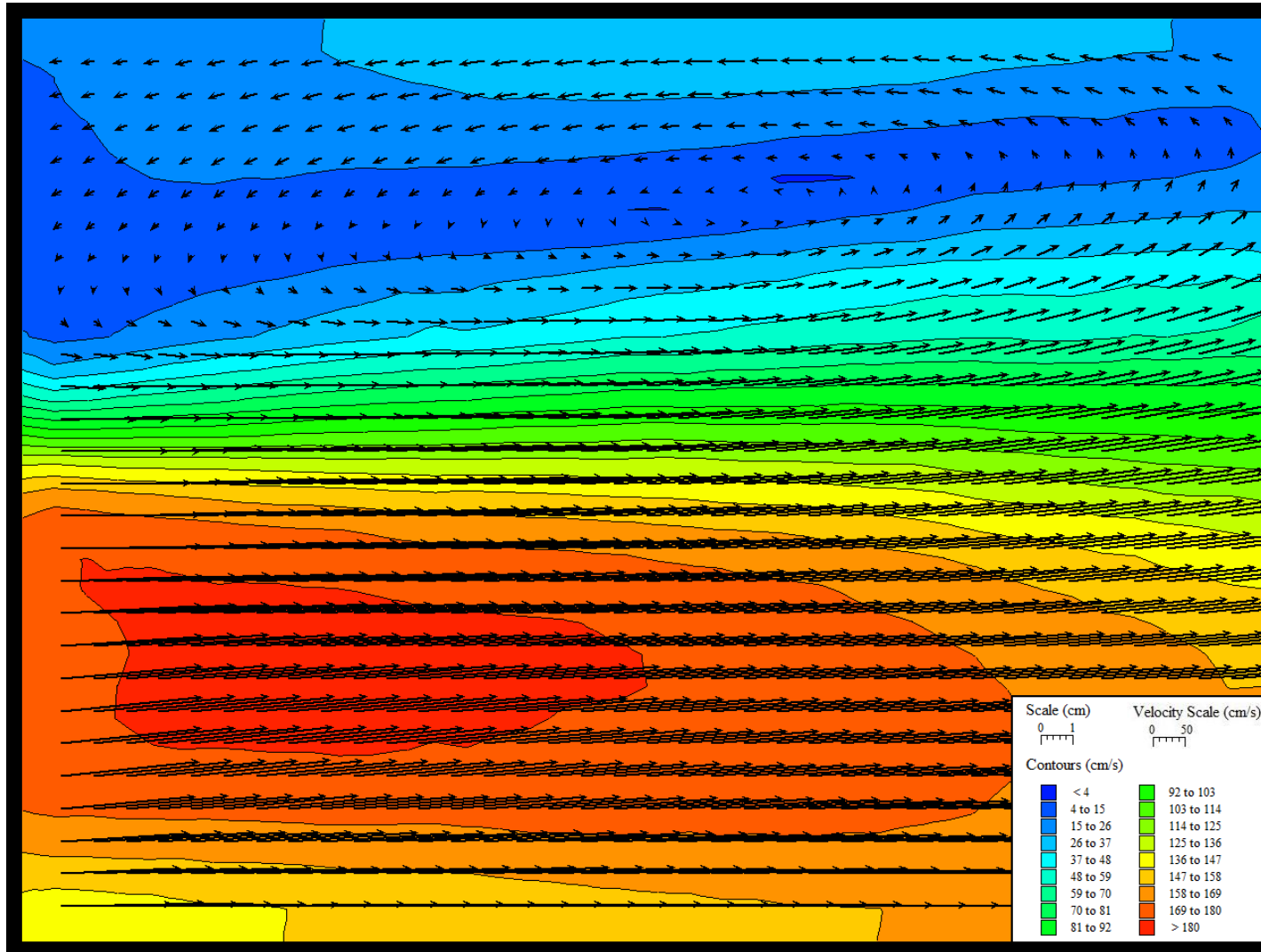


Figure A-5b G07.50 Velocity Contour Map (Large Vector Scale)

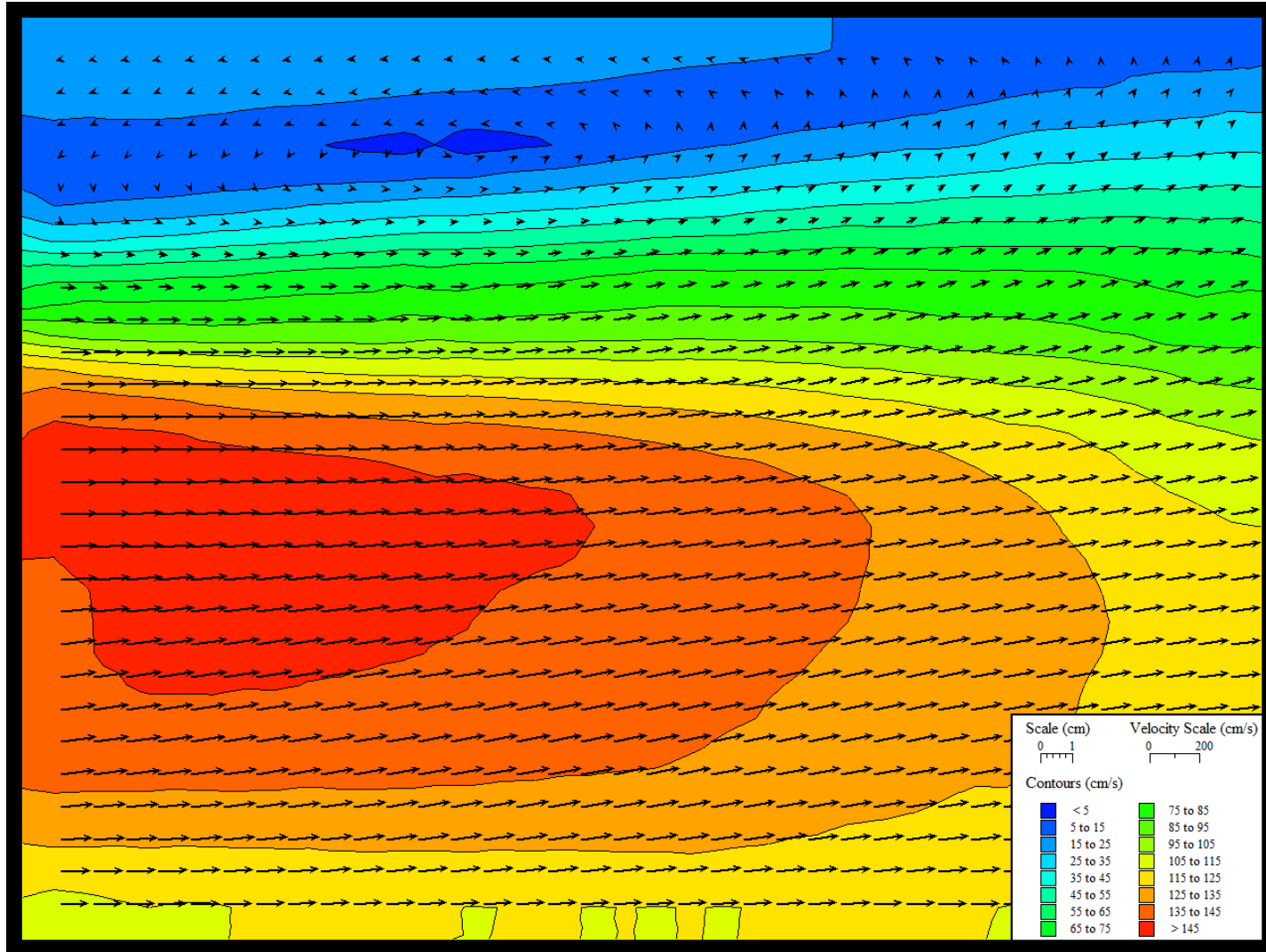


Figure A-6a G09.00 Velocity Contour Map (Small Vector Scale)



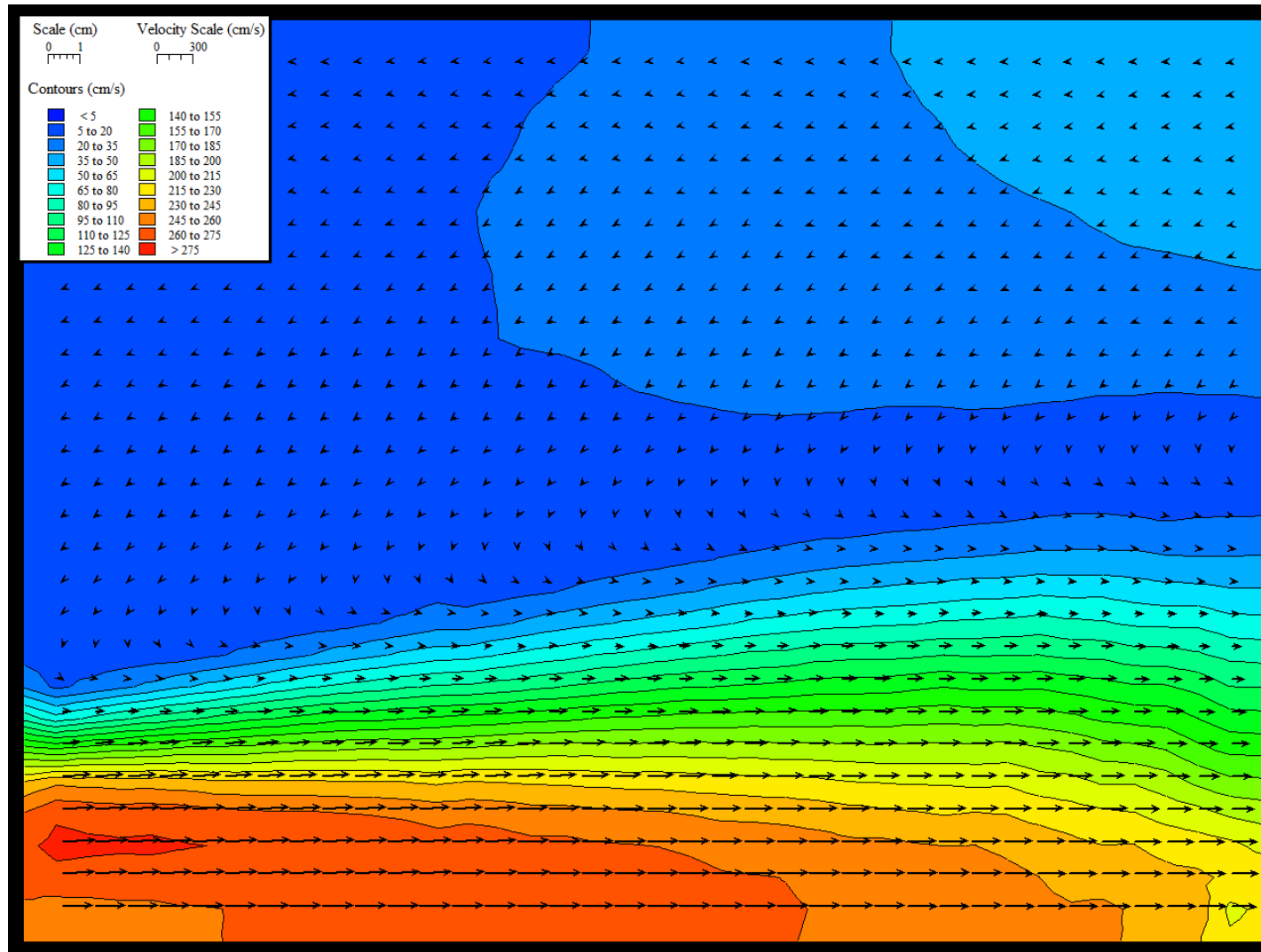


Figure A-6b G09.00 Velocity Contour Map (Large Vector Scale)

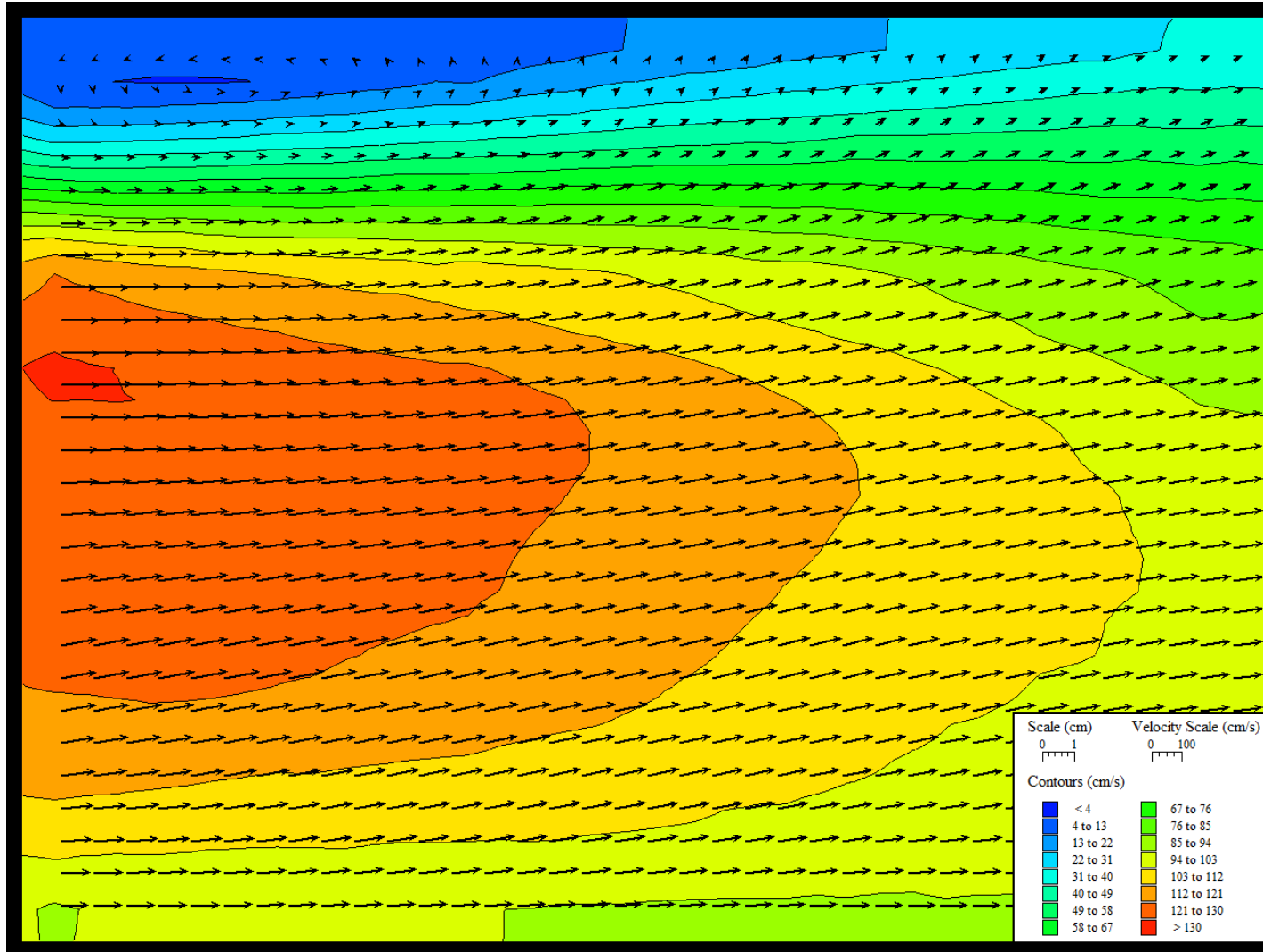


Figure A-7a G10.50 Velocity Contour Map (Small Vector Scale)

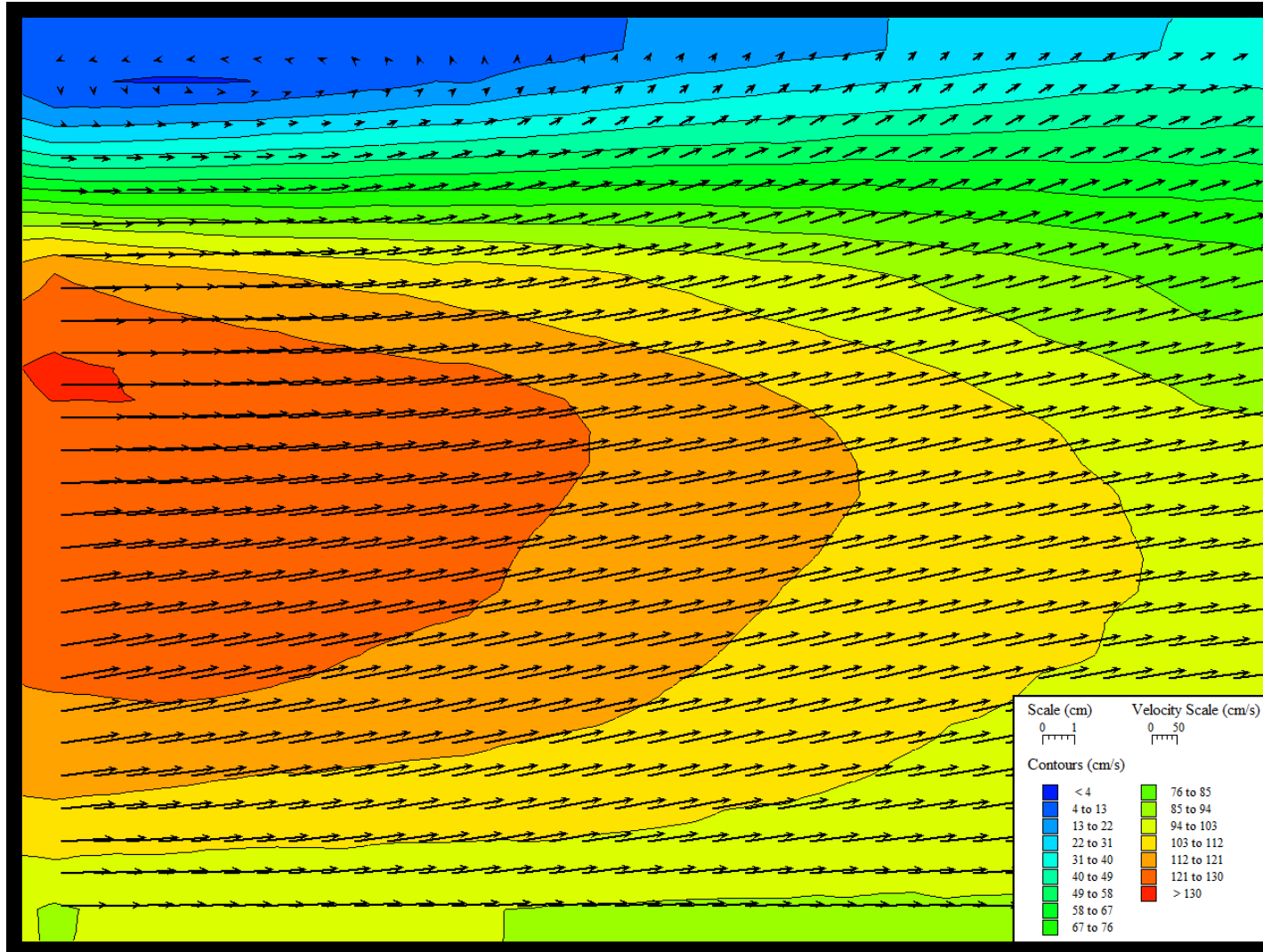


Figure A-7b G10.50 Velocity Contour Map (Large Vector Scale)

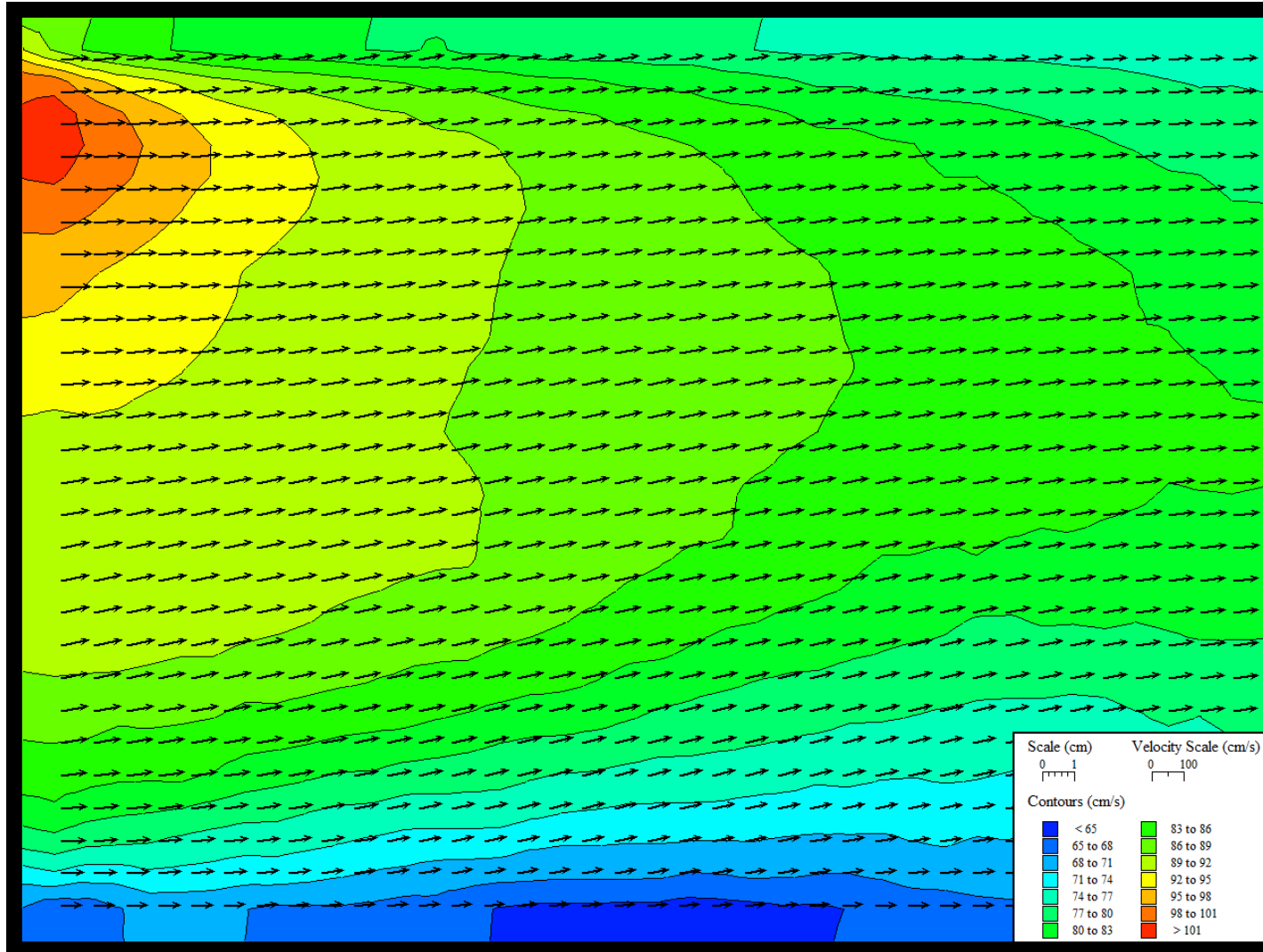


Figure A-8 G12.00 Velocity Contour Map

## Appendix B Measurement, Data Acquisition, and Other System Appurtenances

B-1: Pressure Transducers.....	
B-2: USB Voltage Measurement Device.....	
B-3: Nd:YAG Laser for PIV Measurements.....	
B-4: Prosilica GT1290 Camera.....	
B-5: Delay Generator.....	
B-6: Sperian LOTG-YAG/KTP Safety Goggles.....	
B-7: Pump Information.....	

## B-1: Pressure Transducers

# ALL STAINLESS STEEL TRANSDUCER MULTIMEDIA COMPATIBILITY HIGH-PERFORMANCE SILICON TECHNOLOGY

Engineered from  
1 to 10,000 psi.

**PX309 Series**  
Gage/Absolute Pressure  
0 to 5 Vdc Output  
0-1 to 0-10,000 psi  
0-70 mbar to 0-690 bar

Starts at  
**\$225**



- ✓ 1, 2, and 5 psi Low Pressure Ranges
- ✓ Rugged, Solid State Design
- ✓ All Stainless Steel
- ✓ High Stability, Low Drift
- ✓ 0.25% Accuracy
- ✓ RoHS Compliant
- ✓ IP65 Protection Class

### SPECIFICATIONS

**Excitation:** 9 to 30 Vdc (<10 mA)  
(reverse polarity and overvoltage protected)

**Output:** 0 to 5 Vdc

**Accuracy:**  $\pm 0.25\%$  FS BSL at 25°C;  
includes linearity, hysteresis and repeatability

**Zero Offset:**  $\pm 2\%$  FSO;  
 $\pm 4\%$  for 1 and 2 psi ranges

**Span Setting:**  $\pm 2\%$  FSO;  
 $\pm 4\%$  for 1 and 2 psi ranges

**Total Error Band:**  $\pm 2\%$  FSO, includes linearity, hysteresis, repeatability, thermal hysteresis and thermal errors (except 1 psi =  $\pm 4.5\%$  and 2 psi =  $\pm 3\%$ )

**Long-Term Stability (1 Year):**  
 $\pm 0.25\%$  typical

**Typical Life:** 10 million cycles

**Operating Temperature:** -40 to 85°C  
(-40 to 185°F)

**Compensated Temperature:**

>5 psi Range: -20 to 85°C (-4 to 185°F)

≤5 psi Range: 0 to 50°C (32 to 122°F)

**Proof Pressure:**  
psia and ≤50 psig: 3x capacity  
or 20 psi, whichever is greater  
≥100 psi: 2x capacity



**Burst Pressure:** 5x capacity or 25 psi, whichever is greater

**Response Time:** <1 ms

**Shock:** 50 g, 11 ms half-sine shock

**Vibration:**  $\pm 20$  g

**Wetted Parts:** 316 SS for all psia ranges and 1 to 50 psig; 17-4 PH SS for ranges 100 to 10,000 psig

**Pressure Port:** 1/8-18 MNPT

**Electrical Connections:**

PX309: 1.5 m (5') 3-conductor cable

PX319: mini DIN connector with mating connector included

PX329: Twist-lock connector, mating connector sold separately (PT06V-10-6S)

**Weight:** 155 g (5.4 oz) max

**Note:** Units 100 psig and above may be subjected to vacuum on the pressure port without damage

For alternative performance specifications contact Engineering.

Order a snubber to protect your pressure transducer!



PS-4G, \$12.75, shown actual size.

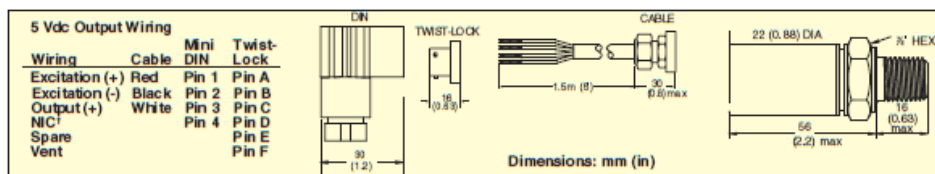
Snubbers protect sensors from fluid hammers/spikes.

VOLTAGE OUTPUT  
PRESSURE TRANSDUCERS  
**B**

B-96



## RUGGED, GENERAL PURPOSE TRANSDUCER

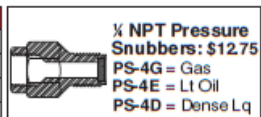


     LOW-PRESSURE RANGES HIGHLIGHTED

To Order (Specify Model Number)							
RANGE		1.5 m CABLE CONNECTION	PRICE	MINI DIN CONNECTION	PRICE	TWIST-LOCK CONNECTION	PRICE
bar	psi						
<b>ABSOLUTE PRESSURE</b>							
0 to 0.34	0 to 5	PX309-005A5V	\$325	PX319-005A5V	\$325	PX329-005A5V	\$350
0 to 1	0 to 15	PX309-015A5V	245	PX319-015A5V	245	PX329-015A5V	295
0 to 2.1	0 to 30	PX309-030A5V	245	PX319-030A5V	245	PX329-030A5V	295
0 to 3.4	0 to 50	PX309-050A5V	245	PX319-050A5V	245	PX329-050A5V	295
0 to 6.9	0 to 100	PX309-100A5V	245	PX319-100A5V	245	PX329-100A5V	295
0 to 14	0 to 200	PX309-200A5V	245	PX319-200A5V	245	PX329-200A5V	295
0 to 21	0 to 300	PX309-300A5V	245	PX319-300A5V	245	PX329-300A5V	295
<b>GAGE PRESSURE</b>							
0 to 0.07	0 to 1	PX309-001G5V	\$345	PX319-001G5V	\$345	PX329-001G5V	\$370
0 to 0.14	0 to 2	PX309-002G5V	325	PX319-002G5V	325	PX329-002G5V	350
0 to 0.34	0 to 5	PX309-005G5V	300	PX319-005G5V	300	PX329-005G5V	325
0 to 1	0 to 15	PX309-015G5V	225	PX319-015G5V	225	PX329-015G5V	275
0 to 2.1	0 to 30	PX309-030G5V	225	PX319-030G5V	225	PX329-030G5V	275
0 to 3.4	0 to 50	PX309-050G5V	225	PX319-050G5V	225	PX329-050G5V	275
0 to 6.9	0 to 100	PX309-100G5V	225	PX319-100G5V	225	PX329-100G5V	275
0 to 10	0 to 150	PX309-150G5V	225	PX319-150G5V	225	PX329-150G5V	275
0 to 14	0 to 200	PX309-200G5V	225	PX319-200G5V	225	PX329-200G5V	275
0 to 21	0 to 300	PX309-300G5V	225	PX319-300G5V	225	PX329-300G5V	275
0 to 34	0 to 500	PX309-500G5V	225	PX319-500G5V	225	PX329-500G5V	275
0 to 69	0 to 1000	PX309-1KG5V	225	PX319-1KG5V	225	PX329-1KG5V	275
0 to 138	0 to 2000	PX309-2KG5V	225	PX319-2KG5V	225	PX329-2KG5V	275
0 to 207	0 to 3000	PX309-3KG5V	225	PX319-3KG5V	225	PX329-3KG5V	275
0 to 345	0 to 5000	PX309-5KG5V	225	PX319-5KG5T	225	PX329-5KG5V	275
0 to 517	0 to 7500	PX309-7.5KG5V	225	PX319-7.5KG5V	225	PX329-7.5KG5V	275
0 to 690	0 to 10,000	PX309-10KG5V	225	PX319-10KG5V	225	PX329-10KG5V	275

### ACCESSORIES

MODEL NO.	PRICE	DESCRIPTION
CAL-3	150.00	Recalibration: 5-point NIST traceable
PT06V-10-6S	26.50	Mating twist-lock connector for PX329
CA-39-4PC22-5	90.00	Mating twist-lock connector with 1.5 m (5') cable for PX329
CX5302	15.00	Extra mating mini DIN connector for PX319



Comes complete with 5-point NIST-traceable calibration.

Ordering Examples: PX309-100G5V, 100 psi gage pressure transducer with 0 to 5 Vdc output and 1 m cable termination, \$225.

PX319-015A5V, 15 psi absolute pressure transducer with 0 to 5 Vdc output and mini DIN termination, \$300. PX329-3KG5V, 3000 psi gage pressure transducer with 0 to 5 Vdc output and twist-lock termination, \$275. Mating connector sold separately; order P T06V-10-6S, \$26.50.

## **B-2: USB Voltage Measurement Device**

### **NI USB-6210**

#### **16-Bit, 250 kS/s M Series Multifunction DAQ, Bus-Powered**

- 16 analog inputs (16-bit, 250 kS/s)
- 4 digital inputs; 4 digital outputs; two 32-bit counters
- Bus-powered USB for high mobility; built-in signal connectivity
- NI signal streaming for sustained high-speed data streams over USB
- Compatibility with LabVIEW, LabWindows™/CVI, and Measurement Studio for Visual Studio .NET
- NI-DAQmx driver software and LabVIEW SignalExpress LE interactive data-logging software



### **Overview**

The NI USB-6210 is a bus-powered M Series multifunction data acquisition (DAQ) module for USB that is optimized for superior accuracy at fast sampling rates. It offers 16 analog inputs; a 250 kS/s single-channel sampling rate; four digital input lines; four digital output lines; four programmable input ranges ( $\pm 0.2$  to  $\pm 10$  V) per channel; digital triggering; and two counter/timers.

The USB-6210 is designed specifically for mobile or space-constrained applications. Plug-and-play installation minimizes configuration and setup time, while direct screw-terminal connectivity keeps costs down and simplifies signal connections. This product does not require external power.

This module also features the new NI signal streaming technology, which gives you DMA-like bidirectional high-speed streaming of data across USB. For more information about NI signal streaming, view the Resources tab.

Bus-powered M Series devices for USB are available in OEM versions. Check the Resources tab or use the left navigation to get pricing and technical information.

#### **Driver Software**

NI-DAQmx driver and measurement services software provides easy-to-use configuration and programming interfaces with features such as the DAQ Assistant to help reduce development time. Browse the information in the Resources tab to learn more about driver software or download a driver. M Series devices are not compatible with the Traditional NI-DAQ (Legacy) driver.

#### **Application Software**

Every M Series DAQ device includes a copy of NI LabVIEW SignalExpress LE data-logging software, so you can quickly acquire, analyze, and present data without programming. In addition to LabVIEW SignalExpress, M Series DAQ devices are compatible with the following versions (or later) of NI application software: LabVIEW 7.1, LabWindows/CVI 7.x, or Measurement Studio 7.x. M Series DAQ devices are also compatible with Visual Studio .NET, C/C++, and Visual Basic 6.0.

The mark LabWindows is used under a license from Microsoft Corporation. Windows is a registered trademark of Microsoft Corporation in the United States and other countries.



## **B-3: Nd:YAG Laser for PIV Measurements**

### **Solo PIV Nd:YAG Laser Systems**



#### **Reliable Operation**

- Thermally compensated resonator assures stable operation.
- Rugged I-Beam resonator design on Solo 120XT and Solo 200XT
- Requires minimal maintenance, increasing system up-time.
- Field-proven reliability permits users to concentrate on their applications, rather than on system upkeep.

#### **Exceptional Performance**

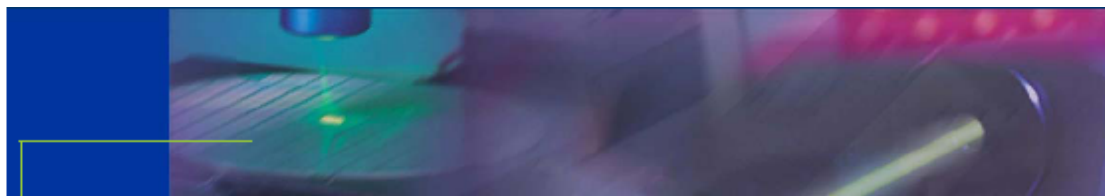
- Superior, proven design provides stable, high-energy output with excellent beam quality and pulse-to-pulse stability.
- Compact resonator design provides excellent beam pointing and energy stability.
- Predictable, high performance ensures that your work gets done faster.

**S**olo PIV is a compact, dual laser-head system designed to provide a highly stable green light source for Particle Image Velocimetry (PIV) applications. It is ideally suited for most liquid and many air-based PIV experiments, and its small size provides excellent flexibility in setting-up such experiments.

#### **Features**

- Small laser head requires minimum space
- Single power supply simplifies setup and enhances mobility
- High output energy
  - 15 - 200 mJ at 532 nm
- Highly flexible design with repetition rates
  - From 1 to 15, or 30 Hz, depending on model selected
- Operating convenience provided through multiple triggering capabilities
  - Continuous internal trigger
  - External TTL trigger
  - Single input pulse activating laser lamp and Q-switch
  - Separate pulses to control lamp & Q-switch independently for precise laser pulse timing control
- Easy set up:
  - Single power supply features internal, closed-loop cooling system
  - Operates on 95-240 VAC single phase source
- Convenient operation made possible with:
  - Remote positioning of a single power supply - saves valuable lab space
  - Local control panel on power supply with all system controls, including optional optical attenuator





### Solo PIV Products

		Solo I-15	Solo II-15	Solo II-30	Solo III-15	Solo 120XT	Solo 200XT
Repetition Rate (Hz)		15	15	30	15	15	15
Energy <sup>1,2</sup> (mJ)	532 nm	15	30	30	50	120	200
	266 nm	NA	NA	NA	NA	20	30
Energy Stability <sup>3</sup> (%)	532 nm	4	4	4	4	4	4
	266 nm	NA	NA	NA	NA	9	9
Beam Diameter (mm)		3	3	3	4	5	6
Pulse Width <sup>3</sup> (ns)		3-5	3-5	3-5	3-5	3-5	3-5
Divergence <sup>4</sup> (mrad)		< 3	< 3	< 3	< 4	< 3	< 4
Beam Pointing (urad)		< 100	< 100	< 100	< 100	< 100	< 100
Jitter (±ns) <sup>5</sup>		1	1	1	1	1	1

- Optical losses due to optional attenuator will reduce maximum energy by 10%.
- Energy and pulse-to-pulse stability for 98% of shots after 30 minute warm up.
- Full width half maximum.
- Full angle for 86% of the energy, at 1/e<sup>2</sup> point.
- From Q-switch synch out to light pulse, 98% of 1000 shots.

### Physical Characteristics

	Laser Head*			Power Supply		
	Solo I, II, III	Solo 120XT	Solo 200XT	Solo I, II, III	Solo 120XT	Solo 200XT
Length	13.775"/350 mm	22.4"/569mm	24.4"/620 mm	18.15" / 461 mm	19.0"/483 mm	21.2" / 538 mm
Width	7.0"/178 mm	9.24"/235 mm	9.24"/235 mm	7.77" / 194 mm	8.6"/218 mm	10.6" / 269 mm
Height	3.167"/81 mm	4.86"/123 mm	4.86"/123 mm	14.32" / 363 mm	15.0"/381 mm	15.16" / 385 mm
Weight	10 lbs./4.5 kg	34 lbs./15.5 kg	40 lbs./18.2 kg	48 lbs. / 22 kg	53 lbs/24 kg	53 lbs. / 24 kg
Length Umbilical	8 ft / 2.4 m	10 ft / 3 m	10 ft / 3 m			

\* Width and height include mounting plate

### Operating Requirements

Temperature	50° - 86° F (10° - 30° C)	
Relative Humidity	20—80% non-condensing	
Voltage	95—240 V, 50/60 Hz	
Power	Solo I, II, III	15 Hz-800 watts; 30 Hz-900 watts
	Solo 120XT	1000 watts
	Solo 200XT	1500 watts

Specifications and product offering subject to change without notice.



**USA**  
New Wave™ Research, Inc.  
4850 Kato Road  
Fremont CA, 94538-7339  
Tel: 510-249-1550  
Tel: 800-596-1743  
Fax: 510-249-1551  
Email: [Sales@new-wave.com](mailto:Sales@new-wave.com)

**Japan**  
New Wave™ Research, KK  
SF Chojiya Building, 1-35-4,  
Shinjuku-ku, Shinjuku  
Tokyo, 165-0022 Japan  
Tel: +81-3-3351-0131  
Fax: +81-3-3351-0121  
Email: [NewWaveKJ@new-wave.com](mailto:NewWaveKJ@new-wave.com)

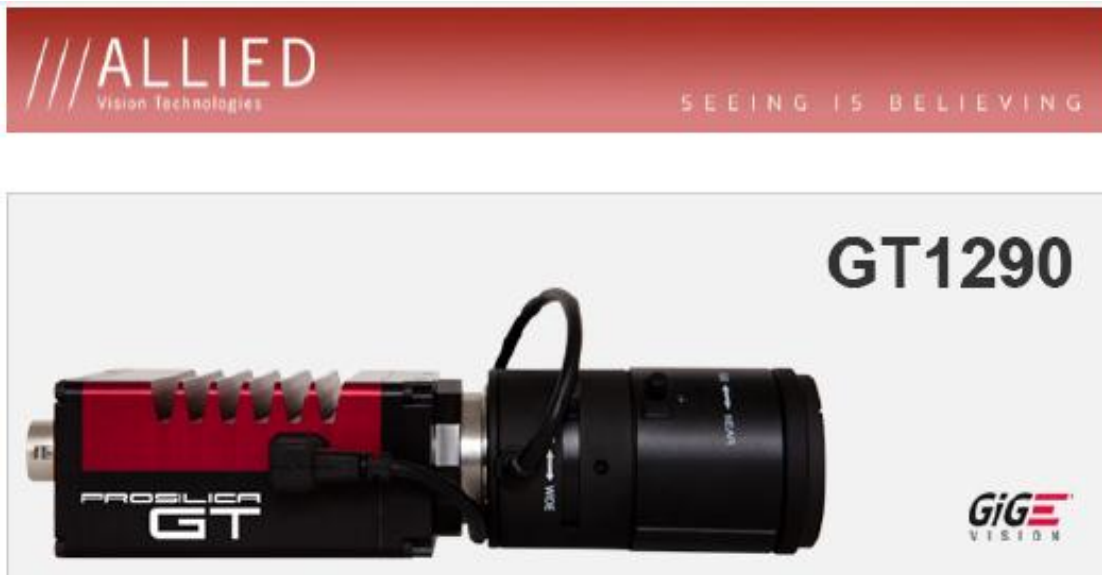
**Taiwan**  
New Wave™ Research G. C. Co., Ltd.  
2F, No. 58-3, XingShan Rd.,  
Neihu Dist.,  
Taipei, Taiwan 114, R.O.C.  
Tel: 886-2-8792-7585  
Fax: 886-2-8792-7584  
Email: [NewWaveSQ@new-wave.com](mailto:NewWaveSQ@new-wave.com)

**Europe**  
New Wave™ Research Co., Ltd.  
8 Auro Court, Emire Business Park  
Huntington, Cambs  
England PE29 6XS, UK  
Tel: 44-(0)1480 456 566  
Fax: 44-(0)1480 456 545  
Email: [NewWaveEU@new-wave.com](mailto:NewWaveEU@new-wave.com)

**China**  
New Wave Research (China) Co., Ltd.  
Rm. 1102, 11/F, Jiesing Mansion,  
No. 877, Dongfeng Rd.  
Shanghai, 200122, China  
Tel: 86-21-5058-7785  
Fax: 86-21-5058-7785  
Email: [NewWaveCN@new-wave.com](mailto:NewWaveCN@new-wave.com)

©2004, 2005, 2006 New Wave Research Doc. No. PN-SOL-DS-061023

## B-4: Prosilica GT1290 Camera



### Description

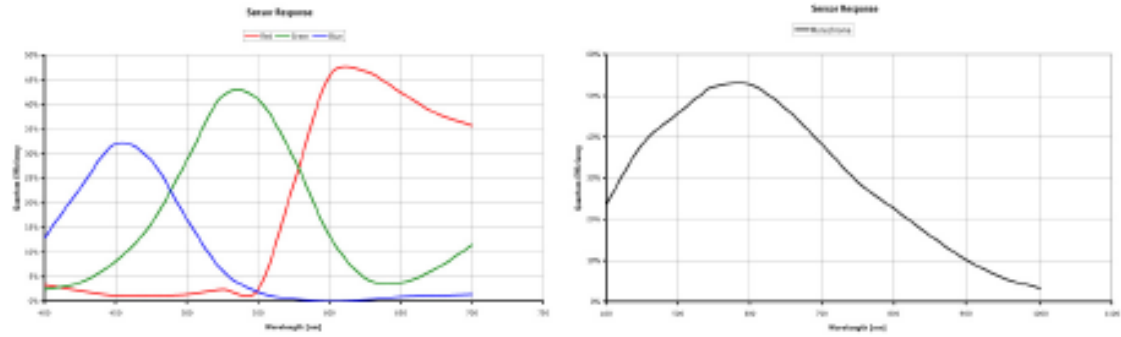
#### **NEW: 1.2 Megapixel camera for extreme environments**

The Prosilica GT1290 is a 1.2 Megapixel camera with a Gigabit Ethernet interface (GigE Vision®). The GT1290 is a rugged camera designed to operate in extreme environments and fluctuating lighting conditions. The GT1290 offers Precise iris lens control allowing users to fix the aperture size to optimize depth of field, exposure and gain without the need for additional control elements. The GT1290 incorporates a high-quality Sony ICX445 Exview HAD CCD sensor providing excellent monochrome and color image quality.

- Sony ICX445 EXview HAD CCD sensor
- Auto Iris (P-Iris and DC)
- Power over Ethernet (PoE)
- Ethernet surge suppression
- Gamma, multiple LUT, color correction
- Metadata (Chunk data), clock synchronization (IEEE1588)
- Wide operating temperature range
- Global shutter (digital shutter)
- **Models:**
  - GT1290, 1280x960, 33 fps, CCD mono
  - GT1290C, 1280x960, 33 fps, CCD color

## Specifications

Prosilica GT	1290
Interface	IEEE 802.3 1000baseT
Resolution	1280 x 960
Sensor	Sony ICX445
Sensor type	CCD Progressive
Sensor size	Type 1/3
Cell size	3.75 $\mu$ m
Lens mount	C-Mount
Max frame rate at full resolution	33 fps
On-board FIFO	128 MB
<b>Output</b>	
Bit depth	8/14 bit
Mono modes	Mono8, Mono12Packed, Mono16
Color modes YUV	YUV411, YUV422, YUV444
Color modes RGB	RGB24, BGR24, RGBA24, BGRA24
Raw modes	Bayer8, Bayer12Packed, Bayer16
<b>General purpose inputs/outputs (GPIOs)</b>	
TTL I/Os	1 input, 2 outputs
Opto-coupled I/Os	1 input, 2 outputs
RS-232	1
<b>Operating conditions/Dimensions</b>	
Operating temperature	-20°C ... +60°C
Power requirements (DC)	8-26 V DC
Power consumption (12 V)	tba
Mass	211 g
Body Dimensions (L x W x H in mm)	83.2 x 53.3 x 33 (including connectors, w/o tripod and lens)
Regulations	CE, FCC Class A, RoHS



## Smart features

The Prosilica GT1290 features include:

- Auto Exposure
- Auto Gain
- Auto White balance
- Flexible Binning
- Region of Interest readout (AOI partial scan)
- StreamBytesPerSecond (easy bandwidth control)
- Stream hold
- Asynchronous external trigger and sync I/O
- Auto Iris (P-Iris and DC)
- Power over Ethernet (PoE)
- Ethernet surge suppression
- Gamma
- Multiple LUT
- Color correction
- Metadata (Chunk data)
- Clock synchronization (IEEE1588)
- Recorder and Multiframe Acquisition Modes

### White Paper

[Remote lens control with Prosilica GT cameras](#)

## **B-5: Delay Generator**

### **Model 9650A Digital Delay Generator**

*Instruction Manual*  
190168-A-MNL-C

Copyright © 2002 AMETEK ADVANCED MEASUREMENT TECHNOLOGY, INC





## Output Pulse Widths

T <sub>0</sub> , A, B, C and D	30 ns to 1 ms (screwdriver adjustable)
A,B and C,D Minimum settable width for valid output:	5 ns. Pulse starts on rising edge of A (or C) and stops on rising edge of B (or D), with edges typically 1 ns later than A (C) and B (D) leading edges when the latter are set to 5 V output levels.

## Output Levels

T <sub>0</sub> , A, B, C and D	Low impedance outputs which generate +5 V, +10 V or -0.8 V into 50 Ω loads, with higher levels when terminated in higher impedances.
Typical pulse transition times when driving a 50 Ω load:	
+5 V and +10 V	1 ns/V risetime, 2.5 ns/V falltime, < 5 % under/overshoot;
-0.8 V	+300 mV undershoot, 200 mV overshoot

A,B and C,D  
Low impedance outputs which generate TTL levels into low or high impedance loads. Typical pulse transition times for a 0.7 V to 2.7 V swing: 5 ns risetime, 5 ns falltime for a 50 Ω load; 3 ns risetime, 4 ns falltime for a 100 Ω load.

## Output Protection

Outputs are short circuit and overload protected and limit if the maximum aggregate current of all outputs averaged over 5 ms exceeds 0.7 A

## Scan Mode

Channel A delay scans with the delay controlled by the following parameters:-	
Initial Delay	0 to 80 μs in 1 ns steps
Triggers/ Step	1 to 49,999
Delay Step Size	0 to 80 μs in 1 ns steps
Delay Steps/Scan	1 to 899 subject to the overall restriction that the max delay in scan mode is 80 μs
Max trigger rate	20 kHz. (external or internal)

Scan Inhibit  
Rear panel active low TTL input inhibits outputs on completion of current scan.

Burst Mode  
Special case of scan mode where Delay Step Size = 0. Allows the generation of 1 to 49,999 pulses using external or internal triggers at up to 20 kHz. Use of scan inhibit input and internal triggers allows the unit to generate "n" pulses on receipt of a single trigger pulse.



**Display**

5 × 7 dot-matrix alphanumeric vacuum fluorescent.

**Setup Storage**

The model 9650A automatically stores the current setup when power is removed and restores it when power is reapplied. Up to 30 additional setups may be saved for future use.

**Computer Interface**

The optional RS232 (-/96) or GPIB (IEEE-488) (-/97) interfaces allow remote setting of the A, B, C and D channel delays, the internal rate generator and the scan settings.

**Options**

9650A/93	Rack Mounting Shelf (for one or two units)
9650A/94	5 MHz External Trigger Option
9650A/96	RS232 Serial Interface (cannot be installed with 9650A/97)
9650A/97	GPIB (IEEE-488) Interface (cannot be installed with 9650A/96)
9650A/98	+15 V Outputs (Increases +10 V output pulse amplitude setting to +15 V)


**Software Support**

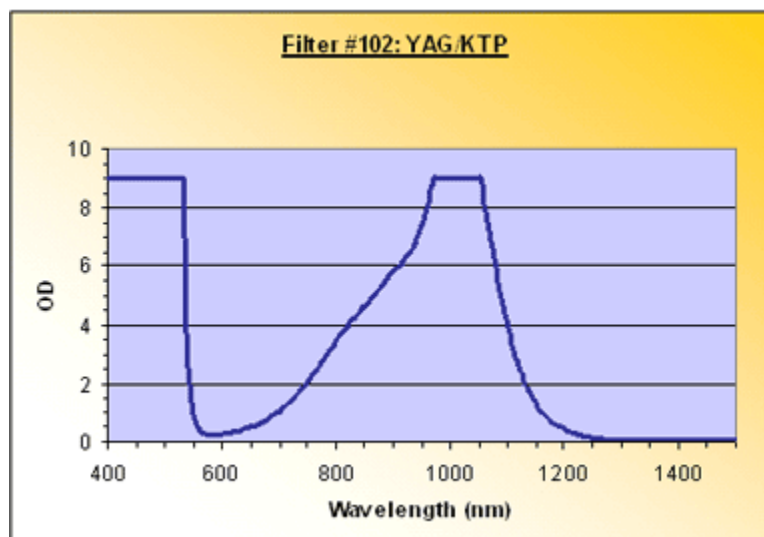
A LabVIEW driver software suitable for version 4.01 and later of LabVIEW is available by download from our website at [www.signalrecovery.com](http://www.signalrecovery.com)

**General**

Power Requirements	
Voltage	110/120/220/240 VAC
Frequency	50/60 Hz
Power	105 VA max
Dimensions	
Width	8¼" (210 mm)
Depth	13¼" (350 mm)
Height	5¼" (135 mm)
Weight	10lb (4.5 kg)

## **B-6: Sperian LOTG-YAG/KTP Safety Goggles**

 <p>LOTG</p>	<ul style="list-style-type: none"> <li>• Fits comfortably over prescription eyewear or can be worn as a stand-alone spectacle</li> <li>• Inclination adjustment</li> <li>• Earpiece length adjustment</li> <li>• Meets ANSI Z87 impact requirements</li> </ul>
---	--



### **WARNING:**

Always ensure that the wavelength(s) listed on your eyewear correspond to the wavelength(s) of the laser being used. Use of this product for protection against wavelength(s) not listed on the eyewear may result in serious personal injury, including blindness.

## B-7: Pump Information

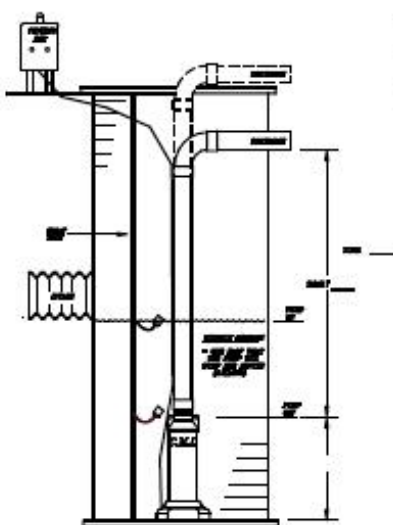
# STAINLESS STEEL AXIAL FLOW SUBMERSIBLE PUMPS



Carry Pumps are an economical solution to all your water management needs. These pumps are well suited for high volume, low head applications like aquaculture fish farming, agricultural field drainage, golf course watering systems, landscaping waterfalls, artesian wells, and fountains, municipal storm water systems, subdivisions, manufactured home communities, parking lots, water transfer and sub-irrigation.

- Corrosion Resistant Stainless Steel Construction
- High Volume: 500 to 1,300 Gallons Per Minute
- Low Head: 2' to 25' of Total Dynamic Head
- Available in Single or Three Phase  
200, 230, 460 or 575 Volts
- Axial-Flow lift for smooth, low vibration, low pressure operation
- Rated for up to 4 cycles per hour or continuous duty
- Economical and efficient to operate
- Water lubricated motor - environmentally safe

All Carry Pumps are built to last. With Stainless Steel Construction and durable Franklin Electric motors and controls, your pump should give you many years of trouble free operation. All products come with a one year limited warranty against manufacturer's defects and workmanship.



Typical Drainage Installation

Pumps are available in vertical or horizontal styles with or without strainer screens.

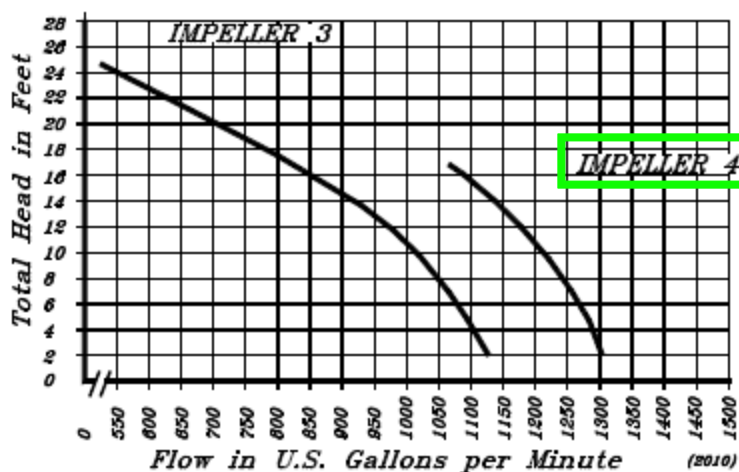


**For more information or a free estimate,  
call Carry Manufacturing today!**



Carry Manufacturing, Inc.  
1514 S. Knight Road, Munger, MI 48747-9703  
(989) 659-3500 or 1-800-492-2779  
Fax: (989) 659-3506 [www.carrymfg.com](http://www.carrymfg.com)

## STAINLESS STEEL AXIAL FLOW SUBMERSIBLE PUMPS



10 HP pumps are available in either vertical or horizontal styles. These pumps can be single phase, 230 volts and three phase in 200, 230, 460 or 575 volts.

Single phase, 3-wire and three phase pumps require a control panel.

10 HP PERFORMANCE CURVE

**MADE IN AMERICA**